



**SEARCH FOR NEW PARTICLES DECAYING TO DIJET WITH
QUARK/GLUON JET TAGGING IN 13 TeV PROTON-PROTON COLLISIONS
AT CMS**

**Ayşe BAT
Ph.D. THESIS**

**DEPARTMENT OF PHYSICS
Assoc. Prof. Dr. Sertaç ÖZTÜRK
April- 2018
All right reserved**

**T.C
GAZIOSMANPAŞA UNIVERSITY
GRADUATE SCHOOL OF NATURE AND APPLIED SCIENCES
DEPARTMENT OF PHYSICS**

Ph.D. THESIS

**SEARCH FOR NEW PARTICLES DECAYING TO DIJET WITH
QUARK/GLUON JET TAGGING IN 13 TeV PROTON-PROTON
COLLISIONS AT CMS**

Ayşe BAT

TOKAT
April- 2018

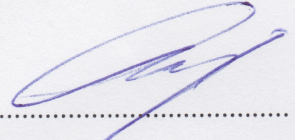
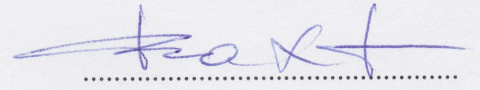
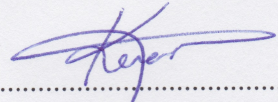
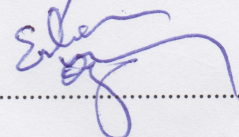
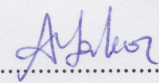
All right reserved

The defense examination of the thesis titled "Search for New Particles Decaying to Dijet with Quark/Gluon Jet Tagging in 13 TeV Proton-Proton Collisions at CMS" was defended by **Ayşe Bat** on April 2, 2018, and it was accepted with vote union as a Ph.D. thesis at Gaziosmanpaşa University Graduate School of Nature and Applied Sciences Department of Physics.

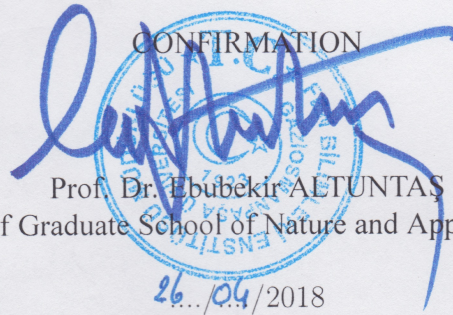
Jury Members

Signature

Supervisor
Assoc. Prof. Dr. Sertaç ÖZTÜRK
GAZİOSMANPAŞA UNIVERSITY
Member
Prof. Dr. Bahtiyar MEHMETOĞLU
GAZİOSMANPAŞA UNIVERSITY
Member
Prof. Dr. Kenan SÖĞÜT
MERSİN UNIVERSITY
Member
Prof. Dr. Veysi Erkean ÖZCAN
BOĞAZİÇİ UNIVERSITY
Member
Assoc. Prof. Dr. Ali YAKAR
GAZİOSMANPAŞA UNIVERSITY


.....

.....

.....

.....

.....

CONFIRMATION


Prof. Dr. Ebubekir ALTUNTAS
Director of Graduate School of Nature and Applied Sciences

26...04/2018

THESIS DECLARATION

I declare that this thesis is written in accordance with the rules of thesis writing is complied with scientific rules of ethics, in the case of using the works of others, it is cited in accordance with scientific norms, the novelty and results contained in the thesis are not taken from another place, no falsification is made in the used data, is not offered as another thesis work at this university or any other university.



Ayşe BAT

02/04/2018



To my family, my adorable niece Zeynep Rmeysa, and nephew mer Asaf.

ABSTRACT

Ph.D. THESIS

SEARCH FOR NEW PARTICLES DECAYING TO DIJET WITH QUARK/GLUON JET TAGGING IN 13 TeV PROTON-PROTON COLLISIONS AT CMS

Ayşe BAT

GAZIOSMANPAŞA UNIVERSITY GRADUATE SCHOOL OF NATURE AND
APPLIED SCIENCES

DEPARTMENT OF PHYSICS

(SUPERVISOR: Assoc. Prof. Dr. Sertaç ÖZTÜRK)

A search for narrow resonances decaying to dijet final states in proton-proton collision data collected by the CMS experiment at the center-of-mass energy of $\sqrt{s} = 13$ TeV is presented in this thesis. The data used corresponding to an integrated luminosity of 35.9 fb^{-1} , and the results are presented for two analyses: A standard dijet narrow resonance search and another one utilizing quark/gluon jet tagging. Both searches use the same analysis techniques looking for resonances with mass above 1.2 TeV using PF jets reconstructed with anti- k_T clustering algorithm. The leading jets are required to be separated from each other in pseudorapidity, $\Delta\eta < 1.3$, and both are needed to be in the central part of the detector, $\eta < 2.5$. A smooth parameterization is used to fit the dijet mass spectrum, and no significant evidence for the presence of a new particle is observed. Upper limits at 95% confidence level are set on the production cross section times branching ratio times to dijet acceptance ($\sigma \times BR \times A$) of the $\Delta\eta$ and η cuts for narrow resonances from gluon-gluon, quark-gluon, and quark-quark final states. These upper limits are interpreted as excluding a mass for specific models: RS gravitons below 1.7 TeV, Z' bosons below 2.7 TeV, W' bosons below 3.3 TeV, color octet scalar ($k_s^2 = 1/2$) below 3.4 TeV, excited quarks below 6.0 TeV, axigluons and colorons below 6.1 TeV, scalar diquarks below 7.2 TeV, and string resonances below 7.4 TeV are excluded. Quark/gluon tagging is shown to improve the exclusion to 3.7 TeV for color octet scalar ($k_s^2 = 1/2$), the only model for which tagging results in better results.

2018, - - - 118

KEYWORDS: CMS, LHC, Jets, Dijet, quark/gluon tagging

ÖZET

DOKTORA TEZİ

13 TEV PROTON PROTON ÇARPIŞMALARINDA CMS'TE İKİ JETE BOZUNAN YENİ PARÇACIKLARIN KUARK/GLUON JET ETİKETLEMESİ İLE ARAŞTIRILMASI

Ayşe BAT

GAZİOSMANPAŞA ÜNİVERSİTESİ FEN BİLİMLERİ ENSTİTÜSÜ

FİZİK ANA BİLİM DALI

(TEZ DANIŞMANI: Doç. Dr. Sertaç ÖZTÜRK)

Bu tezde, 13 TeV kütle merkezi enerjisinde CMS deneyinde toplanan veriler ile son durumda iki jete bozunan dar rezonanslar için yapılan araştırma sonuçları sunuldu. 35.9 fb^{-1} lık entegre ışınım değerine karşılık gelen data kullanıldı ve sonuçlar iki ayrı analiz çalışması olarak sunuldu: biri standart iki-jet dar rezonans araştırması ve diğeri quark/gluon jet etiketleme. İki çalışmada da aynı analiz tekniği kullanıldı, bunun için iki-jet kütlesi 1.2 TeV' den büyük PF jetleri anti- k_T kümeleme algoritması ile yapılandırıldı. Önde gelen iki jetin pseudorapiditilerinin birbirinden $\Delta\eta < 1.3$ kadar ayrılması, ve bu iki jetin dedektörün merkez bölgesinden gelmesi gerekmektedir. İki-jet kütle dağılımı düz bir fonksiyon ile fit edildi, ve yeni parçacık kanıtı olabilecek önemli bir gelişme gözlenmedi. %95 güvenilirlik seviyesinde üst limitler tesir kesiti kere dallanma oranı kere iki-jet olayları kabulü ile dar rezonanslar için $\Delta\eta$ ve η kesimleriyle gluon-gluon, quark-gluon ve quark-quark son durumları için elde edildi. Bu üst sınırlar, belirli modeller için bir kütleyi dışarıladığı şeklinde yorumlanır: 1.7 TeV'in altındaki RS Gravitonları, 2.7 TeV'in altındaki Z' bozonları, 3.3 TeV'in altındaki W' bozonları, 3.4 TeV'in altındaki color octet scalar ($k_s^2 = 1/2$), 6.0 TeV'in altındaki uyarılmış kuarklar, 6.1 TeV'in altındaki axigluonlar ve coloronlar, 7.2 TeV'in altındaki scalar diquarklar ve 7.6 TeV'in altındaki string rezonanslar dışarılanmıştır. Quark/gluon etiketlemenin daha iyi sonuçlara yol açtığı tek model olan color octet scalar için 3.7 TeV'lik gelişme gösterilmiştir.

2018, - - - 118

ANAHTAR KELİME: CMS, LHC, Jetler, İki-jet, quark/gluon etiketleme

ACKNOWLEDGEMENT

After 6 years of intense learning for me, not only in the scientific area but also on a personal level, today is the day: I am using this opportunity to point out my gratitude to everyone who supported and helped me throughout this period.

Firstly, I would like to express my sincere gratitude to my advisor Sertac Öztürk for his continuous support, patience, and motivation. He has given a new world with a lot of opportunities and his endless support. I am grateful to you for being my advisor. I am also grateful to Robert M. Harris for his support and guidance through my visit at FERMILAB. I am grateful to all of the members of the LPC at FERMILAB. In addition, my sincere thanks to TUBITAK for the funding me with 2214-A research scholarship program that enabled me to visit FERMILAB for this analysis work.

I wish to thank M. Numan Bakırcı, Pawel de Barbaro, Paolu Rumerio and German Martinez for given me the opportunity to work with the HCAL team at CERN. I would like to thank Richard Kellogg for his inspiring spirit and his awesome coffees. A special thanks to Danny Noonan, Joseph Mariano, Semra türkçapar, Caleb James Smith, Candan Isık, and Joshua M. Kunkle for their support during the upgrade studies and for their friendship. My deepest thanks go to Kelvin Mei and V. Erkcan Özcan for spending the time to read and evaluate my thesis. Thanks to Kenan Söğüt and Bahtiyar Mehmetoğlu for joining to my defence committee. Thanks also to all the members of the CMS experiment.

I want to express my appreciation to my special friends Elif Somuncu and Melek Kara for encouraging me all the time. They always give me positive feelings about what I am doing. I am grateful for their friendship with along Burcu Ucar.

Most importantly, none of this could have happened without my family, I am really grateful to have them as a parent and sibling. I have appreciated their support during this period.

Ayşe BAT
02/04/2018

CONTENTS

	Page
ABSTRACT	i
ÖZET	ii
ACKNOWLEDGEMENT	iii
CONTENTS	iv
SYMBOLS AND ABBREVIATIONS	vii
LIST OF FIGURES	ix
LIST OF TABLES	xiv
1 INTRODUCTION	1
2 THEORY OF PARTICLE PHYSICS	5
2.1 The Standard Model of Particle Physics	5
2.2 Quantum Chromodynamics (QCD)	7
2.2.1 Color factor in QCD	9
2.3 Hadron-Hadron Collision	10
2.3.1 Hadronic cross section	12
2.4 Dijet Resonance Models	15
2.4.1 Excited quark	16
2.4.2 Randall-Sundrum gravitons	17
2.4.3 Axigluon	20
2.4.4 Colorons	21
2.4.5 Color octet scalars	22
2.4.6 Z' and W'	23
2.4.7 E_6 Diquarks	24

3	EXPERIMENTAL APPARATUS	26
3.1	The Large Hadron Collider	26
3.2	CMS Detector	28
3.2.1	Coordinate system	30
3.2.2	Tracker	31
3.2.3	The Electromagnetic Calorimeter (ECAL)	34
3.2.4	The Hadronic Calorimeter (HCAL)	38
3.2.5	The Magnet	42
3.2.6	The Muon system	42
3.2.7	Data Acquisition (DAQ) and trigger	45
3.2.8	CMS computing model	48
4	JET RECONSTRUCTION AND CALIBRATION AT CMS	51
4.1	The Particle Flow Jets	51
4.2	Jet Reconstruction Algorithms at CMS	53
4.2.1	The Anti- k_T Algorithm	55
4.3	Jet Energy Calibration	56
5	MEASUREMENT OF DIJET MASS SPECTRUM	59
5.1	Data Set and Monte Carlo Samples	59
5.2	The Event Selection	60
5.3	Trigger Efficiency	63
5.4	Data Quality Studies	65
5.5	Dijet Mass Spectrum and Fit	71
6	SEARCH FOR DIJET RESONANCES	73
6.1	Signal Modeling	73
6.2	Significance of the Observed Excess	75
6.3	Calculation of Cross section Upper Limits	77
6.4	Systematic Uncertainties	79
6.4.1	Jet energy scale	79
6.4.2	Jet energy resolution	80

6.4.3	Background parametrization	80
6.4.4	Integrated luminosity	80
6.5	Exclusion Limits with Systematic Uncertainties	81
7	DIJET RESONANCE SEARCH WITH QUARK/GLUON JET TAGGING	87
7.1	Motivation	87
7.2	Quark/Gluon Jet Discrimination in CMS	89
7.2.1	A likelihood discriminant	89
7.3	Q/G Jet Tagging Discriminator Optimization	91
7.4	Dijet Mass Measurement with Quark/Gluon Jet Tagging	94
7.4.1	Trigger efficiency	95
7.4.2	Data quality	96
7.4.3	Impact of q/g jet tagging on signal modeling	99
7.4.4	Dijet mass spectrum and fit	100
7.4.5	Setting of cross section upper limits	103
8	CONCLUSION	106
	REFERENCES	108
	APPENDIX A	112
	APPENDIX B	116
	CURRICULUM VITAE	118

SYMBOLS AND ABBREVIATIONS

Symbols	Explanation
q	Quark
\bar{q}	Anti-quark
q^*	Excited quark
e	Electron
g	Gluon
H	Higgs boson
s	Center of mass energy
W	W boson
Z	Z boson
μ	Muon
τ	Tau
ν_e	Electron neutrino
ν_μ	Muon neutrino
ν_τ	Tau neutrino
α_s	Strong coupling
γ	Photon
Γ	Resonance width
η	Pseudorapidity
X_0	Radiation length
σ	Cross Section
P_T	Transverse momentum
A	Acceptance
D	E_6 diquark
S_8	Color octet scalar
C	Coloron

Abbreviations	Explanation
ALICE	A Large Ion Collider Experiment
ATLAS	A Toroidal LHC Apparatus
BSM	Beyond the Standard Model Conceil Europeenne
CERN	pour la Recherche Nucleaire
CEMF	Charged Hadron Electromagnetic Fraction
CHF	Charged Hadron Fraction
CL	Confident Level
CMS	Compact Muon Solenoid
DAQ	Data Acquisition
ECAL	Electromagnetic Calorimeter
EW	Electroweak
FSR	Final State Radiation
HCAL	Hadronic Calorimeter
HF	Hadronic Forward
ISR	Initial State Radiation
JES	Jet Energy Scale
JER	Jet Energy Resolution
QCD	Quantum Chromo Dynamics
QED	Quantum Electro Dynamics
LHC	Large Hadron Collider
MC	Monte Carlo
MUF	Muon Fraction
NEMF	Neutral Hadron Electromagnetic Fraction
NHF	Neutral Hadron Fraction
PDF	Parton Density Function
QGP	Quark-Gluon Plasma
ROC	Receiver Operation Characteristic
SM	Standard Model
TOE	Theory of Everthing

LIST OF FIGURES

<u>Figure</u>	<u>Page</u>
1.1 An illustration of the 'bump hunt' analysis strategy. If an excess is observed in the dijet mass distribution, it can be interpreted as a signal caused by a new massive resonance at that mass value.	3
2.1 The particles of the Standard Model.	6
2.2 Hard scattering event in hadron-hadron collision	10
2.3 The parton distribution functions as a function of the momentum fraction x , at $Q^2 = 10 \text{ GeV}^2$ (on left) and $Q^2 = 10^4 \text{ GeV}^2$ (on right). This plots obtained from Particle Data Group (PDG)	11
2.4 A schematic view of hadron-hadron collision	13
2.5 The cross-section for dijet resonances with $ \eta < 2.5$ & $ \Delta\eta < 1.3$ is shown as a function of resonance mass for the following models: excited quark, axigluon/coloron, scalar diquark, color-octet-scalar ($k_s^2 = 1/2$), String, RS Graviton W' , and Z'	25
3.1 A schematic view of the LHC	26
3.2 The Compact Muon Solenoid (CMS) Detector (Sakuma and McCauley, 2014).	29
3.3 Transverse Slice of the Compact Muon Solenoid (CMS) Detector (David, 2016)	30
3.4 Coordinate system of CMS detector	31
3.5 Pictorial view of the tracker slice in the r - z plane (Viliani, 2016)	32
3.6 Geometrical layout of the pixel detector (Kramäki, 1977).	33
3.7 3D view of the silicon strip tracker with description of the sub-section (Schael, 2003)	33
3.8 Longitudinal view of one quarter of the ECAL with the barrel (EB), the endcaps (EE), and the preshower (ES) (Isildak, 2011)	35
3.9 Approximate positions of the endcap and barrel preshowers in CMS (Hofer, 1997).	37
3.10 The Hadron Calorimeter with Hadron Barrel (HB), Hadron Endcap (HE), and Hadron Outer (HO) in the central part of CMS. The Hadron Forward (HF) is physically separated from the central calorimeter (Green, 1997).	38
3.11 (a) The HO layout (b) HO tiles corresponding to HB towers (Lobanov, 2015)	41

3.12	A quadrant of the R - z cross-section of the CMS detector, The RPC chambers are marked in blue line and they are coupled with DTs (yellow) in the barrel, and CSCs (green) in the endcaps. The steel of the return yoke is shown in gray (Giovanni, 2015).	43
3.13	Layout of the CMS barrel muon DT chambers in one of the 5 wheels(Chatrchyan, 2010)	44
3.14	The Level-1 trigger layout for calorimeter and muon sub-detectors.	47
3.15	The data flow of CMS detector through the tiers.	49
4.1	The Jet evolution at hadron-hadron collision.	52
4.2	Illustration of the infrared sensitivity of a cursory designed jet algorithm: the emission of a soft gluon changes the number of jets (left). Illustration of the product of a collinear unsafe jet algorithm: the collinear splitting changes the direction of the jet (right)	54
4.3	The Scheme of corrections applied to the jets in CMS.	57
4.4	JET energy corrections for 2016 data taking. Simulated jet response from different part of detector (a), Data/MC residual correction for the dependency of the jet response on the jet η obtained on dijet event(b), Data/MC scale factors for the jet response p_T -dependence, evaluated from $\gamma + jet$, $Z(\rightarrow \mu\mu) + jet$ and $Z(\rightarrow ee) + jet$ events, combined in a global fit (c) (Harrel, 2017)	58
5.1	Illustration shows an event with final state radiation, where the use of the wide jet allows to contain the radiated energy that improves the dijet mass resolution.	62
5.2	Trigger efficiency as a function of m_{jj}^{Wide} with the data (black dot) and fit function (continuous red line).	64
5.3	Dijet mass spectrum after full analysis main cut selection. The back markers shows the data the red line shows QCD simulation.	66
5.4	The ratio of the transverse missing energy to the total transverse energy of the event (left) and the angle between beam axis and the dijet system at the center of mass frame ($\cos(\theta^*)$) (right) for data (points) and simulated (continuous histogram) events	68
5.5	The absolute difference in pseudorapidity between two leading wide jets ($\Delta\eta$) (left) and the angle of the two leading jets in the transverse plane ($\Delta\phi$) (right) for data (points) and simulated (continuous histogram) events.	68
5.6	The charged hadron fraction (CHF) (top left), the neutral hadron fraction (NHF) (top right), and the neutral electromagnetic jet energy fraction (NEMF) (Bottom) for data (points) and simulated (continuous histogram) events.	69
5.7	The neutral particle multiplicity (NM) (left) and the photon multiplicity (PM) (right) for data (points) and simulated (continuous histogram) events.	69

5.8	The charged electromagnetic fraction (CEMF) (left) and the muon fraction (MUF) (right) for data (points) and simulated (continuous histogram) events.	70
5.9	η (top left), the transverse momentum (p_T) (top right), and ϕ (bottom) for data (points) and simulated (continuous histogram) events.	70
5.10	The binned fit for PF RECO performed in the range $1246 < m_{jj} < 7866$ GeV. The black point represents the observed data, the continuous red line represents the smooth fit function.	72
6.1	Dijet resonance shapes for all considered parton pairs decay at ten different mass point. $qq \rightarrow G \rightarrow qq$ (top left) , $qg \rightarrow q^* \rightarrow qq$ (top right), and $gg \rightarrow G \rightarrow gg$ (bottom).	74
6.2	Dijet mass spectrum with the data (points) compared to a smooth fit function (solid line) including the narrow resonance signal models (dot-dashed). The signal of three final states is gg , qg , and qq at the resonance mass values 2.0 TeV, 4.0 TeV, and 6.0 TeV corresponding resonance models are color-octet scalar, excited quark, and scalar diquark, respectively	75
6.3	Local significance of a gg resonance (top left), a qg resonance (top right), and a qq resonance (bottom) are calculated with the observed data (points) for every 100 GeV.	76
6.4	%95 CL upper limits on $\sigma \times BR \times A$ for gg resonance (top left), qg resonance (top right), and qq resonance (bottom) with only statistic uncertainties.	78
6.5	%95 CL upper limits on $\sigma \times BR \times A$ for gg resonance (top left), qg resonance (top right), and qq resonance (bottom) with systematic uncertainties. The black points indicates the observed upper limits, the black dashed line represents the expected upper limits, and the green and yellow bands stand for 1σ , and 2σ uncertainty bands, respectively.	83
6.6	The ratio of 95% CL upper limits on $\sigma \times BR \times A$ for a gluon-gluon resonance (top left), a quark-gluon resonance (top right), and a quark-quark resonance (bottom) with and without systematic uncertainties.	84
6.7	The observed upper limits 95% CL on $\sigma \times BR \times A$ for dijet resonance of the gluon-gluon, quark-gluon, and quark-quark compared to the theoretical predictions for color octet scalar , new gauge boson Z' and W' , scalar diquarks, axigluons/colorons, string resonances, and RSGraviton.	85
7.1	Left: ROC curves of each type of parton pairs. The greatest background rejection is achieved for quark-quark parton pair tagging.Right: Improvement of signal significance ratio as a function of resonance mass after applying parton tagging. The tagging discriminator is chosen at 80% signal efficiency	88

7.2	Normalized distributions of the discriminant variables, for quark (red) and gluon (blue) jets at 4 GeV reconstructed jet with $ \eta < 2.5$. Total multiplicity (top left), $P_T D$ (top right), $axis_2$ (bottom).	92
7.3	Normalized distributions of the likelihood quark/gluon discriminant for quark (red) and gluon (blue) at 4 GeV reconstructed jet with $ \eta < 2.5$. . .	93
7.4	Improvement on signal significance for the gluon-gluon parton pair with a 2g-tag method (top left), the quark-quark parton pair with a 0g-tag method (top right), and the quark-gluon parton pair with a 1g-tag method (bottom).	94
7.5	The measurement of trigger efficiency for quark/gluon tagged dijet events versus m_{jj} , 2g-tag (top left), 1g-tag (top right) and 0g-tag (bottom).	95
7.6	The dijet mass distribution with the data (point) and MC simulation (continuous histogram) events for 2g-tag method (left), 1g-tag method (middle), and 0g-tag method (right) along with data/MC ratio on bottom plots.	96
7.7	The η distribution of two leading wide-jets with the data (point) and MC simulation (continuous histogram) events for 2g-tag method (left), 1g-tag method (middle), and 0g-tag method (right) along with data/MC ratio on bottom plots.	97
7.8	The p_T distribution of two leading wide-jets with the data (point) and MC simulation (continuous histogram) events for 2g-tag method (left), 1g-tag method (middle), and 0g-tag method (right) along with data/MC ratio on bottom plots.	97
7.9	The ϕ distribution of two leading wide-jets for 2g-tag (left), 1g-tag (middle), and 0g-tag (right)	98
7.10	The $\Delta\eta$ distribution of two leading wide-jets with the data (point) and MC simulation (continuous histogram) events for 2g-tag method (left), 1g-tag method (middle), and 0g-tag method (right) along with data/MC ratio on bottom plots.	98
7.11	The $\Delta\phi$ distribution of two leading wide-jets with the data (point) and MC simulation (continuous histogram) events for 2g-tag method (left), 1g-tag method (middle), and 0g-tag method (right) along with data/MC ratio on bottom plots.	99
7.12	Resonance shapes with q/g tag on considered parton pair types for resonance mass 1, 3, 5, 7 TeV with different q/g tag operation point, $G \rightarrow gg$ resonance sample with 2g tag(top left), $q^* \rightarrow qg$ resonance sample with 1g tag(top right), and $G \rightarrow qq$ resonance sample with 0g tag,(bottom)	100
7.13	Tagging Rate as a function of resonance mass using 0.5 LD operation point for gluon-gluon resonance sample (top left), quark-gluon resonance sample (top right), and quark-quark resonance sample (bottom).	101

7.14	The binned fit shown for 2g-tag (top left), 1g-tag (top right), and 0g-tag(down). The signal shapes normalized the cross section for each resonance type at that mass and scaled the quark gluon tagging rate for each tagging method.	102
7.15	95% CL upper limits on cross section times ratio times acceptance ($\sigma \times BR \times A$) for gluon-gluon resonance with 2g-tag method (top left), quark-gluon resonance with 1g-tag method (top right), and quark-quark resonance with 0g-tag method (bottom) with systematic uncertainties.	103
7.16	The comparison of standard dijet searches (black point) to the q/g jet tagging (red point) for gluon-gluon resonance using 2g-tag method (top-left), quark-gluon resonance using 1g-tag method (top-right) and, quark-quark resonance using 0g-tag method (bottom).	104
A.1	Two-particle scattering. The kinematical constraints are energy-momentum conservation and the mass shell condition (a). Visualization of Mandelstam variables (b)	112
A.2	Two-particle scattering in center of mass frame. For the constraints on the scattering angle $\cos\theta^*$	113
A.3	Lab frame and center of mass (CM) frame of a two parton system.	114
B.1	Left: The distribution of X variable for qg resonance at various resonance mass points. Right: Comparison of X distribution at the resonance mass of 5 TeV for qq,qg, and gg resonance sample.	116

LIST OF TABLES

<u>Table</u>	<u>Page</u>
1.1 Searches for dijet resonances at hadron colliders. For each search we list the experiment, year of publication, center-of-mass energy, integrated luminosity, techniques used to define the resonance shape and the background.	4
2.1 Leading order matrix elements for 2-to-2 massless parton subprocesses . .	14
2.2 Properties of some resonance models	16
2.3 The decay modes and branching ratios of excited up and down quarks for $f_s = f = f'$ and $\alpha_s = 0.1$	17
3.1 Summary of the LHC parameters (Vidal and Manzano, 2007)	27
5.1 The data set used in this analysis with corresponding runs range and integrated luminosity	59
5.2 Full datasets for the background with number of events, cross-section, and corresponding luminosity	60
5.3 Tight Jet ID criteria that recommended from CMS (Rauco, 2017)	61
5.4 Table of jet energy correction (JEC) corresponding to each run period. . .	63
5.5 Triggers name used in this analysis and their definition.	64
6.1 The data sets for signal samples which used in this analysis, *XX stand for mass point which used 0.5 TeV and 1 to 9 TeV . *YY is stand for RunIISpring16MiniAODv2-PUSpring16_80X_mcRun2_asymptotic_2016_miniAOD_v0-v1/MINIAODSIM	73
6.2 The constraints associated to systematic uncertainty nuisance parameters.	81
6.3 The observed and expected upper mass limits at 95% CL on models of dijet resonances with corresponding luminosity is 35.9 fb^{-1} at $\sqrt{s} = 13 \text{ TeV}$.	84
6.4 Observed and Expected Upper Limits at 95% CL on $\sigma \times BR \times A$ for a gg resonance, a qg resonance, and qq resonance as a function of resonance mass with systematic uncertainties	85
6.4 Observed and Expected Upper Limits at 95% CL on $\sigma \times BR \times A$ for a gg resonance, a qg resonance, and qq resonance as a function of resonance mass with systematic uncertainties	86
7.1 The events selection summary for quark/gluon jet tagging search	91
7.2 The q/g jet tagging application strategy. Figure 7.3 shows LD operation points which we choose the apply and Figure 7.4 shows the optimal LD operation point as 0.5.	93

8.1 Observed and expected mass limits at 95% CL from this analysis with 35.9 fb^{-1} at $\sqrt{s} = 13$ TeV compared to previously published limits on narrow resonances from CMS with 12.9 fb^{-1} and 2.4 fb^{-1} at $\sqrt{s} = 13$ TeV and with 20 fb^{-1} at $\sqrt{s} = 8$ TeV. 106



1. INTRODUCTION

Particle physicists aspire to better understand the origin of the universe by trying to address a few questions. How did the Universe evolve? What is matter made of? How does matter stick together? Today, at CERN, we are going back in time to answers those questions. According to the theories, the Universe is born from the extremely hot Big Bang, producing a dense soup called quark-gluon plasma (QGP). The Large Hadron Collider (LHC) can reproduce the QGP by accelerating and colliding together two beams of protons or heavy ions. These collisions produce a very similar energy density and temperature that existed a few moments after the Big Bang. For this, particle physics studies the tiny and fundamental particles of nature and their interactions, explained by Standard Model (SM). According to the theory, which is supported by a great deal of experimental evidence, quarks and leptons are the building blocks of matter and forces act through carrier particles exchanged between the particles of matter. Standard Model explains three fundamental forces. These fundamental forces are strong, electromagnetic, and weak forces. The gravitational force plays a vital role in nature, but this remains negligible in atomic and nuclear physics scale. One of the possible goals of fundamental physics is to combine all natural forces to a set of fundamental laws called the theory of everything by theories.

One of the most important experimental contributions to the SM comes from the discovery of Higgs boson in July 2012. CERN announced the discovery of the Higgs boson, which confirmed the existence of the Higgs mechanism. The theory was published in 1964 by Robert Brout, François Englert, and Peter Higgs, that explains the origin of mass. However, observing the Higgs boson is not the end of the story, and researchers have to study the Higgs boson in detail to measure its properties. Our current understanding of the Universe is not complete. The SM of particles and forces indicate our present knowledge of particle physics. The SM has been tested by many experiments, and it has proven particularly successful in anticipating the existence of previously undiscovered particles. However, it leaves many unsolved questions, which the LHC may help to answer. Theories which are called the Beyond the Standard Model

(BSM), answer those unsolved questions and more. In general, we are looking for a sign of new physics that comes from those BSM theories. For instance, Supersymmetry is looking for an explanation why particles have mass. For this, Supersymmetry predicts a partner particle for each particle in the Standard Model. Extra dimensions could explain why gravity is so weak. Compositeness theories are looking for possible substructure for subatomic particles. All these theories are telling a story, coming up with ideas about how something may happen that we need to engage this idea with the experimental results to prove or disprove it.

These unanswered questions of the Standard Model lead us to the search to BSM. Most of BSM searching a new physics sign with a short-lived particle called resonance. Most researchers look for BSM particles through a method known colloquially as “bump-hunting,” where a mass resonances of unknown particles are searched for. In this thesis, we are also searching the new particles that are predicted by BSM. These new particles are produced by s-channel production which is the fusion or annihilation of two partons to an intermediary particle. As the intermediary particle is produced from colored particles, it can also decay to colored particles resulting production of jets. In this search, the invariant dijet mass spectrum is used to search for existence of the new particle.

Our experimental approach is to search for dijet resonances using the dijet mass spectrum measurement in data. The dijet event selection requires two back-to-back high P_T jets to measure dijet invariant mass spectrum. If a resonance exists, it should appear in the dijet mass spectrum as a bump like shown in Figure 1.1. First, we compare the dijet mass spectrum to QCD predictions from PYTHIA to see if they agree. Next, we fit the dijet mass spectrum with a smooth parameterization to see whether we can get a good fit. We look at the difference between the data and the fit then estimate the significance of any bump in the data. If there is no significant evidence for dijet resonances, we proceed to set limits. The dijet resonance shape for generic di-parton resonances containing qq, qg and gg parton pairs were simulated using PYTHIA8 as resonance signals. To calculate the upper cross section limit for this dijet resonance shape in our data, we perform a binned maximum likelihood method. We convolute the statistical likelihood distribution with

our Gaussian systematic uncertainty and find the 95% confidence level upper limit on the cross-section. This calculation gives cross section limits for generic narrow qq , qg and gg resonances, independent of any specific resonance model.

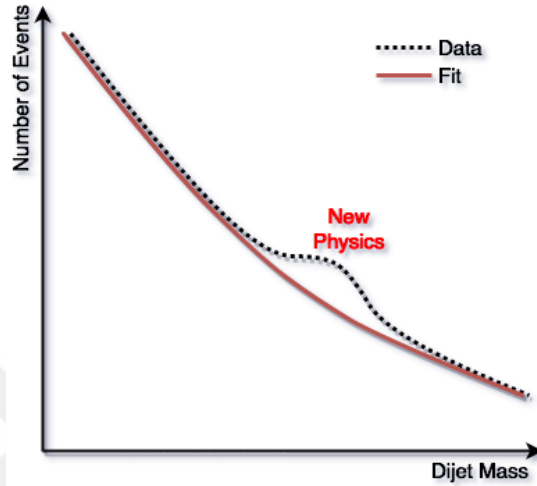


Figure 1.1: An illustration of the 'bump hunt' analysis strategy. If an excess is observed in the dijet mass distribution, it can be interpreted as a signal caused by a new massive resonance at that mass value.

New physics searches using the dijet event topology have been performed with CERN S $\bar{p}p$ S which is proton-antiproton colliders and the Fermilab Tevatron colliders with center of mass (\sqrt{s}) energies of up to 0.63 and 1.96 TeV , respectively. The available dijet mass range for the UA1 and UA2 experiments at S $\bar{p}p$ S was roughly 50 to 300 GeV and that of the CDF and D0 experiments at Tevatron around 0.2 to 1.3 TeV . Since the successful start of the LHC in 2010, many dijet searches with proton-proton collisions have been performed and published by both ATLAS (Aad, 2010) (Abbott, 2011) (Zwalinski, 2012) and CMS (Khachatryan, 2010) (Ozturk,2011) Collaborations, and the analyses are updated during the 2012–2013 at $\sqrt{s} = 8$ TeV collision data in the publication by ATLAS (Bell, 2015) and publications by CMS. (Bakirci, 2013) (Topakli,2013) (Chatrchyan, 2015). The results with $\sqrt{s} = 13$ TeV LHC Run 2 also published both ATLAS (Aaboud, 2017) and CMS (Bat,2015). In this search, we also perform 2016 CMS Run2 data at $\sqrt{s} = 13$ TeV with corresponding luminosity

35.9 fb⁻¹. Table 1.1 summaries the searches for dijet resonances at different hadron colliders from beginning to today.

Table 1.1: Searches for dijet resonances at hadron colliders. For each search we list the experiment, year of publication, center-of-mass energy, integrated luminosity, techniques used to define the resonance shape and the background.

Experiment	Year	\sqrt{s} (TeV)	$\int \text{Ldt}$ (pb ⁻¹)	Resonance Shape	Background Shape
UA1	86	0.63	0.26	BW \oplus Gaussian	LO QCD
UA1	88	0.63	0.49	BW \oplus Gaussian	LO QCD
CDF	90	1.8	0.026	BW \oplus Gaussian	LO QCD
UA2	90	0.63	4.7	Gaussian	Fit Func.
CDF	93	1.8	4.2	BW \oplus Gaussian	LO QCD
UA2	93	0.63	11	Gaussian	Fit Func.
CDF	95	1.8	19	PYTHIA \oplus Sim	Fit Func.
CDF	97	1.8	106	PYTHIA \oplus Sim	Fit Func.
D0	04	1.8	109	PYTHIA \oplus Sim	NLO QCD
CDF	09	1.96	1130	PYTHIA \oplus Sim	Fit Func.
ATLAS	10	7	0.32	PYTHIA \oplus Sim	Fit Func.
CMS	10	7	02.9	PYTHIA \oplus Sim	Fit Func.
ATLAS	11w	7	36	PYTHIA \oplus Sim	Fit Func.
			$\int \text{Ldt}$ (fb ⁻¹)		
CMS	11	7	1	PYTHIA \oplus Sim	Fit Func.
ATLAS	11s	7	1	PYTHIA \oplus Sim	Fit Func.
ATLAS	12	8	20.3	PYTHIA \oplus Sim	Fit Func.
CMS	13	8	4.0	PYTHIA \oplus Sim	Fit Func.
CMS	15	8	19.7	PYTHIA \oplus Sim	Fit Func.
ATLAS	16	13	15,7	PYTHIA \oplus Sim	Fit Func.
CMS	16	13	12.9	PYTHIA \oplus Sim	Fit Func.
ATLAS	17	13	37	PYTHIA \oplus Sim	Fit Func.
CMS	16	13	36	PYTHIA \oplus Sim	Fit Func.

2. THEORY OF PARTICLE PHYSICS

2.1 The Standard Model of Particle Physics

The Standard Model describes all known fundamental particles and their interactions with three of four known fundamental forces of nature. These forces are electroweak, strong, and weak force. Quantum Chromodynamics (QCD) explains the interaction of the colored (quark, gluon) particles through the exchange of the gluons. Electroweak (EW) theory combines Electromagnetic and weak Interactions. Electromagnetism explains the electrically charged particles interact with exchanging of photons. The weak force explains the interaction of the flavored (fermions) particles through the exchange of the W^\pm and Z^0 bosons. The Lagrangian of the SM expresses as a sum of EW and QCD in Equation 2.1 (Griffiths,2008).

$$\mathcal{L}_{SM} = \mathcal{L}_{EW} + \mathcal{L}_{QCD} \quad (2.1)$$

The SM is a quantum field theory and is described using group theory notation as $SU(3) \times SU(2) \times U(1)$. The $SU(3)$ is the gauge group of the strong interaction and generates eight types of gluons as the quanta of the gauge field. The $SU(2) \times U(1)$ is the gauge group of the electroweak interaction. The $SU(2)$ is the symmetry of the weak interaction and the $U(1)$ is the symmetry of QED. All particles incorporate in the weak interaction, all charged particles and the photon in the electromagnetic interaction and that only the quarks include in the strong interaction. Gravity is so weak that it can be neglected at subatomic scales (Botje,2013).

The Standard Model fundamental particles are of two kinds: fermions and bosons. The matter is formed from particles called fermions and the mediator of forces between matter interactions are called bosons. The fermions are divided into two groups: quarks that must bind together and the leptons that can exist freely. There are six flavors of quarks, which are up, down, strange, charm, top, and bottom. The quarks are known to

bind together into doubles or triples. The doubles are called the mesons ($q\bar{q}$), and the triples are called baryon (qqq). In a nutshell, baryons (the heavy triplets), mesons (the middleweight doublets), and quarks (the fundamental particles) are known as hadrons. The other six fermions are called leptons which are electron (e^-), muon (μ^-), tau (τ^-) and their neutrinos (ν_e, ν_μ, ν_τ). The known bosons are a photon, W^\pm , Z^0 , gluon, and Higgs. The particles of the Standard Model are shown in Figure 2.1.

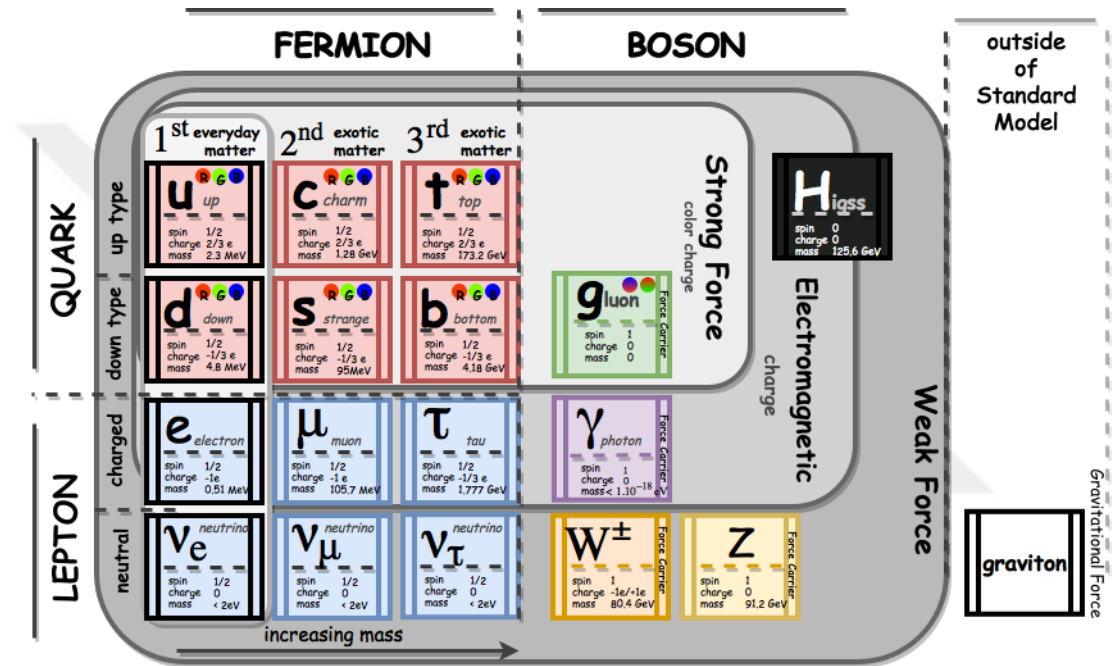


Figure 2.1: The particles of the Standard Model.

Every fundamental particle has an inherent spin that can be described in a discretized half-integer or integer quantum number. Fermions have half-integer spin quantum number ($1/2, 3/2, 5/2$, etc.), and bosons have integer spin quantum number ($0, 1, 2$, etc.). The force-carrying bosons of the SM (gluons, photon, and the W^\pm and Z^0) have spin 1 since they go with vector fields. The Higgs boson is the only scalar boson since has spin 0.

The Higgs boson was the missing part of the standard model until its discovery in 2012. All of space is assumed to be filled with a Higgs field. The particles moving around through space interact with this field that gives mass to elementary particles, and

this is called the Higgs mechanism and the particle that mediates the interaction is called the Higgs boson.

2.2 Quantum Chromodynamics (QCD)

QCD is the theory of the strong interaction based on the gauge field theory of the color SU(3), which makes QCD a non-Abelian theory. The force carrier of the theory is gluon, that is both colored and self-interacting. So, QCD is called a gauge theory, like the theory of the weak interactions and quantum electrodynamics (QED). In theory like this, the constituent fields are described by representations of symmetry group while the interaction between the fields is described by the exchange of gauge bosons.

Quantum Chromodynamics is defined as a field theory by its Lagrange density (Sterman,1995),

$$\mathcal{L}_{eff}^{QCD} [\psi_f(x), \bar{\psi}_f(x), A(x), c(x), \bar{c}(x); g, m_f] = \mathcal{L}_{invar} + \mathcal{L}_{gauge} + \mathcal{L}_{ghost}, \quad (2.2)$$

which is a function of fields [ψ_f (quark), A (gluon), and c (ghost)] and parameters are the gauge couplings (g) and the masses of the fermions (m_f), where f labels distinct quark fields. \mathcal{L}_{invar} is the classical Lagrangian density, which invariant under local SU(N_c) gauge transformations, with $N_c = 3$ for QCD. The classical Lagrangian density was originally written by Yang and Mills (Yang and Mills, 1954),

$$\begin{aligned} \mathcal{L}_{invar} &= \sum_f \bar{\psi}_f \left(i \not{D}[A] - m_f \right) \psi_f - \frac{1}{4} F^2[A] \\ &= \sum_{f=1}^{n_f} \sum_{\alpha, \beta=1}^4 \sum_{i, j=1}^{N_c} \bar{\psi}_{f, \beta, j} \left(i (\gamma)_{\beta\alpha}^\mu D_{\mu, ji}[A] - m_f \delta_{\beta\alpha} \delta_{ji} \right) \psi_{f, \alpha, i} \\ &\quad - \frac{1}{4} \sum_{\mu, \nu=0}^3 \sum_{a=1}^{N_c^2-1} F_{\mu\nu, a}[A] F_a^{\mu\nu}[A], \end{aligned} \quad (2.3)$$

In the Equation 2.3, we have written out all indices clarify, using the notations

$$D_{\mu,ij}[A] \equiv \partial_{\mu}\delta_{ij} + igA_{\mu a} (T_a^{(F)})_{ij} \quad (2.4)$$

$$F_{\mu\nu,a}[A] \equiv \partial_{\mu}A_{\nu a} - \partial_{\nu}A_{\mu a} - g C_{abc} A_{\mu b} A_{\nu c} . \quad (2.5)$$

In the Equation 2.5 , $F_{\mu\nu,a}$ is the non-Abelian field strength defined in terms of the gluon vector field A_b^{μ} with $N_c^2 - 1$ group components b . g is the QCD strong coupling and the C_{abc} , $a, b, c = 1 \dots N_c^2 - 1$, are real numbers, called the structure constants of $SU(N_c)$, which define its Lie algebra. N_c is called the number of colors. $D_{ij}^{\mu}[A]$ is the covariant derivative in the N_c - dimensional representation of $SU(N_c)$, which acts on the spinor quark fields in the Equation 2.4. There are n_f independent quark fields ($n_f = 6$ in SM), labeled by flavor $f (= u, d, c, s, t, b)$. In the QCD Lagrangian, they are distinguished only by their masses. The gauge invariance of \mathcal{L}_{invar} makes it somewhat difficult to quantize. This problem is solved by adding to \mathcal{L}_{gauge} and \mathcal{L}_{ghost} , as in Equation 2.2. The former may be chosen almost freely; the two most common choices being,

$$\mathcal{L}_{gauge} = -\frac{\lambda}{2} \sum_{a=1}^{N_c^2-1} (\partial_{\mu} A_a^{\mu})^2 \quad 1 < \lambda < \infty, \quad (2.6)$$

$$\mathcal{L}_{gauge} = -\frac{\lambda}{2} \sum_{a=1}^{N_c^2-1} (n \cdot A_a)^2 \quad \lambda \rightarrow \infty,$$

where n^{μ} is a fixed vector. The first defines the set of covariant gauges, the most familiar having $\lambda = 1$, the Feynman gauge. The second defines the axial or physical gauges, when $\lambda \rightarrow \infty$ eliminates the need for ghost fields. In the covariant gauges we must add a ghost Lagrangian which is given by Equation 2.7, and where $c_a(x)$ and $\bar{c}_a(x)$ are scalar ghost and anti-ghost fields.

$$\mathcal{L}_{ghost} = (\partial_{\mu} \bar{c}_a) (\partial^{\mu} \delta_{ad} - g C_{abd} A_b^{\mu}) c_d \quad (2.7)$$

2.2.1 Color factor in QCD

There are color charges in QCD similar to the electric charge in QED. However, QCD has three different color charges which are red (R), green (G), and blue (B). All observed particles are white or colorless particles, which colored particles can't be observed. Each quark carries one color and gluons carry a combination of color and anti-color. There are eight different gluon types, which formed from SU(3) octet. In Equation 2.4, the generators T is 3×3 matrices, which define the constant C_{abc} as the structure of SU(3) (Ellis,1996).

$$[t^A, t^B] = i C_{abc} T^c \quad (2.8)$$

The Normalization condition is equal to:

$$Tr (t^A, t^B) = T_F \delta^{AB} \quad (2.9)$$

$T_F = 1/2$ is chosen to fix the normalization of the matrices t_A which is equal to $t_A = \lambda^A/2$. Casimir operator C_F and C_A can be calculated specifically for SU(3) as follow:

$$\sum t_{ab}^A t_{bc}^A = C_F \delta_{ac}, \quad C_F = \frac{N^2 - 1}{2N}, \quad C_F = \frac{4}{3} \quad (2.10)$$

$$Tr T^C T^D = \sum_{A,B} f^{ABC} f^{ABD} = C_A \delta^{CD}, \quad C_A = N, \quad C_A = 3 \quad (2.11)$$

QCD leads us to two remarkable features: confinement and asymptotic freedom. The asymptotic freedom and confinement are two sides of the same coin. Asymptotic freedom indicates the weakness of short distance while the confinement of quark follows its strength at a long distance. A strong coupling constant characterizes the strength of the interaction which described as:

$$\alpha_s = \frac{g^2}{4\pi} \quad (2.12)$$

When the distance is short or equivalently the energy of the process is high, α_s approaches zero, meaning that the partons can move freely and not interact with other partons though the color force.

2.3 Hadron-Hadron Collision

When two hadrons collide, the actual collisions are between partons (quark, gluon) inside the proton. The theory of strong interaction (QCD) plays an essential role here. The hard scattering process can be examined in three part: first, incoming long distance hadrons in the beams. Second, the short distance scattering process and the third is the long-distance outgoing states. Figure 2.2 shows the hard scattering process in the hadron-hadron collisions (Ellis, 2007).

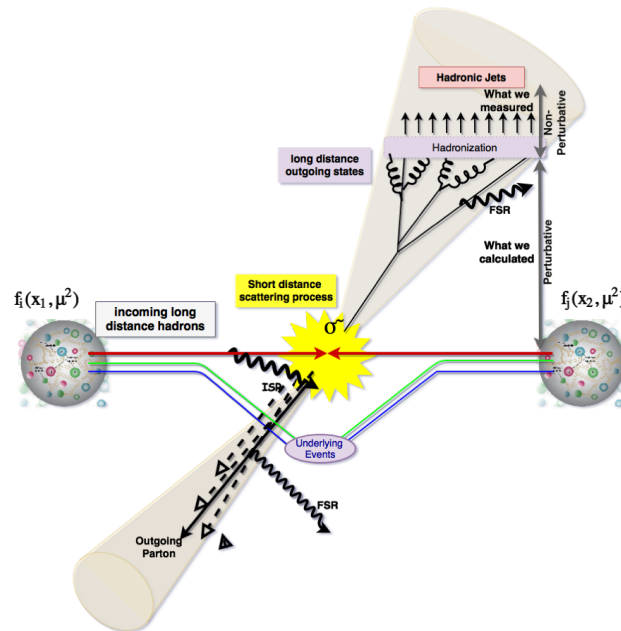


Figure 2.2: Hard scattering event in hadron-hadron collision

In the first part of the process, the QCD coupling is strong in the long distance which causes the color singlet states. The partons can emit radiation before the short distance scattering process yielding the as initial state radiation (ISR). The remnants of the original hadrons will interact, presumably softly, with each other generating underlying distribution of soft partons called underlying events (UE). In this step, the partons in beam picking out from to the short distance scattering depend on the parton distribution function (PDFs). The parton distribution functions $f_i(x, Q^2)$ give the probability densities to find a particular parton carrying a momentum fraction x at a squared energy scale (Q^2). Thus, this function defines total hadron momentum as a measure of how much is carried by a parton. In Figure 2.3 shows parton distribution functions for partons as a function of the momentum fraction x , at $Q^2 = 10 \text{ GeV}^2$ (on left) and $Q^2 = 10^4 \text{ GeV}^2$ (on right).

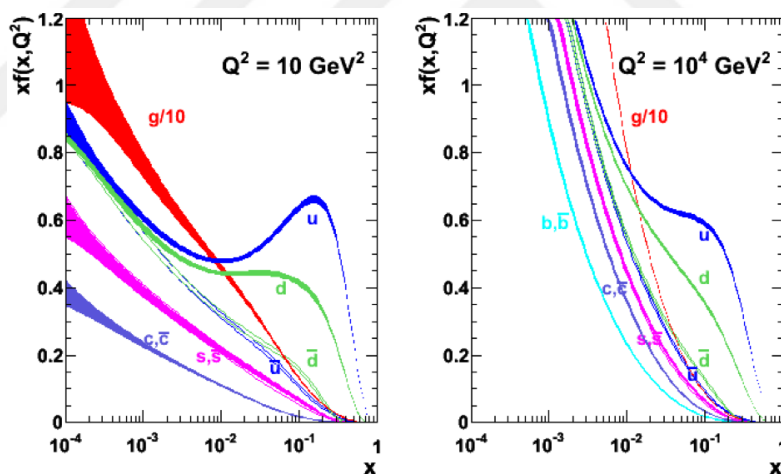


Figure 2.3: The parton distribution functions as a function of the momentum fraction x , at $Q^2 = 10 \text{ GeV}^2$ (on left) and $Q^2 = 10^4 \text{ GeV}^2$ (on right). This plots obtained from Particle Data Group (PDG)

Next comes to the short distance, large momentum transfer scattering process where strong coupling goes weak, meaning partons can move freely and do not interact each other. Each parton has a finite probability to split into two partons that are called parton shower (parton branching), and the probability of splitting depends on the color factor related to the type of the partons. The color factors are $C_{gg} = 3$ ($gluon \rightarrow gluon +$

gluon), $C_{qq} = 4/3$ (*gluon* \rightarrow *quark* + *anti-quark*), and $C_{qg} = 1/2$ (*quark* \rightarrow *gluon* + *quark*). As a result, gluons shower more than quarks. The parton shower is a perturbative process, and the cross-section for this step is calculated in a fixed order in perturbative QCD (pQCD), with the next-to-leading-order (NLO) or higher order.

The final part of the process is long distance outgoing states compromise a non-perturbative hadronization process. In this step, α_s goes strong again, meaning the strength of the interaction between colored particles increase, and results in confinement. The formation of hadrons out of quarks and gluons coming from parton shower continues until there is not enough energy to create new hadrons. This process is called hadronization. Figure 2.4 shows the schematic view of hadron-hadron collision and formation of jets. A jet is the experimental signature of a parton, described as a spray of hadrons. You may find more information in Section 4.

2.3.1 Hadronic cross section

The previous section describes the hard scattering process in a perfective view of experimental needs to be rephrased. In view of the theory, a hard scattering process between hadrons leads to us the definition of the cross-section which is a probability of a given process between initial states and final states. The cross-section for a hard scattering process is described as (Harris and Kousouris, 2011) :

$$\sigma(P_1, P_2) = \sum_{i,j} \int dx_1 dx_2 f_i(x_1, \mu^2) f_j(x_2, \mu^2) \tilde{\sigma}_{ij}(p_1, p_2, \alpha_s(\mu^2, Q^2/\mu^2)) \quad (2.13)$$

where P_1 and P_2 are 4-momenta for partons which join in the hard interaction and can be written as:

$$p_1 = x_1 P_1 \quad p_2 = x_2 P_2 \quad (2.14)$$

The functions $f_i(x, \mu^2)$ are parton distributions functions for quark and gluon defined at a factorization scale μ . Q is the characteristic scale of the hard scattering. σ_{ij}

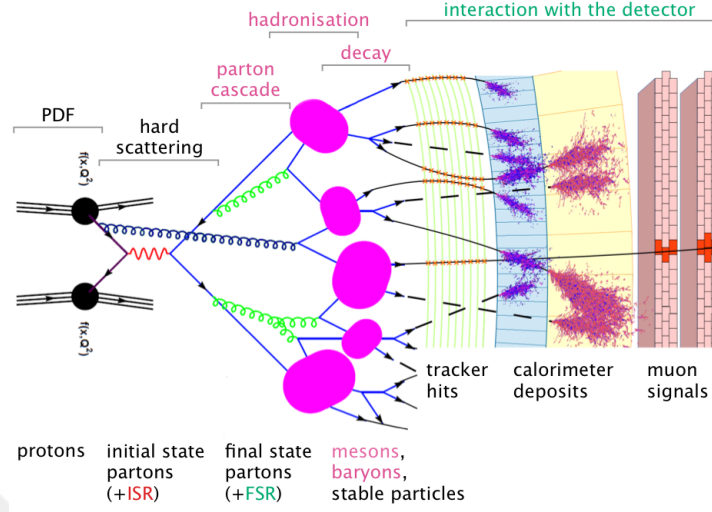


Figure 2.4: A schematic view of hadron-hadron collision

define the short distance cross-section. The cross-section of hard scattering can be calculated as a perturbative series of α_s because of strong coupling (α_s) is small at high energy and short distance.

The cross-section has a strong relation with Luminosity (L) of the machine, where L multiplied by the cross-section (σ) for the relevant scattering process gives us the number of events (N), which is described as $N = L \times \sigma$. The Luminosity of the machine for pp collider demonstrate by the collider parameters (Ellis,1996).

$$L = \frac{f N_p N_p}{\pi n_b} \frac{\gamma}{\sqrt{\beta_x^* \beta_y^* E_x^* E_y^*}}, \quad (2.15)$$

where n_b is a number of the bunch, f is the revolution frequency, $\gamma = E/m$ is the standard relativistic factor. N_p is the number of protons, which the increasing the number of protons increases the luminosity of the collider. E_x, E_y is the transverse emittance of the beams, and B_x, B_y is the wavelength of the physics of high energy collision. A description of the differential parton luminosity $dL_{ij}/d\tau$ can be written as:

$$\frac{dL_{ij}}{d\tau} = \int_0^1 \int_0^1 dx_1 dx_2 f_i(x_1) f_j(x_2) \delta(x_1 x_2 - \tau), \quad \tau = x_1 x_2 = \frac{\hat{s}}{s} \quad (2.16)$$

Table 2.1: Leading order matrix elements for 2-to-2 massless parton subprocesses

Subprocess	$\mathcal{S}(ij \rightarrow kl) = \frac{s^2}{\pi\alpha_s^2} \frac{d\hat{\sigma}}{d\hat{t}}(ij \rightarrow kl)$
$q_1 q_2 \rightarrow q_1 q_2$	$\frac{4}{9} \frac{\hat{s}^2 + \hat{u}^2}{\hat{t}^2}$
$q_1 \bar{q}_2 \rightarrow q_1 \bar{q}_2$	$\frac{4}{9} \frac{\hat{s}^2 + \hat{u}^2}{\hat{t}^2}$
$qq \rightarrow qq$	$\frac{4}{9} \left(\frac{\hat{s}^2 + \hat{u}^2}{\hat{t}^2} + \frac{\hat{s}^2 + \hat{t}^2}{\hat{u}^2} \right) - \frac{8}{27} \frac{\hat{s}^2}{\hat{u}\hat{t}}$
$q_1 \bar{q}_2 \rightarrow q_2 \bar{q}_2$	$\frac{4}{9} \frac{\hat{t}^2 + \hat{u}^2}{\hat{s}^2}$
$q\bar{q} \rightarrow q\bar{q}$	$\frac{4}{9} \left(\frac{\hat{s}^2 + \hat{u}^2}{\hat{t}^2} + \frac{\hat{s}^2 + \hat{t}^2}{\hat{u}^2} \right) - \frac{8}{27} \frac{\hat{u}^2}{\hat{s}\hat{t}}$
$q\bar{q} \rightarrow gg$	$\frac{32}{27} \frac{\hat{t}^2 + \hat{u}^2}{\hat{t}\hat{u}} - \frac{8}{3} \frac{\hat{t}^2 + \hat{u}^2}{\hat{s}^2}$
$gg \rightarrow q\bar{q}$	$\frac{1}{6} \frac{\hat{t}^2 + \hat{u}^2}{\hat{t}\hat{u}} - \frac{3}{8} \frac{\hat{t}^2 + \hat{u}^2}{\hat{s}^2}$
$gq \rightarrow gq$	$-\frac{4}{9} \frac{\hat{s}^2 + \hat{u}^2}{\hat{s}\hat{u}} + \frac{\hat{u}^2 + \hat{s}^2}{\hat{t}^2}$
$gg \rightarrow gg$	$\frac{9}{2} \left(3 - \frac{\hat{t}\hat{u}}{\hat{s}^2} - \frac{\hat{s}\hat{u}}{\hat{t}^2} - \frac{\hat{s}\hat{t}}{\hat{u}^2} \right)$

In practice, experimental constraints are imposed on the rapidities of the outgoing partons, observed as hadronic jets. For this reason, it is more proper way to express the parton luminosity as a functions of the variables τ and \bar{y} , rather than $x_{1,2}$:

$dx_1 dx_2 = \frac{\partial(\tau, \bar{y})}{\partial x_{1,2}} d\tau d\bar{y}$. The parton luminosity becomes:

$$\frac{dL_{ij}(\bar{y}_{min}, \bar{y}_{max})}{d\tau} = \int_{\bar{y}_{min}}^{\bar{y}_{max}} f_i(\sqrt{\tau} e^{\bar{y}}) f_j(\sqrt{\tau} e^{-\bar{y}}) d\bar{y} \quad (2.17)$$

The hadronic cross section of any process can be described in general as a function of the parton luminosity factor and the partonic cross section:

$$\sigma_{had} = \sum_{i,j} \int \frac{d\tau}{\tau} \left[\frac{1}{s} \frac{dL_{ij}}{d\tau} \right] [\hat{s} \hat{\sigma}_{ij}] \quad (2.18)$$

In the particular situation of a two-to-two scattering, resulting in the production of two jets, the differential cross section can be described as a function of the two parton invariant mass and the scattering angle at the center-of-mass frame. To a first approximation, this cross-section is equal to the observed dijet cross section. The matrix elements presented in Table 2.1 that shows leading order matrix elements for 2-to-2 massless parton subprocesses are folded with the parton distribution functions, giving:

$$\frac{d^2\sigma_{had}}{dm d\cos\theta^*} = \frac{\pi\alpha_s^2}{m} \sum_{ij} \left[\frac{1}{s} \frac{dL_{ij}}{d\tau} \right]_{\tau=m^2/s} \hat{F}_{ij}(\cos\theta^*), \quad (2.19)$$

where $m \approx \sqrt{\hat{s}} = \sqrt{\tau s}$.

$$\hat{F}_{ij}(\cos\theta^*) = \sum_{kl} \mathcal{S}(ij \rightarrow kl) \frac{1}{1 + \delta_{kl}} \quad (2.20)$$

2.4 Dijet Resonance Models

The Standard model is the most powerful theory to date describing nature, and so far, all the experimental results support the Standard Model. However, Standard Model does not provide complete answers to all our questions, such as: Why are there exactly three generations of quarks and leptons? Are quarks and leptons fundamental, or made up of even more fundamental particles? Why is there so much more matter than antimatter in the Universe? How do we unify gravity with the other forces? Why is gravity so weak?

The Standard Model is not the end of the story. There are a Beyond Standard Model theories that try to answer those question. These new theories usually predict resonances, and these new particles may show themselves in the pp collision with an extremely short lifetime. Table 2.2 shows properties of some resonance models decaying to two partons in final states, resulting in two jets. The basic idea of the new physics searches with dijet

events is to reconstruct a dijet mass spectrum from the events with back to back highest P_T jets called dijets and looks for resonances as a bump on dijet mass spectrum.

Table 2.2: Properties of some resonance models

Model Name	Symbol	Color Multiplet	J^P	$\Gamma/(2M)$	Decay Channel
Excited Quark	q^*	Triplet	$1/2^+$	0.02	qg
E_6 Diquark	D	Triplet	0^+	0.004	qq
Axigluon	A	Octet	1^+	0.04	$q\bar{q}$
Coloron	C	Octet	1^-	0.04	$q\bar{q}$
Color Octet Scaler	S_8	Octet	0^+	0.03	gg
Heavy W	W'	Singlet	1^-	0.01	$q\bar{q}$
Heavy Z	Z'	Singlet	1^-	0.01	$q\bar{q}$
RS Graviton	G	Singlet	2^-	0.01	$q\bar{q}, gg$

Diquarks (D) are predicted by E_6 grand unified models, and decay channel is quark-quark. Chiral color, which extends QCD predict axigluon (A) and Coloron (C). Models that include new gauge symmetries predict W' and Z' bosons. RS model of extra dimensions predicts RS Graviton (G). Axigluon, Coloron, W' and Z' bosons and RS Graviton decay channel is quark-antiquark parton pair. RS Graviton also decays gluon-gluon parton pair channel. String resonance is Regge excitations of quarks and gluons in string theory. Excited quark (q^*) is predicted the compositeness theory looking for whether quarks are a composite object or not, String resonance and Excited quark models decay channel is quark-gluon parton pair channel. String resonance (S) also decay to the $q\bar{q}, gg$ but a predominantly qg channel. And last resonance model is S_8 which is predicted in a technicolor model, and decay channel is gluon-gluon. The calculation and the details of these models are discussed in the following subsection.

2.4.1 Excited quark

As far as we know, quarks are a fundamental particle in SM, but there is a Beyond the Standard Model theory search for evidence that quarks are composite particles, meaning quarks are made up of something smaller. If quarks are composite particles, then excited states are expected, which is called excited quark and denoted by

q^* . We simply consider a kind of excited quark, one with spin 1/2 and weak isospin 1/2. The Lagrangian of the excited quark form as (Baur,1987):

$$\mathcal{L} = \frac{1}{\Lambda} \bar{q}_R^* \sigma^{\mu\nu} \left(g_s f_s t_a G_{\mu\nu}^a + g f \frac{\vec{\tau} \cdot \vec{W}_{\mu\nu}}{2} + g' f' \frac{Y}{2} B_{\mu\nu} \right) q_L + h.c \quad (2.21)$$

where $G_{\mu\nu}^a$, $\vec{W}_{\mu\nu}$, $B_{\mu\nu}$ are the field tensors t_a and $\vec{\tau}$ are the generators of the color SU(3) and isospin SU(2), g_s and g' are the gauge couplings, Y is the hypercharge, and f_s, f, f' are dimensionless constants, accounting for possible deviations from the SM couplings.

In hadron collisions, the production of an excited quark happens through the quark-gluon fusion. Afterwards, the excited quark decays to an ordinary quark and a gauge boson. The dominant decay channel is $q^* \rightarrow qg$, which is leading to a dijet signature. The partial width (Γ) for the decay of an excited quark with mass m^* is written as:

$$\Gamma (q^* \rightarrow qg) = \frac{1}{3} \alpha_s f_s^2 \frac{m^{*3}}{\Lambda^2} \quad (2.22)$$

The relative decay modes and branching ratios of excited up and down quarks are shown in Table 2.3 (Harris,2006).

Table 2.3: The decay modes and branching ratios of excited up and down quarks for $f_s = f = f'$ and $\alpha_s = 0.1$.

Decay Mode	Branching Ratio (%)	Decay Mode	Branching Ratio (%)
$u^* \rightarrow ug$	83.4	$d^* \rightarrow dg$	83.4
$u^* \rightarrow u\gamma$	2.2	$d^* \rightarrow d\gamma$	0.5
$u^* \rightarrow uW$	10.9	$d^* \rightarrow dW$	10.9
$u^* \rightarrow uZ$	3.5	$d^* \rightarrow dZ$	5.1

2.4.2 Randall-Sundrum gravitons

The Randall-Sundrum (RS) Graviton model was proposed as a solution to the Electroweak vs. Planck scale hierarchy problem. The hierarchy problem arises from the

vast discrepancy between Electroweak scale (~ 1 TeV) and Planck scale (10^{19} GeV). In this model, the hierarchy is produced by an exponential function of the compactification radius of one extra dimension. The metric in the 5-dimensional space is given by (Randall and Sundrum, 1999):

$$ds^2 = e^{-2kr_c\phi} \eta_{\mu\nu} x^\mu x^\nu + r_c^2 d\phi^2, \quad (2.23)$$

where k is a constant of the same order and related to the 5-dimensional Planck scale M , ϕ is the extra dimension with compactification radius r_c , x^μ are the space-time dimensions. The reduced effective 4D Planck scale \bar{M}_{Pl} is written as:

$$\bar{M}_{Pl}^2 = \frac{M^3}{k} (1 - e^{-2kr_c\pi}) \quad (2.24)$$

In RS Graviton (RSG) model, spin-2 gravitons look like the Kaluza-Klein (KK) excitations of the gravitational field $h_{\mu\nu}$, whose coupling to the Standard-Model fields is given by the interaction Lagrangian:

$$\mathcal{L}_I = -\frac{1}{\Lambda_\pi} h^{\mu\nu} T_{\mu\nu} \quad (2.25)$$

with $T_{\mu\nu}$ being the energy-momentum tensor of the matter fields. The scale Λ_π and the mass m_n of the Kaluza-Klein (KK) excitations can be expressed as a function of the fundamental constants of the theory:

$$\Lambda_\pi = \bar{M}_{Pl} e^{-kr_c\pi}, \quad m_n = k x_n e^{-kr_c\pi} \quad (2.26)$$

The coupling constant of the graviton-matter interaction is the inverse of the scale Λ_π :

$$g = \frac{1}{\Lambda_\pi} = x_n \frac{(k/\bar{M}_{Pl})}{m_n}, \quad (2.27)$$

where x_n is the n-th root of the Bessel function of order 1. In many simplified models, the two parameters of interest are the mass and the coupling strength parameter k/\bar{M}_{Pl} . If the fundamental constants of the model satisfy the relation $k_{rc} \sim 12$, then $\Lambda_\pi \sim \text{TeV}$, and RSG can show up in hadron collisions. Through the Graviton coupling to the matter fields, RSG can decay to two partons, leading to a dijet signature.

In the narrow width approximation, the lowest order differential cross section for the spin-2 Graviton resonance of mass M and width Γ per unit of center-of-mass scattering angle $\cos \theta$ and boost η is given by (Harris,2006):

$$\frac{d\sigma}{d\cos\theta d\eta_B} = \frac{1}{C_i} \left(\frac{2M\pi}{s} \frac{\Gamma}{2} \right) \left(\frac{20\pi}{M_2} B_i B_f \frac{1}{C_i} \right) F(\cos\theta^*) f(x_p) f(x_{\bar{p}}) \quad (2.28)$$

where s is the square of the proton-proton collision energy, $\eta_B = (\eta_1 + \eta_2)/2$ is the average pseudorapidity of the final state partons, B_i and B_f are the branching fractions for the initial state and the final state respectively, C_i is the color of the initial state (8 for gg and 3 for $q\bar{q}$), $f(x_p)$ and $f(x_{\bar{p}})$ are the parton distributions of the initial state, and the $F(\cos\theta^*)$ are the normalized angular distributions of the sub-process:

$$\begin{aligned} F(gg \rightarrow G \rightarrow q\bar{q}) &= F(q\bar{q} \rightarrow G \rightarrow gg) = \frac{5}{8}(1 - \cos^4 \theta) \\ F(gg \rightarrow G \rightarrow gg) &= \frac{5}{32}(1 + 6 \cos^2 \theta + \cos^4 \theta) \\ F(q\bar{q} \rightarrow G \rightarrow q\bar{q}) &= \frac{5}{8}(1 - 3 \cos^2 \theta + 4 \cos^4 \theta) \end{aligned} \quad (2.29)$$

In Equation 2.28, the cross-section for a Breit-Wigner narrow resonance properly weighted by the initial and final state branching fractions. The final state branching fractions are given by the ratio of the partial widths to the full widths, the partial width for the final state gg and qq can be written by:

$$\Gamma(G \rightarrow gg) = \frac{x_1^2}{10\pi} \left(\frac{k}{\bar{M}_{Pl}} \right)^2 m_1$$

$$\Gamma(G \rightarrow q\bar{q}) = \frac{3x_1^2}{160\pi} \left(\frac{k}{\bar{M}_{Pl}} \right)^2 m_1$$
(2.30)

2.4.3 Axigluon

In the models of chiral color, the unbroken color symmetry $SU(3)_C$ of QCD results from the breaking of the larger chiral color group $SU(3)_L \times SU(3)_R$. In a symmetry group like this, the left-handed and right-handed fermions $\psi_{L,R} = 1/2(1 \mp \gamma_5)$ transform differently and the transformations are generated by the $T_{L,R}^a$ generators. Equally, the group can be defined by a linear transformation of the generators, divided into vectorial $T_V^a = T_L^a + T_R^a$ and axial $T_A^a = T_L^a - T_R^a$ ones. The relevant gauge field to the vectorial generators is identified as the usual color field of QCD, while the gauge field relevant to the axial generators is called the axigluon field. While the exact application of the chiral color group is model dependent, there are two universal features: the existence of a massive color octet axigluon field (corresponding to the broken symmetry), and the existence of new particles which are needed to cancel the triangular anomalies (Bagger,1988).

Axigluons are generated and decay strongly from quark-antiquark interactions, giving one of the largest cross section times branching ratio of any of the models considered. They can not decay into a gluon-gluon pair because of parity conservation. The axigluon decay to fermions is described by the Lagrangian:

$$\mathcal{L}_A = -ig_s \left(\sum_{i,j} \bar{q}_i \gamma_5 \gamma_\mu t_a q_j \right) \mathcal{A}^{a\mu},$$
(2.31)

where \mathcal{A} is the axigluon field, $g_s = \sqrt{4\pi\alpha_s}$, and t^a are the usual color group generators. The width of the axigluon decay given by:

$$\Gamma_A = \frac{N \alpha_s M_A}{6}, \quad (2.32)$$

where α_s is the strong coupling constant, M_A is the axigluon mass, and N refers to the number of open decay channel. The N range from 6 to 18, where the factor of 6 comes from the 6 quark flavors currently in the Standard Model. Because of top quark, the branching ratio of the axigluon needs a correction. When $M_A < 2M_t$ the branching ratio to light quarks (u, d, s, c, b) is 1 and when $M_A > 2M_t$ the branching ratio is taken to be:

$$BR(A \rightarrow q\bar{q}) = \frac{1}{5 + [1 + (2M_t/M_A)^2]^{3/2}} \quad (2.33)$$

2.4.4 Colorons

In flavor-universal coloron model where the gauge group is extended to $SU(3)_1 \times SU(3)_2$. The corresponding gauge couplings are denoted as $\xi_{1,2}$. In addition, the model includes a scalar boson ϕ , which develops a non-zero vacuum expectation value and breaks the symmetry of the two groups spontaneously. The diagonal subgroup remains unbroken and is identified as the familiar color group of QCD. In the rotated phase of the physical gauge fields, the initial gauge bosons are mixed, forming an octet of massless gluons and an octet of massive colorons. The mass of the colorons is expressed as a function of the fundamental parameters (Elizabeth,1997):

$$M_c = \left(\frac{g_s}{\sin \theta \cos \theta} \right) f \quad (2.34)$$

where f is the vacuum expectation value of the scalar field, and θ is the gauge boson mixing angle with $\cot \theta = \xi_2/\xi_1$. The Lagrangian of the interaction between the colorons

field $C^{\mu a}$ and the quarks is similar to QCD:

$$\mathcal{L} = -g_s \cot \theta \left(\sum_{i,j} \bar{q}_i \gamma_\mu t_a q_j \right) C^{\mu a} \quad (2.35)$$

where $\cot \theta$ is expected to have a value $\cot \theta \geq 1$ because of the mixing parameter of the two SU(3). The colorons decay to all sufficiently light quarks; assuming there are n flavors lighter than $M_c/2$, the decay width is given by:

$$\Gamma_c \approx \frac{n}{6} \alpha_s \cot^2 \theta M_c \quad (2.36)$$

The flavor universal coloron is thus a massive gluon which couples equally to all quarks. It is obvious that for the value of mixing $\cot \theta = 1$ the coloron has the same width as the axigluon, the same coupling strength to quarks as the axigluon, and the same production cross sections times branching ratio for jets.

2.4.5 Color octet scalars

In various theoretical models, bosonic states can come out of gluon-gluon fusion. The color octet scalar model (S_8) is one example of an exotic color resonances. The coupling of the color octet scalar field with gluons is described with the Lagrangian (Han, 2010):

$$\mathcal{L} = g_s \frac{\mathcal{K}}{\Lambda} d^{abc} S_8^a G_{\mu\nu}^b G^{c,\mu\nu} \quad (2.37)$$

where \mathcal{K} is the scalar coupling, g_s is the strong coupling, Λ is the characteristic scale of the interaction, d^{abc} are structure constants of the SU(3) group identified by the relation $\{t^a, t^b\} = \frac{1}{3}\delta^{ab} + d^{abc}t^c$, S_8 is the color octet scalar field, and $G_{\mu\nu}$ is the gluon field tensor.

The width of the color octet scalar resonance can be written as :

$$\Gamma = \frac{5}{6} \alpha_s \mathcal{K}^2 \frac{M^3}{\Lambda^2} \quad (2.38)$$

2.4.6 Z' and W'

New gauge bosons take shape in models where the symmetry $SU(2)_L \times U(1)_Y$ of the electroweak SM sector is expanded. Common features in these models are the new gauge coupling constants, which tend to be of the same order as the $SU(2)_L$ coupling of the SM, and the existence of new gauge bosons, namely W' and Z' . We assume the W' has the same production cross section as the W (with M_W replaced by $M_{W'}$) and the same fractional width as the W . The same relations keep between the Z' and the Z . In addition, under such a hypothesis that the new gauge bosons couple to ordinary quarks and leptons similar to their SM counterparts, the cross-sections of these particles are calculated by scaling the corresponding SM cross-section with a new Fermi constant, G_F , replaced by (Eichten,1984):

$$G'_F = G_F \left(\frac{M}{M'} \right)^2, \quad (2.39)$$

where M is the mass of the W or Z and M' is the mass of the W' or Z' , respectively. Z' and W' half widths are significantly less than our dijet mass resolution and the half width of the W' and the half width of the Z' given by,

$$\frac{\Gamma}{2} = \frac{2 \text{ GeV}}{2} \frac{M'_W}{M_W}, \quad \frac{\Gamma}{2} = \frac{2 \text{ GeV}}{2} \frac{M'_Z}{M_Z} \quad (2.40)$$

2.4.7 E₆ Diquarks

E₆ are suggested by Beyond the Standard Model, such as the superstring- inspired E₆ models and composite models. If the string gauge is E₈ × E₈, 10-dimensional string theory is required to be free of gauge and gravitational anomalies. The compactification of the extra 6 dimensions can lead to E₆ as the grand unification group for the strong and electroweak interactions. The E₆ models contain color triplet scalar diquarks D (D^c) with charge $-1/3$ ($+1/3$) which couple to $\bar{u}\bar{d}$ (ud).

The interaction Lagrangian for transitions between E₆ diquarks and light quarks is (Angelopoulos,1987):

$$\mathcal{L}_D = \lambda \epsilon_{ijk} \bar{u}^{ci} \frac{1}{2} (1 - \gamma_5) d^j D^k + \frac{\lambda_c}{2} \epsilon_{ijk} \bar{u}^i \frac{1}{2} (1 + \gamma_5) d^{cj} D^{ck} + h.c. \quad (2.41)$$

where λ, λ_c are parameters of the hyper-potential of the general E₆, and i, j, k are color indices. The squared amplitudes for the diquark decays to light quarks are given by:

$$|\mathcal{M}(D \rightarrow \bar{u}\bar{d})|^2 = 24 \lambda^2 m_D^2, \quad |\mathcal{M}(D^c \rightarrow ud)|^2 = 6 \lambda_c^2 m_{D^c}^2 \quad (2.42)$$

The corresponding widths are:

$$\begin{aligned} \Gamma &= \alpha_\lambda M_D, \quad \alpha_\lambda = \frac{\lambda^2}{4\pi} \\ \Gamma_{D^c} &= \frac{1}{4} \alpha_{\lambda_c} M_{D^c}, \quad \alpha_{\lambda_c} = \frac{\lambda_c^2}{4\pi} \end{aligned} \quad (2.43)$$

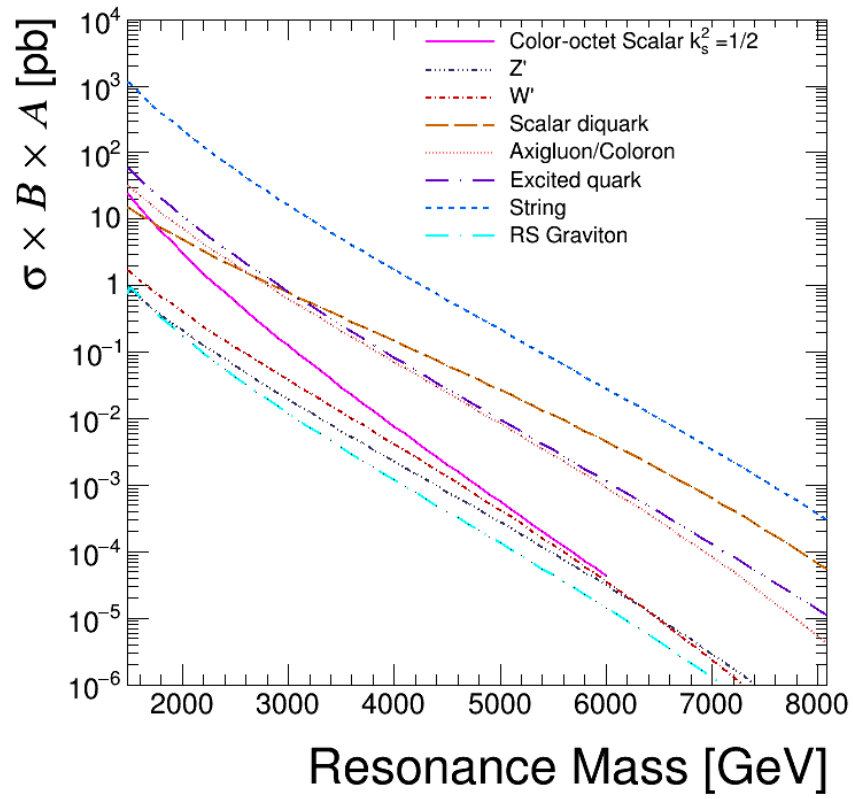


Figure 2.5: The cross-section for dijet resonances with $|\eta| < 2.5$ & $|\Delta\eta| < 1.3$ is shown as a function of resonance mass for the following models: excited quark, axigluon/coloron, scalar diquark, color-octet-scalar ($k_s^2=1/2$), String, RS Graviton W' , and Z' .

3. EXPERIMENTAL APPARATUS

3.1 The Large Hadron Collider

The Large Hadron Collider (LHC) at CERN is the world's largest and the most powerful particle accelerator ever built. The LHC reuses the 27 km circumference tunnel that was built for CERN's previous big accelerator, LEP (Large Electron-Positron) collider, which finished running in 2000, located on the French-Swiss national border near Geneva. The tunnel was built with a mean depth of 100 m, because of the geological considerations. Its depth varies between 175 m under the Jura and 50 m towards Lake Geneva (Anonym, 2017).

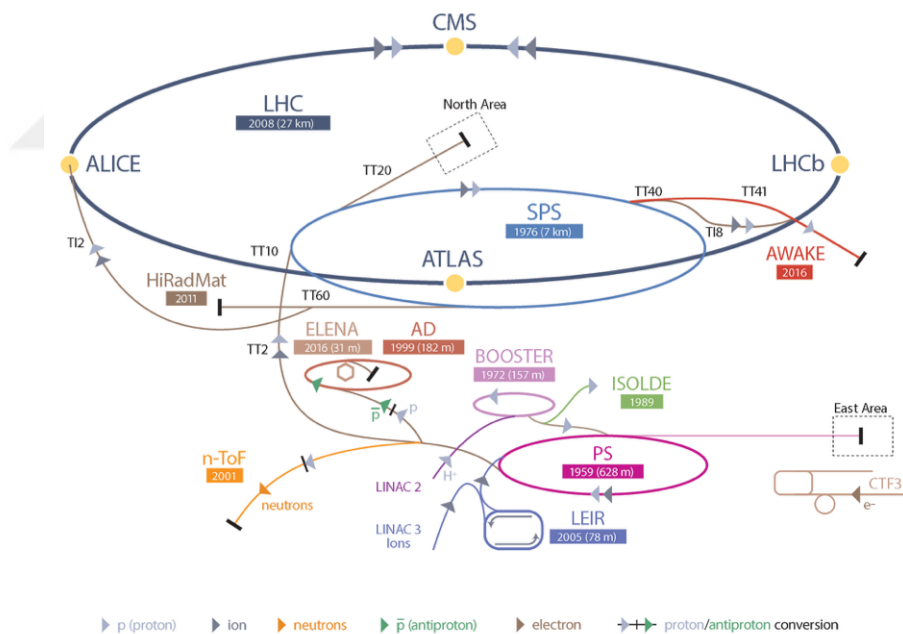


Figure 3.1: A schematic view of the LHC

Inside the accelerator, two high-energy particle beams, either protons or lead ions, travel at close to the speed of light before they are made to collide. The beams move in opposite directions in separate beam pipes. They are guided around the 27 km

Table 3.1: Summary of the LHC parameters (Vidal and Manzano, 2007)

Particle Used	Protons (P-P Collisions) Heavy Ions (Lead 82+)
Circumference [km]	27
Injected beam energy [GeV]	450
Design beam energy [TeV]	7
Actual beam energy [TeV]	6.5
Dipolar Magnetic Field [T]	8.33
Dipolar operation temperature [K]	1.9
RF Frequency [MHz]	400
Revolution Frequency [kHz]	112455
Number of Magnets	9300
Design Luminosity	$10^{34} \text{cm}^{-2} \text{s}^{-1}$
Number of bunches per protons beam	2808
Number of protons per bunches	$1.15 \cdot 10^{11}$
Bunch Spacing [ns]	25
Number of collisions per second	600 millions

accelerator ring by an 8.3 Tesla magnetic field which is 100.000 times more stronger than the Earth's magnetic field. This process carried out with superconducting electromagnets which require chilling the magnets to $-271.3 \text{ }^\circ\text{C}$, a temperature colder than that of the outer space. The electromagnets on the LHC bend and tighten the particles for keeping the beam stable and aligned. The whole accelerator complex of the LHC is illustrated in Figure 3.1 and the summary of the LHC parameters are listed in Table 3.1

The LHC is currently operating at the energy of 6.5 TeV per beam. Before the LHC reached this energy, a beam energy of 3.5 TeV (7 TeV total) was used from 2010 to 2011. In 2012, a beam energy of 4 TeV (8 TeV total) was employed. The Run1 was officially ended in 2013. In 2015, Run2 was started with the center-of-mass energy at 13 TeV which corresponds 6.5 TeV per bunch. The next step will be to reach a center of mass at 14 TeV which is the design energy. For reaching these high energies, each machine injects the beam into the next one and LHC is the last element of this chain. The story begins with the hydrogen atoms. Hydrogen atoms come from a bottle containing hydrogen. We get protons by stripping electrons from hydrogen atoms. Protons are injected into the PS

Booster (PSB) at an energy of 50 MeV from Linac2. The PS booster accelerates the beam to 1.4 GeV and sends to the Proton Synchrotron (PS). In PS, the beam is accelerated to 25 GeV and delivered to the Super Proton Synchrotron (SPS), which pushes the beam to 450 GeV. Finally, the proton beam transferred to the two beam pipes of the LHC to reach the energy of 6.5 TeV (Anonym, 2015).

In the LHC, there are mainly seven experiments. The Compact Muon Solenoid (CMS) is a general-purpose detector designed to cover the widest possible range of physics at the LHC, from precision measurements of the Higgs boson to searches for new physics Beyond the Standard Model. A Toroidal LHC ApparatuS (ATLAS) is a general-purpose detector with similar physics goals as CMS, but different technical solutions and design (Airapetian, 1999). A Large Ion Collider Experiment (ALICE) is specialized in measuring and analyzing lead-ion collisions. It especially studies the properties of quark-gluon plasma (Cortese, 2004). The Large Hadron Collider beauty (LHCb) experiment, specializes in the study of the slight asymmetry between matter and antimatter present in interactions of B-mesons containing the b quark (Anelli, 2003). The Large Hadron Collider forward (LHCf) experiment, is a small experiment that measures particles produced very close to the direction of the beams in the proton-proton and proton-nucleus collisions at the LHC (Adriani, 2006). The TOTAL Elastic and diffractive cross-section Measurement (TOTEM) experiment measures the effective size or cross-section of the proton at LHC (Kienzle, 1997). Mono-pole and Exotics Detector at the LHC (MoEDAL) is a small experiment searching for hypothetical highly ionizing particles such as magnetic mono-poles (Pinfeld, 2009). ALICE, ATLAS, CMS, and LHCb are the big experiments installed in four huge underground caverns on the LHC ring.

3.2 CMS Detector

CMS is one of the biggest particle detectors designed to see a wide range of particles that come from the high-energy collisions in the LHC. CMS is installed about 100 meters underground close to the French village of Cessy, between Lake Geneva and

the Jura mountains, a location also known in CERN as LHC Point 5. The CMS is 21 m long, 15 m high and 15 m wide, and its total weight is 14 000 tonnes. CMS detector is smaller, but heavier when compared to the ATLAS detector. CMS has similar physics goals as ATLAS. ATLAS and CMS are located on opposite sides of the LHC ring. Having two different technical designs, that they allow cross-checking of any discoveries. Figure 3.2 shows a sectional view of the CMS detector (Bayatian, 2006).

CMS has a multi-purpose physics programme ranging from studying the Standard Model to searching for extra dimensions and particles that could make up dark matter. A fundamental purpose of the CMS and ATLAS since the early 1990s has been achieved with the detection of the Standard Model Higgs boson, whose discovery was announced on 4 July 2012.

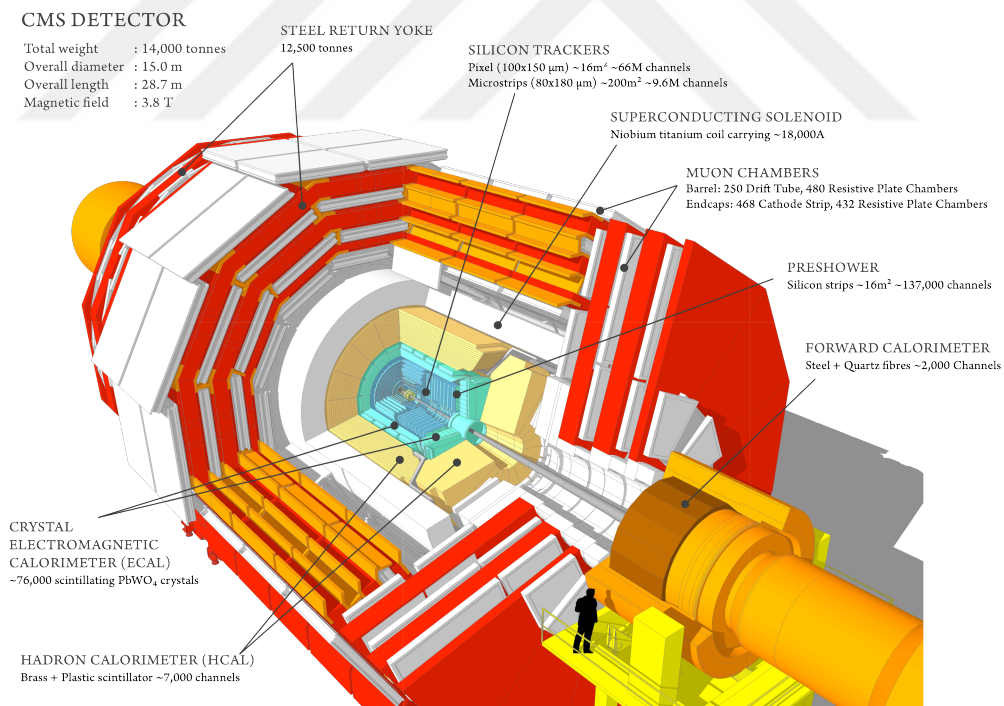


Figure 3.2: The Compact Muon Solenoid (CMS) Detector (Sakuma and McCauley, 2014).

CMS has been designed as a multilayered cylinder, resembling an onion. Each layer is responsible for catching and measuring the energy and momentum of different

Transverse Slice of the Compact Muon Solenoid (CMS) Detector

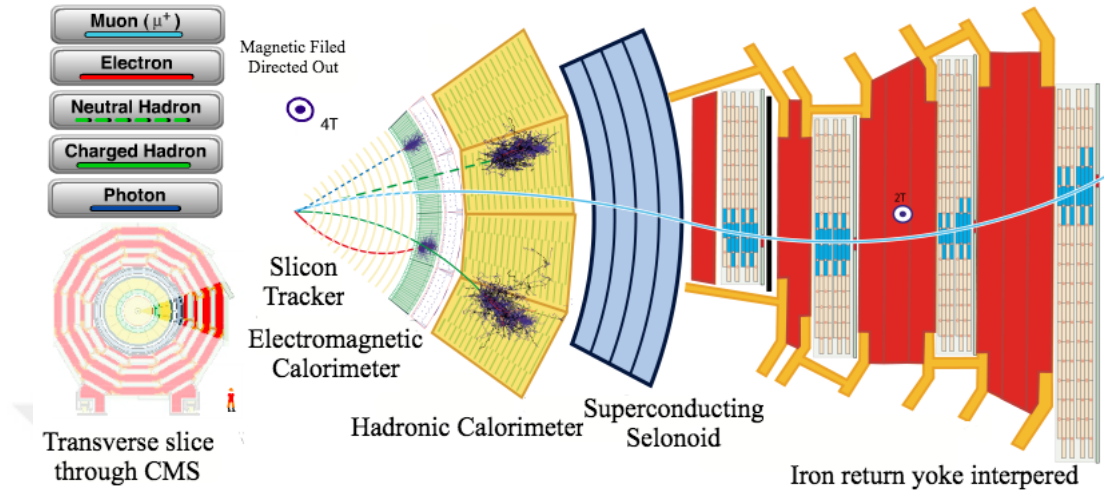


Figure 3.3: Transverse Slice of the Compact Muon Solenoid (CMS) Detector (David, 2016)

kinds of particles. The following sub-sections describe the design and construction of these layers each comprising one of the CMS sub-detector. The Figure 3.3 shows how each sub-detector detects the particles when they go through the CMS.

3.2.1 Coordinate system

A right-handed coordinate system is used at the CMS detector, with the z -axis along the counterclockwise beam direction, x -axis pointing towards the center of the LHC, and the y -axis pointing up, vertical to the LHC plane. The coordinate system of the CMS detector is illustrated in Figure 3.4. The azimuthal angle, with the ϕ , is the angle between transverse momentum (P_T), and x -axis, xy plane taken on the transverse plane. P_T is the momentum vertical to the path of the colliding particles and is equal to $P_T = P \cdot \sin \theta$. Pseudorapidity (η) is a special coordinate describing the angle of between a given particle and the beam axis (z -axis). Definition of the pseudorapidity is:

$$\eta = -\ln \tan \left(\frac{\theta}{2} \right). \quad (3.1)$$

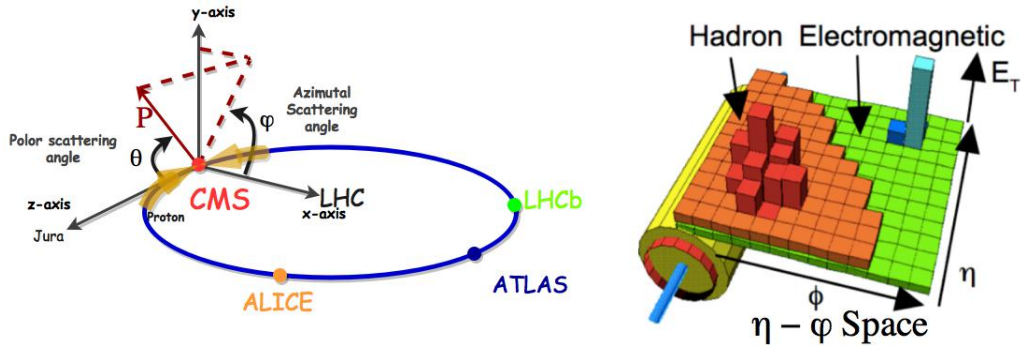


Figure 3.4: Coordinate system of CMS detector

The center of mass scattering angle (θ) is the angle between beam axis (z -axis) and two-dimensional momentum of a particle. The $\eta - \phi$ space represents a rectangular coordinate system in which η is plotted on horizontal, and ϕ is plotted on vertical. The direction of an outgoing particle is represented by a point in the $\eta - \phi$ space. The distance between any two points in the $\eta - \phi$ space is calculated using Equation 3.2.

$$d = \sqrt{(\eta_2 - \eta_1)^2 + (\phi_2 - \phi_1)^2} . \quad (3.2)$$

3.2.2 Tracker

The tracker is the innermost section of the CMS detector which surrounds the interaction point. The tracker has a length of 5.8 m and a diameter of 2.5 m. Millions of particles hit and pass through the tracker every 25 ns. The intense particle flux can cause severe radiation damage to the tracking system. The tracker detector technology requires high granularity and fast response. These requirements on granularity, speed and radiation hardness lead to a tracker design entirely based on silicon detector technology (Kramäki, 1977).

The purpose of the tracker is to provide a high precision measurement of the trajectories of charged particles up to pseudorapidities $|\eta| < 2.5$ as well as a precise reconstruction of secondary vertices. Calculating the momentum of a particle is achieved

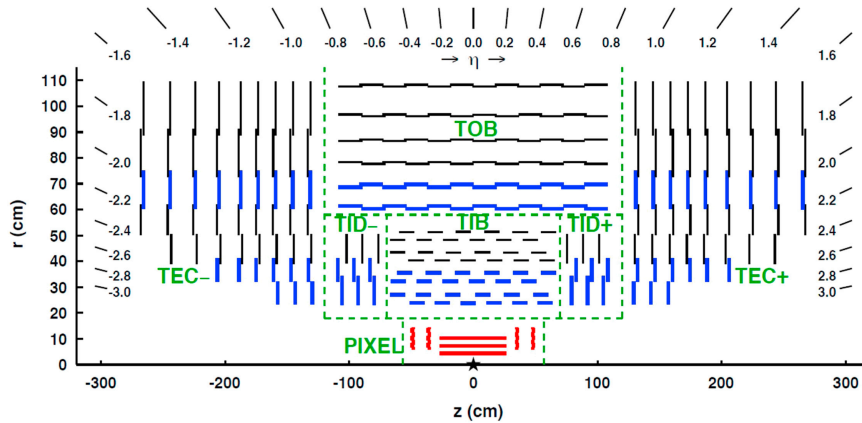


Figure 3.5: Pictorial view of the tracker slice in the r - z plane (Viliani, 2016)

by measuring the bending of its trajectory by a strong magnetic field. The tracker identifies electrons together with the electromagnetic calorimeter and also identify muons along with the muon system with high momentum resolution and efficiency. CMS tracker system consists of two subparts: pixel detector and silicon strip tracker.

Pixel detector

The high-resolution pixel detector is the innermost part of the CMS Tracker system. A small-scale pixel geometry is required for unambiguous hit recognition and precise vertex reconstruction. Short-lived particles come from the primary vertex, which can decay after having traveled only a few hundred micrometers inside the pixel detector. Therefore, the pixel detector must distinguish such secondary vertices from the original collision point. The Fig. 3.6 shows the geometrical layout of the pixel detector in η perspective and the endcaps and barrel in the pixel detector.

In total, the pixel detector covers an area of about 1m^2 and has 66 million pixels which the size of a pixel cell is $100 \times 150 \mu\text{m}^2$ and covers a pseudorapidity range $-2.5 < |\eta| < 2.5$. The pixel detector consists of 3 barrel layers which are located at a mean radius of 4.4 cm, 7.3 cm and 10.2 cm and two endcap disks which are placed on each side at $|z| = 34.5$ cm and 46.5 cm extending from 6 to 15 cm in radius.

Silicon strip tracker

The barrel tracker consists of two sections: a Tracker Inner Barrel (TIB) and a Tracker Outer Barrel (TOB). The TIB is made of 4 layers and covers up to $|z| < 65$ cm, using silicon sensors with a thickness of $320 \mu\text{m}$ and a strip pitch which varies from 80 to $120 \mu\text{m}$. The TOB comprises 6 layers with a half-length of $|z| < 110$ cm. Using silicon sensors with a thickness of $500 \mu\text{m}$. The endcaps tracker consists of two sections: a Tracker End Cap (TEC) and a Tracker Inner Disks (TID). Each TEC comprises 9 disks that extend into the region $120 \text{ cm} < |z| < 280$ cm, and each TID includes 3 small disks that fill the gap between the TIB and the TEC. The TEC and the TID modules are arranged in

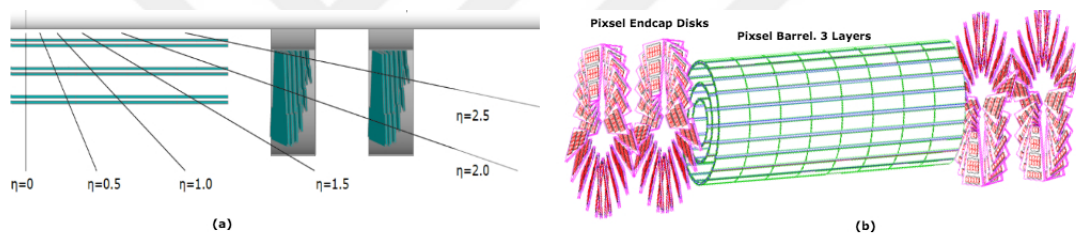


Figure 3.6: Geometrical layout of the pixel detector (Kramäki, 1977).

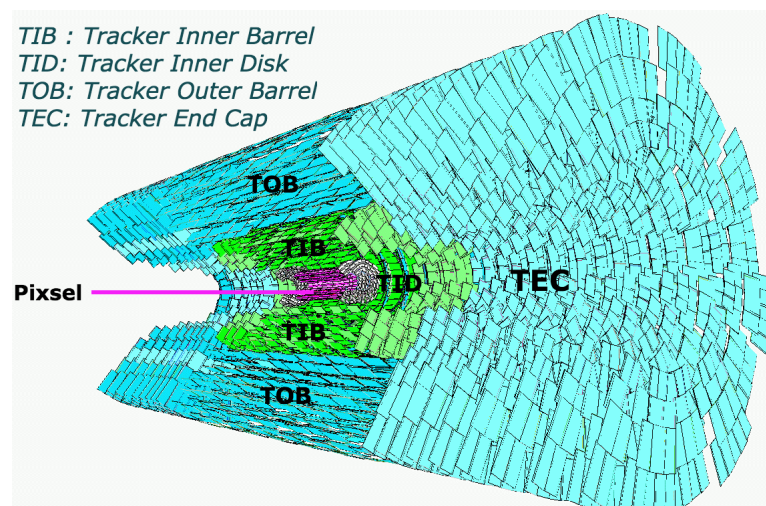


Figure 3.7: 3D view of the silicon strip tracker with description of the sub-section (Schael, 2003)

rings, centered on the beamline, and have strips that point towards the beam line, therefore having a variable pitch. Strip tracker using the single-sided p - n -type silicon microstrip sensors. Silicon strip detectors located on the way of the tracker after the pixel detector. The particles pass through 10 layers of silicon strip detectors, reaching out to a radius of 130 cm. The silicon detectors work in much the same way as the pixel. Figure 3.7 shows the 3D view of the silicon strip tracker with its sub-detectors.

3.2.3 The Electromagnetic Calorimeter (ECAL)

Electromagnetic Calorimeter (ECAL) of CMS is placed between the inner tracker and the Hadronic Calorimeter (HCAL). The space and material between ECAL and HCAL are minimized to ensure the best possible jet and missing transverse energy measurements. Also, the inner tracker system optimized the interface in front of the ECAL. The geometrical crystals and the photodetectors of the ECAL coverage extend to $|\eta| = 3$ and consists of three sections, where are the barrel (EB), the endcaps (EE), and the preshower (ES). Figure 3.8 illustrates the longitudinal view of one-quarter of the ECAL (Hofer, 1997).

The Electromagnetic Calorimeters measure the energy of electrons and photons interacting electromagnetically. They also help in particle identification, specifically electron, charged-pion separation in conjunction with the tracker, Finally, the ECAL helps to measure the energy of high energy hadrons in conjunction with the HCAL. In particular, the ECAL played an essential role in the study of the electroweak symmetry breaking, mainly through the search of the low mass Higgs boson at the LHC in the decay channel $H \rightarrow \gamma\gamma$. ECAL also provides a information for a variety of SM process and other new physics processes. ECAL gives a reconstruction of a background-free $Z \rightarrow ee$ data sample by measuring the electrons from the decay Z_s , originating from $H \rightarrow ZZ^*$. It is also crucial for other measurements such as cascade decays of gluinos and squarks, where the lepton pair mass provides information about the supersymmetric particle spectrum or the leptonic decay of new heavy vector bosons in the multi TeV mass range.

Consequently, one of the principal CMS design objectives is to construct a very high-performance electromagnetic calorimeter. For this, Lead Tungstate crystals (PbWO_4) were chosen as the active material of choice in the ECAL for operation at the LHC because they offer the best prospects of reaching the demanding requirements. PbWO_4 has a high density (8.3g/cm^3), short radiation length (0.89 cm), and a small Molière radius (2.2 cm), resulting in a high granularity and allowing for the construction of a compact calorimeter inside the magnet. This high granularity is needed for the π^0 - γ separation and angular resolution. These crystals also ensure fast light emission, with the scintillating decay time of the same order of magnitude as the LHC bunch crossing time.

The Energy resolution of ECAL between 25 GeV and 500 GeV can be parametrized as:

$$\left(\frac{\sigma_E}{E}\right)^2 = \left(\frac{S}{\sqrt{E}}\right)^2 + \left(\frac{N}{E}\right)^2 + C^2, \quad (3.3)$$

where E is the energy, usually in GeV, σ_E/E is the energy resolution, S is the stochastic

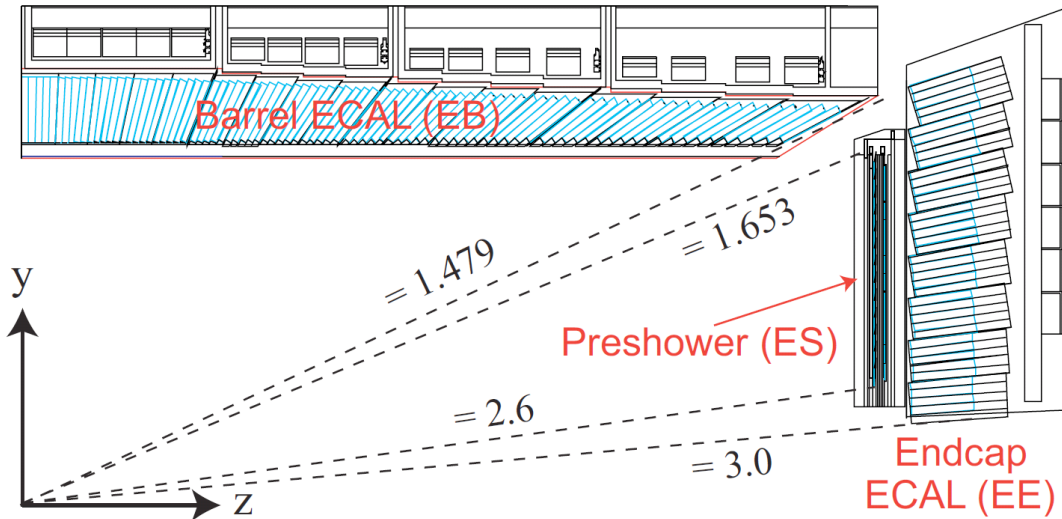


Figure 3.8: Longitudinal view of one quarter of the ECAL with the barrel (EB), the endcaps (EE), and the preshower (ES) (Isildak, 2011)

term which is mainly governed by photostatistics and sampling fluctuations. N is the noise term which comes from electronic noise, digitization noise, and pile-up. C is the constant term which mainly from shower containment limitations and calorimeter non-uniformities. Each term should be small and in the same order at the relevant electron/photon energies for optimum calorimeter performance.

Barrel calorimeter

There are 36 identical supermodules, 18 in each half barrel, each covering 20° in ϕ and pseudorapidity range $0 < |\eta| < 1.479$. Each supermodule contains four modules. The first module consist of 500 crystals and rest of three modules consist of 400 crystals corresponding to the total number of 61200 crystals. The crystal cross-section corresponds to approximately 0.0175×0.0175 in the $\eta - \phi$ or $22 \times 22 \text{ mm}^2$ at the front of the crystal, with radius 1.29 m and the length of 230 mm corresponding to $25.8 X_0$.

Endcaps calorimeter

The endcaps cover the pseudorapidity range of $1.48 < |\eta| < 3.0$. Pileup effects and radiation damage limits the performance of the calorimeter at very high η so, the precision energy measurement comes from $\eta < 2.6$. In order to increase the energy-flow measurement in the forward direction, the crystals are installed up to $\eta = 3.0$. They are made of crystals with a length of $24.7 X_0$. The mechanical design of the endcap calorimeter is based on an off-pointing pseudo-projective geometry using tapered crystals of the same shape and dimensions ($24.7 \times 24.7 \times 220 \text{ mm}^3$) grouped into units of 36, referred to as supercrystals. A total of 268 identical supercrystals is used to cover each endcap with a further 64 sectioned supercrystals used to complete the inner and outer perimeter. Each endcap contains 14648 crystals, corresponding to a volume of 1.52 m^3 .

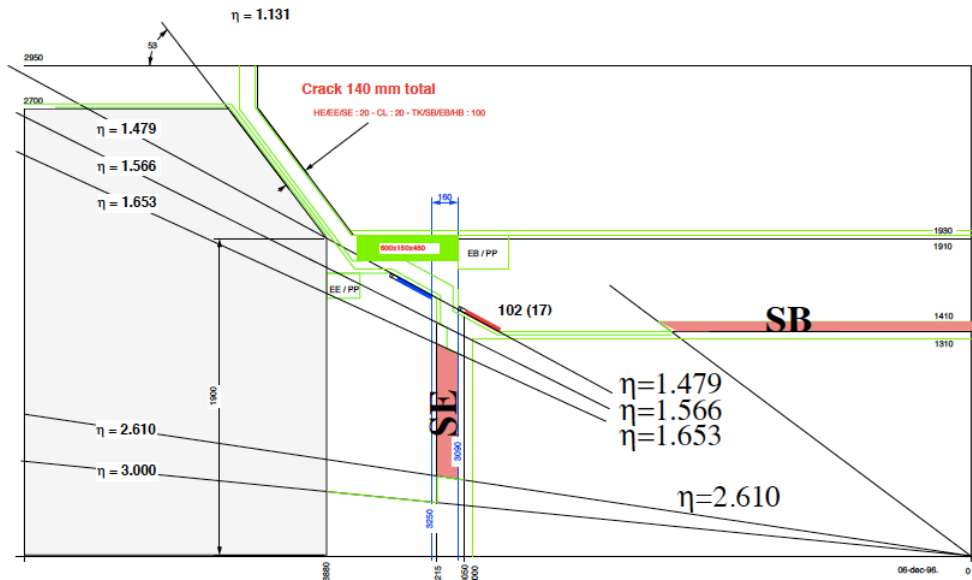


Figure 3.9: Approximate positions of the endcap and barrel preshowerers in CMS (Hofer, 1997).

Preshower

There are two preshower detectors: one is in front of the ECAL barrel calorimeter and covers the pseudorapidity range up to $|\eta| = 0.9$ and the other one is in front of the ECAL endcaps and covers the pseudorapidity range $1.65 < |\eta| < 2.61$. They are similar in design but have very different functions. Figure 3.9 shows the positions of the endcap and barrel preshowerers in CMS. The barrel preshower (SB) is used to measure the angle of incidence of photons which is helping the accuracy of the measurement of the angle between the two photons. This angle requires a knowledge of the decay point of the $H \rightarrow \gamma \gamma$. The Endcap Preshower (SE) distinguishing energy deposits in the ECAL caused by single photons and photons from the decay of neutral pions (π^0). The neutral pions in jets are background to the $H \rightarrow \gamma \gamma$ channel with this π^0 rejection on the endcap preshower helping the separation between the two photons from the decay of a π^0 .

3.2.4 The Hadronic Calorimeter (HCAL)

The Hadronic Calorimeter (HCAL) surrounds ECAL, and they form a complete CMS calorimetry system. This calorimetry system measures the energy and direction of particle jets and the missing transverse energy to the measurement of quark, gluon and neutrino directions, and energies. The determination of missing energy also forms a crucial signature for new particles and phenomena, such as encounters in the searches for the supersymmetric partners of quarks and gluons. The HCAL determines the electrons, photons, and muons together with the ECAL and the muon system.

The design of the HCAL requires good hermiticity, good transverse granularity, moderate energy resolution and sufficient depth for hadron shower containment. The HCAL granularity of $\delta\eta \times \delta\phi = 0.087$ for $\eta < 2.0$ to match the electromagnetic calorimeter and the muon chamber structure. This granularity is sufficient for good dijet separation and mass resolution. The physics program most demanding of good hadronic resolution and segmentation is the detection of narrow states decaying into a pair of jets. The dijet mass resolution receives contributions from physics effects such as

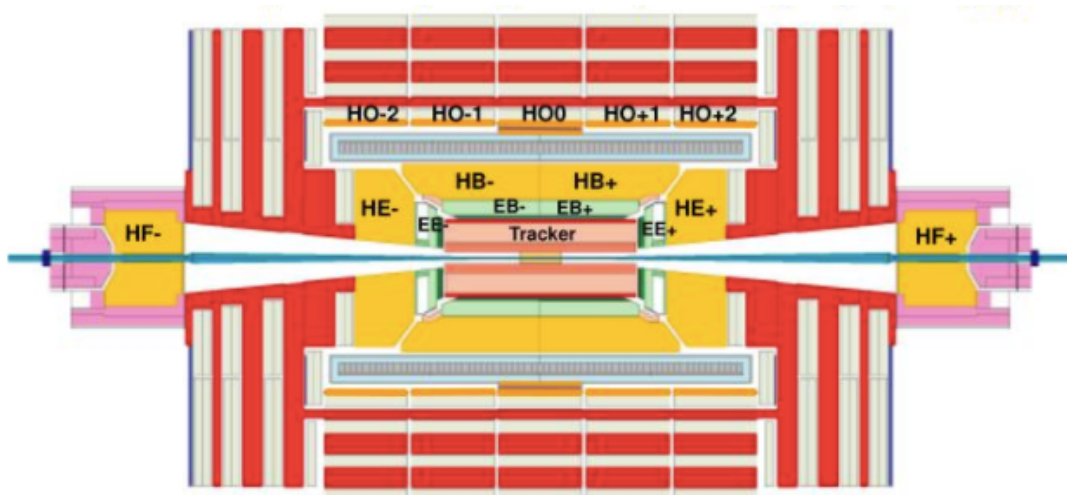


Figure 3.10: The Hadron Calorimeter with Hadron Barrel (HB), Hadron Endcap (HE), and Hadron Outer (HO) in the central part of CMS. The Hadron Forward (HF) is physically separated from the central calorimeter (Green, 1997).

fragmentation and initial and final state radiation, as well as detector effects such as angular and energy resolution.

The HCAL can be considered in two pieces: one of them is a central calorimeter which comprises $\eta < 3.0$. The central calorimeter consists of three parts: the Hadron Endcap (HE), the Hadron Barrel (HB), and the Hadron Outer (HO). The HE and the HB are located inside the CMS magnet, but the HO is located outside of the magnet. The HO is required in the barrel and endcap region to measure late shower development and ensures of total shower energy containment. The central part of HCAL provides excellent jet identification, moderate single particle, and jet resolution. The other part of HCAL is a forward calorimeter which comprises $3.0 < \eta < 5.0$ with modest hadron energy resolution but with good jet identification capability. The Hadron Forward (HF) calorimeter is physically separated from the central calorimeter, its front face is being located at $\pm 11\text{m}$ from the interaction point. Figure 3.10 illustrates the HCAL calorimeter with all sub-detectors (Green, 1997).

Hadron Barrel (HB)

The HB is placed inside the magnetic coil and covers the pseudorapidity range $|\eta| < 1.3$. The HB extends radially between $r = 1.806$ and $r = 2.95$ meters, with 2304 towers, resulting in a segmentation of $\delta\eta \times \delta\phi = 0.087 \times 0.087$. Each tower is made up of alternating layers of the non-magnetic brass absorber and plastic scintillator material to eliminate magnetic forces on it. The HB is divided into two half-barrel sections. The half-barrel at positive z -axis is labeled HB+, while the negative z -axis barrel is labeled HB-. Each half-barrel consists of 18 identical azimuthal wedges. These wedges are numbered 1 through 18 for in the each half-barrel, starting with 1 at the x -axis and proceeding counterclockwise towards positive y -axis. Each wedge subtends 20 degrees of ϕ , and extends from the CMS detector mid-plane about 4.3 meters in z and weighs 25.7 metric tonnes.

Hadron Endcap (HE)

The two hadron endcaps cover a region of $1.3 < |\eta| < 3.0$. The granularity begins from $\delta\eta \times \delta\phi = 0.087 \times 0.087$ at $|\eta| < 1.6$ up to $\delta\eta \times \delta\phi = 0.17 \times 0.17$ at $1.6 < |\eta| < 3.0$. The total depth of the HE calorimeter is about 10 absorption lengths (19 active layers). The absorber sampling thickness is 8 cm. The absorber material is brass (90% Cu + 10% Zn), the front and back plates are made of stainless steel to increase strength. The absorber plates are bolted together to form a single monolithic structure, with gaps for scintillator insertion. This structure is conceptually similar to the barrel structure, although differing in engineering details because of the endcap geometry and mounting scheme. The photodetector is the Hybrid Photodiode (HPD) used for the HE and the HB. The wavelength-shifting fibers transport the scintillation light from the HB and the HE tiles to HPDs, whose electric signals are then integrated and digitized by the Charge Integration and Encoder version 8 (QIE8) before being sent to off-detector readout electronics.

Hadron Outer (HO)

The HO calorimeter is located outside the solenoid as an extension the HB due to the space inside the solenoid is not sufficient to contain the hadronic showers completely. Without the outer barrel, particles showering late in the calorimeter would not deposit their energy in the HCAL, resulting in a considerable contribution to the missing transverse energy, a result that would be inconvenient for many physics analysis purposes. The granularity and η range of outer barrel are the same as the hadron barrel. The HO is located in all 5 barrel rings of CMS and is split into 30 sections along the z -axis (beam-line). In the transverse plane, the HO consists of 12 sectors, each with 6 trays, totaling 72 sections, each 5° . The scintillation light is collected with wavelength shifting fibers and transmitted over clear fibers to front-end electronics placed close to the layers. Each $\eta - \phi$ position is read out by a separate channel, summing to 2160 physical channels. A schematic layout of the calorimeters in CMS and the location of the HO scintillators is shown in Figure 3.11.

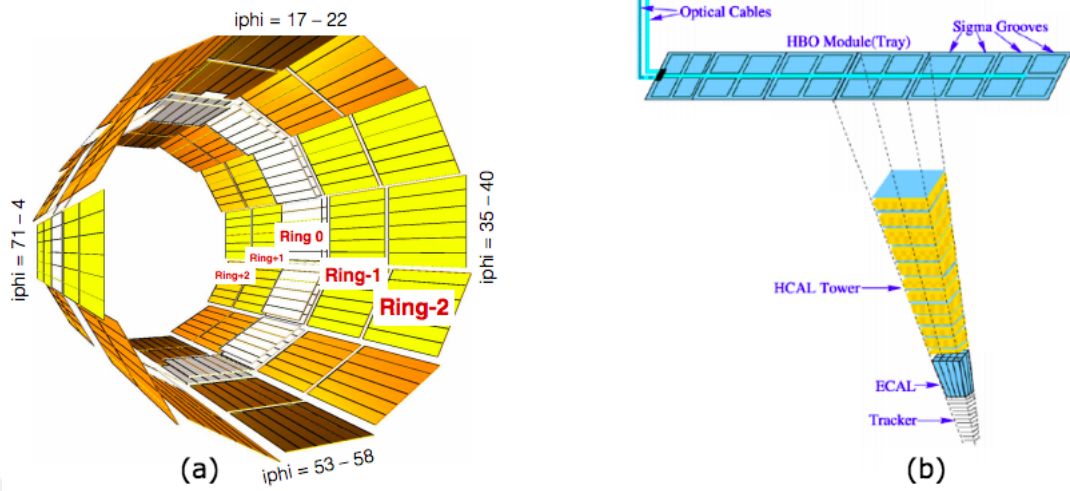


Figure 3.11: (a) The HO layout (b) HO tiles corresponding to HB towers (Lobanov, 2015)

Hadron Forward (HF)

The very forward calorimeter (HF) covers the pseudorapidity range $3.0 < |\eta| < 5.0$. The front face of HF is located at ± 11.1 m from the interaction point (IP). The main targets of this detector are to improve the measurement of the missing transverse energy (E_T^{miss}), to enable identification and reconstruction of very forward jets, and luminosity calculation. In some cases, these jets are the distinguishing characteristic of several essential physics processes, in others, they are background signatures. Each HF module (HF+, HF-) is consist of 18 wedges in a nonprojective geometry with the quartz fibers running parallel to the beam axis along the length of the iron absorbers. The quartz fibers have two different lengths to differentiate between shower processes. Longer fibers length of 1.65 m, which provide light from EM and hadronic showers in the absorber. Shorter fibers length of 1.43 m that contain the hadronic showers.

3.2.5 The Magnet

The magnet of the CMS detector is a superconducting solenoid designed to reach 4 Tesla uniform magnetic field, which aims to maximize the physics performance of CMS. The job of a solenoid magnet is to bend the paths of particles emerging from high energy collisions to reach accurate measurement of the momentum. The more momentum a particle has, the less its path is curved by a magnetic field, so the measurement of momentum comes from a trace of its path (Herve, 1997).

The superconducting solenoid is the largest superconducting magnet ever built with 6 m diameter and 12.5 m length, and the total weight is 12,000 tonnes. It can be cooled to -268.5°C which is colder than outer space and its magnetic field is 100,000 times stronger than the Earth's magnetic field.

3.2.6 The Muon system

The muon system is the outermost of the CMS subdetectors. One CMS major design goal is to reconstruct the momentum and charge of muons over the entire kinematic range of the LHC. The muon system has three main purposes: muon identification, muon trigger, and muon momentum measurement. It is placed outside the magnet coil and covers pseudorapidity range $0 < |\eta| < 2.4$. The muon system uses three different technologies to detect and measure the muons; drift tubes (DT) in the barrel region which roughly covers pseudorapidity $|\eta| < 1.2$, cathode strip chambers (CSC) in the endcap region which covers pseudorapidity range $0.9 < |\eta| < 2.4$, and resistive plate chambers (RPC) in both the barrel and endcap which covers pseudorapidity $|\eta| < 1.6$. Figure 3.12 shows a quadrant view of the R - z cross-section of the CMS detector, blue line points out the RPC chambers, yellow in barrel shows the DT and green in endcap shows the CSC. The steel of the return yoke is shown in gray (Gasparini, 1997).

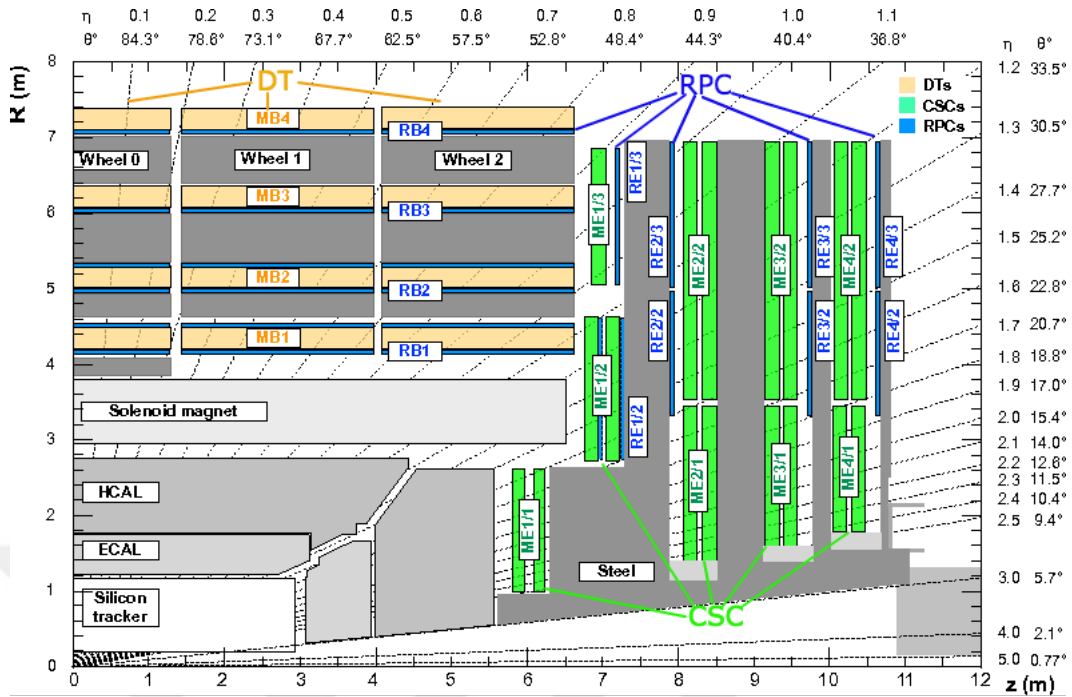


Figure 3.12: A quadrant of the R - z cross-section of the CMS detector, The RPC chambers are marked in blue line and they are coupled with DTs (yellow) in the barrel, and CSCs (green) in the endcaps. The steel of the return yoke is shown in gray (Giovanni, 2015).

Major upgrades of the muon detectors have been implemented in 2013-2014 during the Long Shutdown 1 (LS1). ME4/2 is one of the outermost rings of CSC in the fourth station and RE4/2, and RE4/3 are outermost rings of RPC in the fourth station have been completed during the LS1 (Giovanni, 2015).

Drift Tube (DT)

In the barrel region, where the neutron-induced background is small, the muon rate is low, the 4T magnetic field is uniform and mostly bounded by in the steel yoke, drift chambers with standard rectangular drift cells are used. The barrel DT chambers cover the pseudorapidity region of $|\eta| < 1.2$ organized into four sections and installed into the yoke barrel (YB). These positions are called MB1, MB2, MB3, and MB4 located at a radius of approximately 4.0, 4.9, 5.9 and 7.0 m from the beam axis. The barrel DT consists of 5 wheels and each of them divided into 12 sectors with each covering a 30°

azimuthal angle. In the sections MB1 and MB2, each package consists of one DT chamber sandwiched between two RPCs. In sections MB3 and MB4, each package consists of one DT chamber and one RPC. Figure 3.13 shows the layout of the CMS barrel muon DT chambers in one of the five wheels.

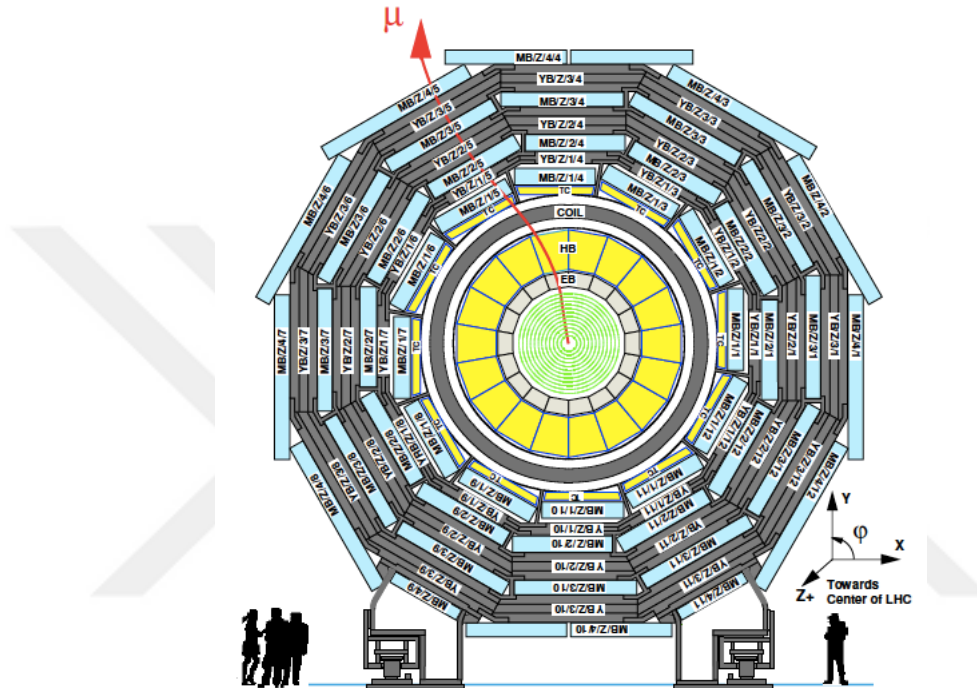


Figure 3.13: Layout of the CMS barrel muon DT chambers in one of the 5 wheels(Chatrchyan, 2010)

Cathode Strip Chamber (CSC)

In the two endcap regions of CMS, where the muon rates and background levels are high and the magnetic field is large and non-uniform, the muon system uses cathode strip chambers (CSC). The CSC has a fast response time, fine segmentation, and radiation resistance, which help to identify muons between $0.9 < |\eta| < 2.4$. There are 4 stations (ME1, ME2, ME3, ME4) of CSCs in each endcap. The ME1 station is divided into 3 rings of chambers (ME1/1, ME1/2, ME1/3) and there are 72 cathode strip chambers for each of them. The other stations are divided into 2 rings of a chamber. The first ring of chambers for each station has 36 and the second one has 72 cathode strip chambers. These

chambers have a trapezoidal shape and arranged in a series of concentric rings centered on the beam-line. The stations are separated by the iron disks of the flux return yoke, which is thick enough to isolate the electrons in showers.

Resistive plate chamber system (RPC)

The RPC has two parallel plates which they are made out of phenolic resin separated by a gas gap of a few millimeters. In the barrel region, a total of six layers of RPCs are embedded in the iron yoke, two of them are placed in each of the muon stations MB1 and MB2. The other two in each of the stations MB3 and MB4. The redundancy in the first two sections allows the trigger algorithm to perform the reconstruction always by four layers, even for low P_T tracks, which may be stopped inside the detector. In the endcap region, four stations of RPCs are placed in the forward part of CMS (ME1, ME2, ME3, ME4) to cover the region up to $\eta = 2.1$. The stations have a trapezoidal shape, and the strips run along the radial direction. In order to maintain projectivity, the strip shape is trapezoidal, so that in each h region its width always covers $5/16$ degrees in ϕ . Also, the strip length varies, according to the h region, from ~ 25 cm to ~ 100 cm. The endcap RPC stations are built using the double-gap concept.

3.2.7 Data Acquisition (DAQ) and trigger

The LHC is designed to collide protons at a center-of-mass energy of 14 TeV and the design luminosity of $10^{34} \text{cm}^{-2} \text{s}^{-1}$. At this design luminosity, the pp interaction rate exceeds 1 GHz, which is practically impossible to store this amount of data. In addition, saving all events would not be useful due to most of the elastic collisions which are not interesting for CMS physics program. The trigger system selects the exciting events in real time and stores them. CMS Trigger system makes this selection in two-part: a Level-1 Trigger (L1) and High-Level Trigger (HLT).

The first level (L1) of the CMS trigger is implemented in specific hardware. L1 process an event that should be accepted or rejected using the simple logical operations

directly on detector signals and reduce the rate to the 100 kHz. The second step is HLT system based on the software system. It takes decisions analyzing the reconstructed quantities for a given object and reduces the rate of stored events by a factor 1000 bringing the frequency to about 1 kHz.

The Level-1 trigger

The L1 trigger gets a new event from the detector every 2 ns. At the first level, all information about the event is conserved, and L1 decides whether to keep or discard the data. The L1 trigger system is organized into two major subsystems: the L1 calorimeter trigger and the L1 muon trigger. All information from these two parts are sent to the Global Trigger, which takes the final accept-reject decision (Acosta, 2006).

The L1 calorimeter trigger begins with trigger tower energy sums formed by the ECAL, the HCAL, and the HF upper-level readout. Trigger Primitive Generator (TPG) transforms the individual calorimeter cell energies. The TPG information is transmitted over high-speed copper links to the Regional Calorimeter Trigger (RCT), which finds candidate electrons, photons, taus, and jets. The RCT individually finds both isolated and non-isolated electron/photon candidates. The RCT transmits the candidates along with sums of transverse energy to the Global Calorimeter Trigger (GCT). The GCT organizes the candidate electrons, photons, taus, and jets and forwards the top 4 of each type to the global trigger. The GCT also calculates the total transverse energy and total missing energy. It forwards this information to the global trigger as well.

The muon trigger is organized into CMS trigger subsystems stands for the 3 different muon detector systems, CSC trigger in the endcap, DT Trigger in the barrel, and RPC trigger are covering both barrel and endcap. Each of the L1 muon trigger systems has its trigger logic. The trigger tracks from RPC are built by the pattern comparator trigger (PACT) using information coming from the detector hits directly. The local trigger track primitives are formed within the DT and the CSC detectors prior to the transmission to the respective track finders. The Global Muon Trigger sorts the

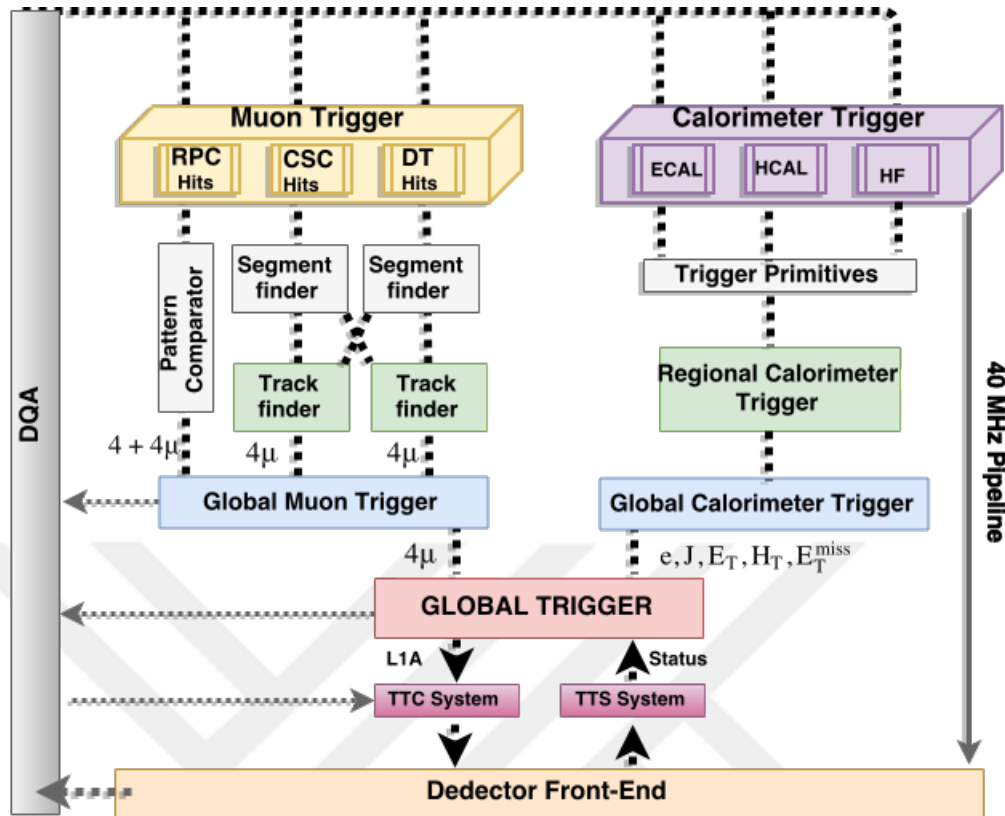


Figure 3.14: The Level-1 trigger layout for calorimeter and muon sub-detectors.

muon tracks coming from the RPC, the DT, and the CSC. These tracks are converted into the same η , ϕ and p_T scale, and validates the muon sign. The final community of muons are sorted based on their initial quality, correlation and p_T and then the 4 top muons are sent to the Global Trigger. Figure 3.14 shows the L1 trigger layout for calorimeter and muon sub-detectors.

The L1 Global Trigger makes final decisions to reject or accept a physics event for subsequent evaluation by the HLT. This decision is based on trigger objects from the L1 muon and the calorimeter systems, which contain information about transverse energy E_T or transverse momentum P_T , location (pseudorapidity and azimuthal angle), and quality.

The High Level Trigger (HLT)

HLT is designed to reduce the maximum L1 accept rate of 100 kHz to the final output rate of 100 Hz. The performance of the CMS DAQ/HLT system follows the step listed below:

- perform the readout of the front-end electronics after a L1 trigger accept;
- execute physics selection algorithms on the events read out, in order to accept the ones with the most interesting physics content;
- forward these accepted events, as well as a small sample of the rejected events, to the online services which show the performance of the CMS detector (Cittalin, 2002).

3.2.8 CMS computing model

One of the most significant challenges in CMS managing and storing the massive amount of data and provide necessary computing resources. For this, CMS uses the Grid services which set of services provide the computing, storage and connectivity resources. CMS uses tge Grid to conduct data processing, data archiving, Monte Carlo event generation, and all kinds of computing-related activities utilizing the computing centers. These computing centers available to CMS around the world are distributed and configured in a tiered architecture that process as a single coherent system. Each of the three-tier levels provides different resources and services:

The first tier in the CMS model, for which there is only one site, CERN, is known as Tier-0 (T0). T0 accepts RAW data from the CMS Online Data Acquisition and Trigger System (TriDAS) during CMS data taking. The RAW data which received from the DAQ repacks into primary datasets based on trigger information. Tier-0 also archives the repacked RAW data into the tape and distributes RAW data sets to the Tier-1. In order to keep two copies of every piece of RAW data, one is saved at CERN, another at a

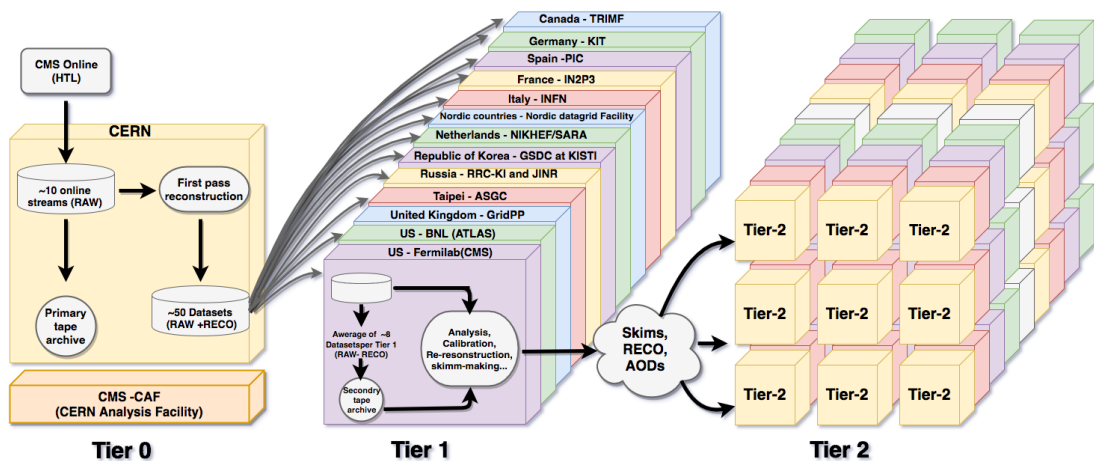


Figure 3.15: The data flow of CMS detector through the tiers.

Tier-1 site. The RAW datasets are reconstructed into the RECO. The RECO datasets are distributed to the Tier-1 centers.

Tier-1 consists of 13 computer centers, which are large centers in CMS collaborating countries. Tier-1 sites usually use for large-scale, centrally organized activities and can provide data to and receive data from all Tier-2 sites. Each T1 center offers tape archive of part of the RAW data. Tier-1 centers have significant CPU power for scheduled: re-reconstruction, skimming, calibration, AOD extraction, and stores an entire copy of the AOD. Tier-1 also distributes RECOs, skims and AOD to the other T1 centers and CERN as well as the associated group of T2 centers, provides secure storage and redistribution for MC events generated by the Tier-2's.

There is a larger set of smaller Tier-2 ("small" centers at universities), but with significant CPU resources, providing the capacity for user analysis, calibration studies, and Monte Carlo production. T2 centers offer limited disk space and no tape archiving. The T2 sites provide services for local communities grid-based analysis for the whole experiment (T2 resources available for the entire experiment through the grid), and Monte Carlo simulation for the whole experiment. Figure 3.15 shows the data flow of the CMS detector through the tiers.

CMS Data is organized into a hierarchy of data tiers. Each physics event is written into each data tier, where the tiers each consist of different levels of information about the event. The four main data types written in CMS are RAW, RECO, AOD and, MiniAOD. The RAW data contain full event information from the detector, and they are often not utilized directly for analysis. The reconstructed data (RECO) contains reconstructed physics objects, they can use for analysis, but still, provide very detailed data and hard the process. The Analysis Object Data (AOD) is a distilled version of the RECO event information and is expected to be used for most of the physics analyses. MiniAOD is condensed dataset of AOD which uses the minimum amount of space, extract only the minimum required data from existing data formats, and re-use existing data excluding unnecessary data (Sphicas, 2005).

4. JET RECONSTRUCTION AND CALIBRATION AT CMS

A jet is a spray of particles that come from the hadronization and fragmentation of high momentum of colored particles (quark, gluon) which can not be free because of color confinement. Therefore we can see colored particle as an experimental signature of the hadron-hadron collisions. Jets are used to understand the strong interaction and also to search for new strongly-interacting physics.

Jets can be made out of leptons, hadrons and even bosons, particularly the photon, and these particles cluster in a cone with different jet algorithms uses to define a jet cone. A jet can be defined using 4-momentum information which is calculated using the transverse momentum (P_T), the azimuthal angle (ϕ), the rapidity $y = \frac{1}{2} \log \frac{E+P_z}{E-P_z}$, and invariant mass of jet M . The four-momentum of jet can be written as (Hauth,1990):

$$\begin{aligned} p^\mu &= (E, P_x, P_y, P_z) \\ &= (\sqrt{P_T^2 + m^2} \cosh(y), P_T \cdot \sin \phi, P_T \cos \phi, \sqrt{P_T^2 + m^2} \sinh(y)) \end{aligned} \tag{4.1}$$

4.1 The Particle Flow Jets

The Particle Flow (PF) is a full event reconstruction technique where purpose is to reconstruct all stable particles arising from the hadron-hadron collision. The PF algorithm first gathers reconstructed hits in each sub-detector independently and create a list of reconstructed elements. These elements are linked topologically into blocks, and PF jets are reconstructed from these blocks (Bernet,2009).

PF can find and classify electrons, muons, photons and charged and neutral hadrons from the events, depending on the type of blocks involved in the reconstruction. Photons are reconstructed from energy deposits in the ECAL. Electrons are clustered from a combination of a charged track and energy deposits in the ECAL. Muons are

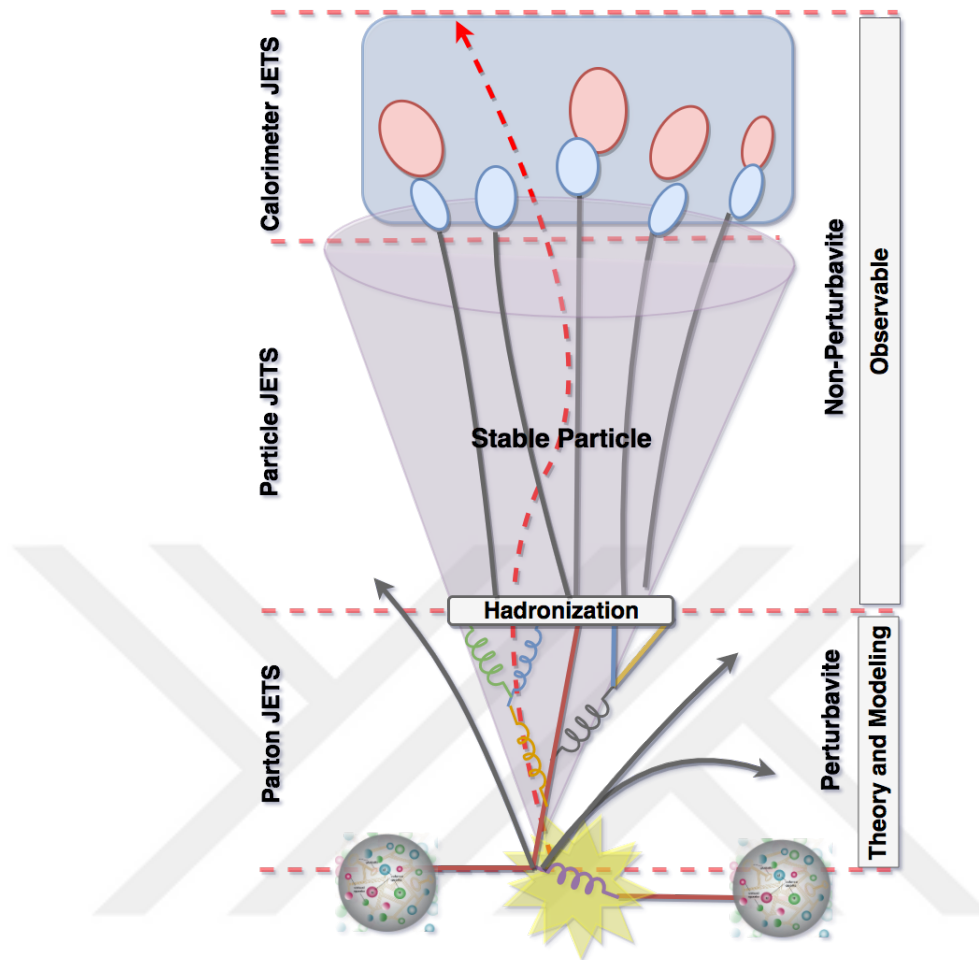


Figure 4.1: The Jet evolution at hadron-hadron collision.

reconstructed from a combination of tracker and muon chamber information. The charged particle tracks that match with deposits in both HCAL and ECAL are identified as charged hadron candidates. The neutral hadron information comes only from the HCAL.

In this search, PF jets are used to collect the information from all sub-detectors. The traditional way of simply clustering calorimeter deposits to form jets suffer from large fluctuations and nonuniformity. So, with Particle Flow, reconstruction of the jet momentum and position is improved over that of calorimeter jets because of the additional information provided by the tracker and the high granularity ECAL.

4.2 Jet Reconstruction Algorithms at CMS

As we discussed in the previous section, PF candidates are clustered with information that come from each sub-detector. These PF candidates should be re-clustered as a jet object in the detector through the implementation of the clustering algorithm. Actually, a jet is a messy collection of particles flying through in the same direction and it is hard to define which particles come from hard parton interaction. So, we need a “jet” definition that clearly specifies which particle belongs to a jet and how many jets originated in hadron-hadron collisions. If the jets are defined in a similar way, the results can be compared amongst different experiments and with the theory as well. As a result, we can make a list of requirement that we expect jet clustering algorithms to satisfy a follows:

- Simple to implement in an experimental analysis;
- Simple to implement in theoretical calculations;
- Defined at any order of perturbation theory;
- Yields finite cross section at any order of perturbation theory;
- Yields a cross section that is relatively insensitive to hadronization;

There are also two fundamental physical requirement that any jet reconstruction algorithms should obey: Infrared and collinear (IRC) safety. Infrared safety means that adding a soft gluon should not change the results of jet clustering. Collinear safety is that splinting one parton into two parton (e.g., a gluon splitting in two quarks) should not change the jet clustering. Figure 4.2 shows an example of Infrared and collinear safety.

There are two kinds of mainstream clustering algorithms: cone-type and sequential clustering. Midpoint clustering algorithm, iterative cone clustering algorithm, and seedless infrared-safe cone clustering algorithm (SIScone) are classified as cone-type clustering algorithms. The second class is the sequential clustering algorithms,

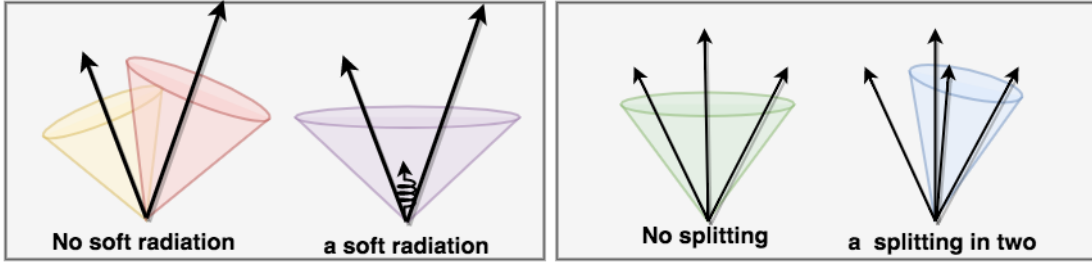


Figure 4.2: Illustration of the infrared sensitivity of a cursory designed jet algorithm: the emission of a soft gluon changes the number of jets (left). Illustration of the product of a collinear unsafe jet algorithm: the collinear splitting changes the direction of the jet (right)

which include the k_T (Catani 1993), anti- k_T (Caciari, 2008) and the Cambridge/Aachen algorithms (Bentvelsen and Meyer, 1998).

Cone algorithms clustered the particle based on $\eta - \phi$ space, in a conical region to form a jet, that turns out resulting in jets with rigid circular boundaries. Cone algorithms in the past were preferred by experimentalists as they were easier to apply to the experimental analysis. However, they are not favored by theorists as they contain non-physical constants. Also, cone algorithms are generally IRC unsafe.

Sequential clustering algorithms assume that particles within jets will have small differences in transverse momenta and thus groups particles based on momentum space. Theorists have always favored sequential clustering algorithms, but not by experimentalists as in the past due to the restricted computational performance. After the introduction of the FastJet program (Caciari, Salam and Soyez, 2011), which allows much faster reconstruction, sequential clustering algorithm preferred by experimentalists as well. Also, the sequential clustering algorithms are IRC safe.

The CMS experiment mainly used three type of clustering algorithms which are iterative cone algorithm, seedless infrared-safe cone (Salam and Soyez, 2007), and anti- k_T sequential clustering algorithm. The first two belong the cone-jet algorithm, and the Cone jet algorithms are motivated by the idea of defining a jet as an angular cone around some direction of dominant energy flow. To find these directions of dominant energy flow, cone

algorithms usually take some of the event particles as ‘seeds’, i.e., trial cone directions. Then for each seed, they establish the list of particles in the trial cone, calculate the sum of their 4-momenta, and use the resulting 4-momentum as a new trial direction for the cone. This procedure is repeated until the cone direction no longer changes, and labeled as a “stable cone”. The third one is the anti- k_T algorithm, which is an example of sequential clustering algorithm. The anti- k_T algorithm is an infrared and collinear safe algorithm, thus making it more favorable in CMS. In this search, we also use the anti- k_T algorithm to cluster the jets. We will broadly discuss the anti- k_T algorithm in the following section.

4.2.1 The Anti- k_T Algorithm

The first distance parameter d_{ij} between two particles is given by (Atkin,2015);

$$d_{ij} = \min(p_{Ti}^a, p_{Tj}^a) \times \frac{P_{ij}^2}{R} \quad (4.2)$$

where a is a parameter that varies depending on the choice of a particular clustering algorithm, which in anti- k_T algorithm corresponds to the value of -2 resulting cluster hard particles first due to $a = -2$ dominate the equation 4.2 by the highest P_T .

$$R_{ij} = \sqrt{(\eta_i - \eta_j)^2 + (\phi_i - \phi_j)^2} \quad (4.3)$$

R_{ij} is a distance between the two particles on the $(\eta-\phi)$ space and R is the radius parameter which determines the final size of the jet, and it is usually between 0.4 - 0.7. The second distance parameter is $d_{iB} = P_{ti}^a$ ($a = -2$ for anti- k_T) is the momentum space distance between the beam axis and the detected particle. The anti- k_T clustering algorithms work by first finding the minimum of the entire set d_{ij}, d_{iB} . If d_{ij} is the minimum then particles i and j are combined into one particle (ij) using the summation of 4-vectors then which i and j are removed from the list of particles. If d_{iB} is the minimum, i is labeled a final jet and removed from the list of particles. This process is repeated until either all particles are part of a jet with the distance between the jet axis R_{ij} greater than R , which is called an

inclusive clustering, or until a desired amount of jets have been found that called exclusive clustering.

The anti- k_T algorithm is infrared and collinear safe and is currently the most widely used algorithm either at CMS or any of the other LHC experiment. In this search, we used the anti- k_T algorithm to cluster jets with a radius of 0.4 for Run2 that ATLAS and CMS Collaborations have agreed to use $R = 0.4$ as the default distance parameter so that results from jet measurements are directly comparable.

4.3 Jet Energy Calibration

Detector response to particles is not linear, and that's why it is not obvious to translate the measured jet energy to the true particle or parton energy. The jet energy corrections are a set of tools that allows the proper mapping of the measured jet energy deposition to the particle-level jet energy (except neutrinos). The jet energy corrections based on the factorized approach meaning different sets of corrections are defined and each level of correction takes care of a different physical effect. In order to do this, each level of correction is essentially a scaling of the jet four-momentum with a scale factor. Each level of correction is applied sequentially (the output of each step is the input to the next) and with a fixed order. These corrections depend on various jet related quantities like P_T , pseudorapidity (η), flavor, etc.. In the following, we describe the different type of jet energy corrections (Del Re, 2009).

1. **Offset:** Required correction for pile-up and electronic noise.
2. **Relative (η):** Required correction for variations in jet response with pseudorapidity relative to a control region.
3. **Absolute (P_T):** Required correction to particle level versus jet P_T in the control region.
4. **EMF:** Optional correction for variations in jet response with electromagnetic energy fraction.

5. **Flavor:** Optional correction to particle level for different types of jets (light quark, c, b, gluon)
6. **Underlying Event:** Optional correction for underlying event energy due to soft interactions involving spectator partons.
7. **Parton:** Optional correction to parton level.

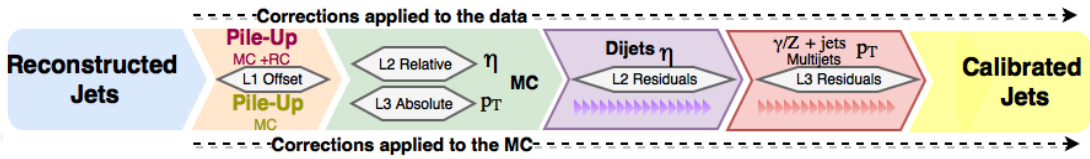


Figure 4.3: The Scheme of corrections applied to the jets in CMS.

The level of corrections applying to the jet measurement analysis (Harrel, 2017) in CMS discussed below and also shown in Figure 4.3.

L1 Offset Corrections : L1 correction removes the energy coming from pile-up events which are additional energy arising from secondary proton-proton collision inside a jet. To subtract the additional energy from the jet simulated of a sample of QCD dijet events processed with and without pileup overlay to process pileup offset corrections. They are parameterized as a function of offset energy density ρ , jet area A , and P_T . Corrections for residual differences between data and detector simulation as a function of eta are determined using the random cone method in zero-bias events which have no energy deposition from hard interactions. For this reason, different L1 corrections are applied to data and MC.

L2 relative and L3 absolute corrections: L2 relative correction was applied for minimizing the effect of non-uniformities between different sub-detector, meaning to make the flat response as a function of η from all sub-detector. After, the application of L2 corrections, L3 absolute corrections are applied versus jet P_T . For this, the simulated jet response corrections are determined on a QCD dijet sample, by comparing the reconstructed P_T to the particle-level one. The corrections are derived as a function of

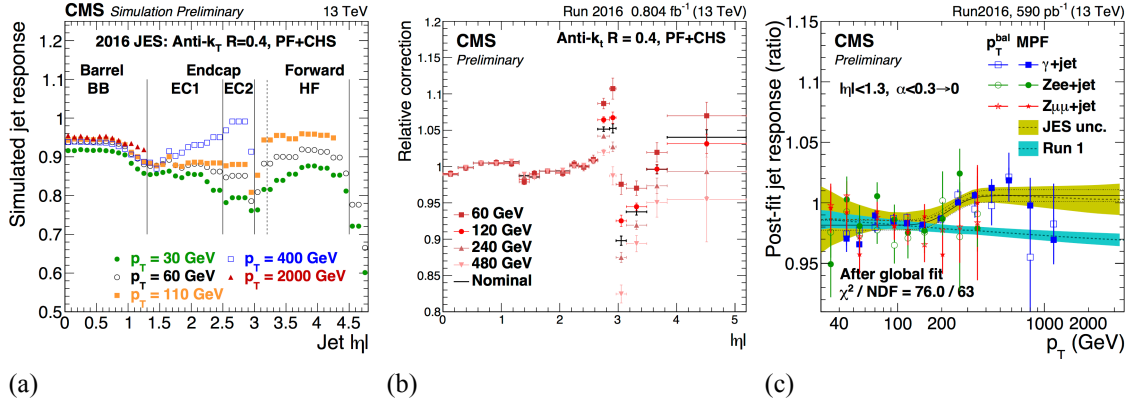


Figure 4.4: JET energy corrections for 2016 data taking. Simulated jet response from different part of detector (a), Data/MC residual correction for the dependency of the jet response on the jet η obtained on dijet event(b), Data/MC scale factors for the jet response p_T -dependence, evaluated from $\gamma + jet$, $Z(\rightarrow \mu\mu) + jet$ and $Z(\rightarrow ee) + jet$ events, combined in a global fit (c) (Harrel, 2017)

jet P_T and η to make the response uniform for these two variables. These two corrections are also applying both data and MC.

L2L3 Residual Corrections: This correction is only applying the data events which aim to correct differences within jet response in data and MC after the application of L1, L2, L3. The L2 Residuals eta-dependent corrections are determined with dijet events, relative to a jet of similar P_T in the barrel reference region. These corrections include a P_T dependence of the JES relative to the JES of the barrel jet. The L3Residuals correct the jet absolute scale (JES vs. P_T). These corrections are determined, for barrel jets, using $Z+jet$, $\gamma+jet$ and multijet events. Relative (vs. η) and absolute (vs. P_T) residual corrections are identified separately but they are stored in one single L2L3Residuals step for the analyzers.

5. MEASUREMENT OF DIJET MASS SPECTRUM

In this chapter, the details of the analysis and measurement of the dijet mass spectrum will be discussed.

5.1 Data Set and Monte Carlo Samples

The proton-proton collision data analyzed in this thesis. The data have been collected with the center of mass energy of $\sqrt{s} = 13$ TeV during 2016 by the CMS detector, with an LHC operation using the bunch spacing of 25 ns. The primary data set used for this study is JetHT dataset which collects most of the dijets events. The datasets used in this analysis is listed in Table 5.1 with corresponding good runs range and integrated luminosity (Benedikt, 2015). The total integrated luminosity of the selected data sample is 35.9 fb^{-1} .

Table 5.1: The data set used in this analysis with corresponding runs range and integrated luminosity

Data Set	Run Range	$L = \int Ldt$
/JetHT/Run2016B-23Sep2016A-v3/MINIAOD	273150-275376	5750.491 pb^{-1}
/JetHT/Run2016C-23Sep2016-v1/MINIAOD	275656-276283	2572.903 pb^{-1}
/JetHT/Run2016D-23Sep2016-v1/MINIAOD	276315-276811	4242.292 pb^{-1}
/JetHT/Run2016E-23Sep2016-v1/MINIAOD	276831-277420	4025.288 pb^{-1}
/JetHT/Run2016F-23Sep2016-v1/MINIAOD	277932-278808	3104.509 pb^{-1}
/JetHT/Run2016G-23Sep2016-v1/MINIAOD	278820-280385	7575.824 pb^{-1}
/JetHT/Run2016H-PromptReco-v2/MINIAOD	281207-284035	8434.663 pb^{-1}
/JetHT/Run2016H-PromptReco-v3/MINIAOD	284036-284068	215.965 pb^{-1}
Total	271036-284044	35991.875 pb^{-1}

The key to the search for dijet resonances is the measurement of the dijet mass distribution and the estimation of the background. Unlike many other searches in high energy physics, the search for dijet resonances is entirely dominated by a single background coming from the multi-jets event. The observed dijet mass distribution comes from the dominant process in hadronic collisions: $2 \rightarrow 2$ scattering of partons

predicted by perturbative QCD. The QCD samples are produced from Monte Carlo (MC) simulations. The MC simulation technique is used to understand experimental conditions and performance of the detector. The QCD multijet MC samples were produced using PYHTIA8 (Sjöstrand, 2007) with full CMS detector simulation that modeled in GEANT4 (Agostinelli, 2003). The MC samples are used the CUETP8M1 tune to model the QCD background. The tunes are set of parameter for the UE, modeling of the PYTHIA events. The CUETP8M1 tune is well described the 13 TeV data (Mrenna, 2016). These MC samples were produced using 25 ns bunch spacing, an asymptotic pile-up condition, and different transverse momentum (\hat{p}_T) binning, which allows large statistics in the tails of the dijet mass distributions. Table 5.2 shows the list of dataset names for background studies with the number of events, cross-section, and corresponding luminosity.

Table 5.2: Full datasets for the background with number of events, cross-section, and corresponding luminosity

Dataset	Cross Section (pb^{-1})	Number of Events	Equivalent luminosity (fb^{-1})
/QCD_Pt-300to470_TuneCUETP8M1_pythia8/	7823	5,970,600	0.7632
/QCD_Pt-470to600_TuneCUETP8M1_pythia8/	648.2	3,928,870	6.061
/QCD_Pt-600to800_TuneCUETP8M1_pythia8/	186.9	3,956,768	21.19
/QCD_Pt-800to1000_TuneCUETP8M1_pythia8/	32.293	3,976,136	123.1
/QCD_Pt-1000to1400_TuneCUETP8M1_pythia8/	9.4183	2,999,069	318.4
/QCD_Pt-1400to1800_TuneCUETP8M1_pythia8/	0.84265	396,409	470.4
/QCD_Pt-1800to2400_TuneCUETP8M1_pythia8/	0.114943	396,100	$3.466 \cdot 10^3$
/QCD_Pt-2400to3200_TuneCUETP8M1_pythia8/	0.0068298	399,226	$58.45 \cdot 10^3$
/QCD_Pt-3200_TuneCUETP8M1_pythia8/	0.000165445	383,926	$2321 \cdot 10^3$

5.2 The Event Selection

The dijet system is defined with two highest P_T jets, which are called the leading jets. These jets form the dijet mass $m = \sqrt{(E_1 + E_2)^2 - (\vec{p}_1 + \vec{p}_2)^2}$. The jet transverse energy is $E_T = E \sin \theta$, and the jet transverse momentum is $P_T = p \sin \theta$, where θ is the angle between the jet momentum and the beam. Both the momentum and jet energy are corrected back to the particles in the jet cone originating from the hard interaction excluding pileup. The PF jets used for this analysis are reconstructed using the anti- k_T algorithm with a radius parameter $R = 0.4$. These reconstructed jets allow us to account

for all the particles in each event. These particles can be electrons, muons, photons, charged hadrons and neutral hadrons, where direction, energy, and type are determined optimally from a thorough combination of data from all CMS sub-detectors.

Events are selected with the aim of minimizing the contribution of the overwhelming QCD dijet background and for maximizing the prominence of an excess. Leading jets are required to satisfy proper identification criteria. CMS has developed a set of jet quality criteria (“Jet ID”) for PF jets. The Jet ID is applied to remove most of the misidentified jets arising from calorimeter and readout electronics noise in pure noise non-collision data samples: such as cosmic-ray trigger data or data from triggers on empty bunches during LHC operation. The Jet ID criteria which are used in this analysis is “Tight” PF Jet ID. These Jet ID criteria are listed in Table 5.3.

Table 5.3: Tight Jet ID criteria that recommended from CMS (Rauco, 2017)

All η	$ \eta < 2.4$
Neutral Hadron Fraction < 0.90	Charged Hadron Fraction > 0.0
Neutral Hadron EM Fraction < 0.90	Charged Hadron Multiplicity > 0.0
Number of Constituents > 1	Charged EM Fraction < 0.90
Muon Energy Fraction < 0.80	

Events are rejected if at least one of the two leading jets does not pass the tight jet ID, or if it is outside of the tracker acceptance: $|\eta| < 2.5$. Events are also required that one of the leading jets has muon energy fraction smaller than 0.8 to reject mis-reconstructed muon events identified as jets and causing the massive non-physical tails in the dijet mass distribution.

The leading jet is required to have $P_T > 60$ GeV and the second leading jet is required to have $P_T > 30$ GeV. All leading jets are expected from the tracker acceptance $|\eta| < 2.5$ and passing the tight jet ID within $\Delta R = \sqrt{\Delta\phi^2 + \Delta\eta^2} < 1.1$ which allow us to geometrically close jets combine into “wide jets”, which will be used to reconstruct the invariant dijet mass. The center of each leading jets is a starting point the wide jet clustering, which is adding the four-momentum of any jet within $\Delta R = 1.1$ to the leading

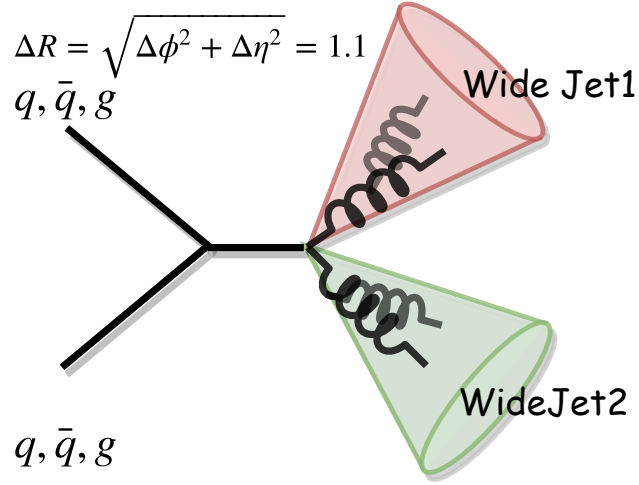


Figure 5.1: Illustration shows an event with final state radiation, where the use of the wide jet allows to contain the radiated energy that improves the dijet mass resolution.

jets. A wide jet allows better reconstruction of the energy of the hadrons in presence of final state radiation (FSR) and hence improves the dijet mass resolution. Figure 5.1 shows the illustration of the wide jets containing final state radiation.

The two leading jets are required to have $|\Delta\eta_{jj}^{\text{Wide}}| = |\eta_1 - \eta_2| < 1.3$, which is the angular separation of two leading jets. $|\Delta\eta_{jj}^{\text{Wide}}|$ depends on the emission of the final state partons from the beam line in the center-of-mass reference frame, meaning the scattering angle $\cos\theta^* = \tanh(\Delta\eta/2)$. The cut $|\Delta\eta_{jj}^{\text{Wide}}| < 1.3$ corresponds to the $\cos\theta^* < 0.57$ in the center-of-mass reference frame. Appendix A shows the derivation of $\cos\theta^*$ variable. There are several reasons for this $\cos\theta^*$ selection.

- This selection reduces the background and increases the significance of the signal. It suppresses QCD contributions more than it does the signal, which is an s-channel production, while QCD is t-channel.
- It defines a fiducial region for our measurement predominantly in the barrel.
- It provides a faster trigger turn-on curve for the jet trigger which uses H_T (scalar sum of P_T), allowing us to start the analysis at lower mass.

In order to reach good trigger efficiency, the invariant mass of two wide leading jets should be higher than about 1246 GeV. This requirement ensures that dijet mass spectrum is not disturbed much by trigger inefficiencies close to the low mass edge. More information will be given in Section 5.3.

Finally, additional jet energy correction (JEC) is applied to particle flow jets. L1 FastJet pile-up corrections, L2Relative and L3 Absolute corrections have used for both the data and MC, and L2L3Residual is applied to the data only for to account the small differences within jet response in the data and MC. The corrections are derived in four blocks of data organized according to the data taking runs as listed in Table 5.4.

Table 5.4: Table of jet energy correction (JEC) corresponding to each run period.

Run Period	JEC	Runs
1-276811	Summer16_23Sep2016BCDV4_DATA	B/C/D
276831-278801	Summer16_23Sep2016EFV4_DATA	E/early F
278802-280385	Summer16_23Sep2016GV4_DATA	lateF/G
280919-284044	Summer16_23Sep2016HV4_DATA	H

5.3 Trigger Efficiency

The trigger efficiency curve is essential to decide where we can start the fit in the dijet mass distribution, without disturbing the low mass region due to the trigger turn on. It is also essential to check if there are any failures at high mass, not to lose any exciting dijet events.

We used the following triggers in a logical order, which are *PFHT800*, *PFHT900*, *PFJet500*, *CaloJet500_NoJetID* and *DiPFJetAve500* respect to the *SingleMuon45* trigger, which requires the single muon $P_T > 45$ GeV. The name of the trigger is special for CMS, which indicates the jets properties used for this trigger. The jets are considered for trigger could be PFJets or CaloJets, depending on which part of detector energy deposit is considered. The H_T is defined as the scalar sum of the jets P_T . These triggers require at least one jet in the event with P_T above a certain threshold except the *DiPFJetAve500*

trigger, which requires two jets with average energy above the 500 GeV. Table 5.5 shows the these triggers name and their definition.

Table 5.5: Triggers name used in this analysis and their definition.

Trigger Name	Defination
<i>PFHT800</i>	$H_T > 800$ GeV
<i>PFHT900</i>	$H_T > 900$ GeV
<i>PFJet500</i>	PFJets, $P_T > 500$ GeV
<i>CaloJet500_NoJetID</i>	CaloJets, $P_T > 500$ GeV
<i>DiPFJetAve500</i>	PFJets, $(P_{T1} + P_{T2})/2 > 500$ GeV

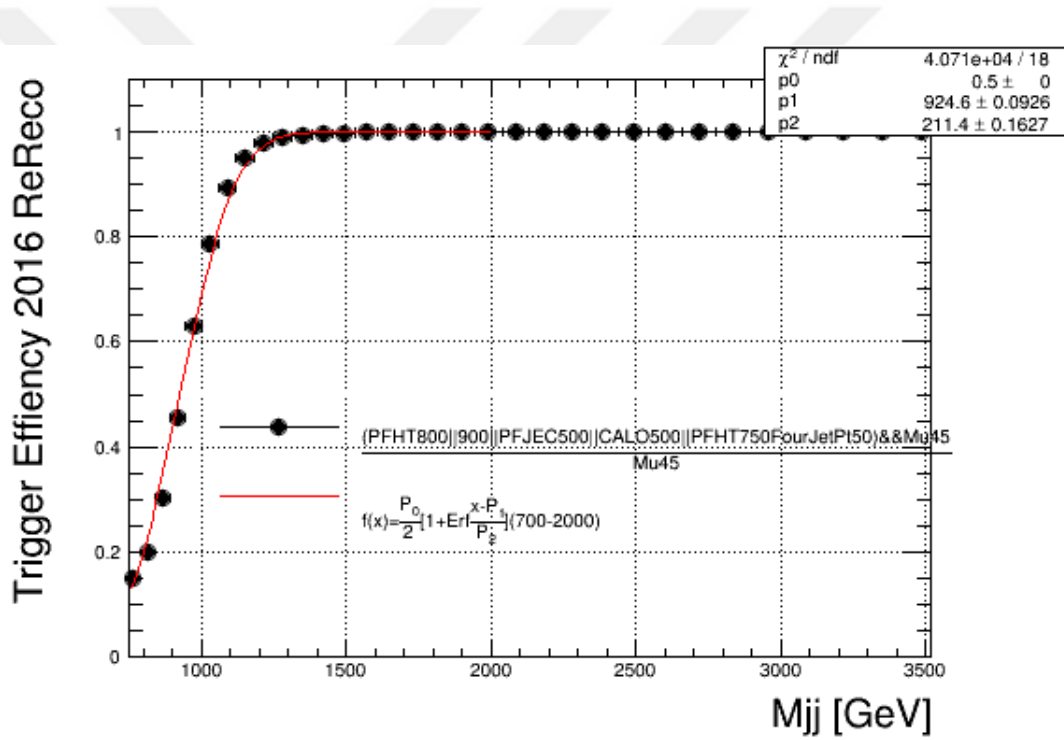


Figure 5.2: Trigger efficiency as a function of m_{jj}^{Wide} with the data (black dot) and fit function (continuous red line).

The trigger efficiency is calculated as a function of dijet mass; single muon is applied as the denominator. Other trigger applied as numerator which satisfies the denominator requirement with logical operator between them as shown in Equation 5.1. Figure 5.2 shows the trigger efficiency as a function of dijet mass. In the analysis, the trigger is 98% efficient for dijet masses above 1246 GeV. Therefore, this mass value will be chosen as a starting mass point for this analysis.

$$\frac{(PFHT800 \parallel 900 \parallel PFJEC500 \parallel CALO500 \parallel PFHT750 \text{Four Jet Pt150}) \&\& Mu45}{Mu45} \quad (5.1)$$

5.4 Data Quality Studies

A comparison between the data and QCD MC simulation is performed to examine and study the quality of our data and how robust our event and jet selection are against beam and detector related noise, detector pathologies, reconstruction catastrophic failures etc. The MC distribution is normalized to the number of events in the data by multiplying the value of the 0,82 (data/MC) to have a better agreement between the data and MC. All plots are shown in this section are re-scaled with this value.

Firstly, we compare the dijet mass spectrum with QCD MC simulation and the data. The dijet mass spectrum is in good agreement between the data and QCD MC simulation. The highest mass event is equal to $m_{jj}^{\text{Wide}} = 7.8$ TeV. Figure 5.3 shows the comparison between the data and QCD MC simulation for the dijet mass spectrum.

The other event related distributions are listed below:

- $\frac{E_T^{\text{miss}}}{\sum E_T}$: The ratio of the missing transverse energy to the total transverse energy; the balance of the event energy in the transverse plane. This variable is related to the detector noise which would create a significant energy imbalance. The detector noise tends to show up at higher values of this ratio. So we choose the $MET / \sum E_T < 0.5$ to clean up jet mis-reconstruction problems at very high jet P_T . Figure 5.4 on the left side shows the ratio of $MET / \sum E_T <$
- $\Delta\phi = \phi_1 - \phi_2$: the angle between the two leading jets in the transverse plane; this variable is also sensitive to the detector noise, as the fake jets would take place in the regions away from the $\Delta\phi = \pi$. Figure 5.5 on the right side shows the comparison between the data and MC simulation for this variable.

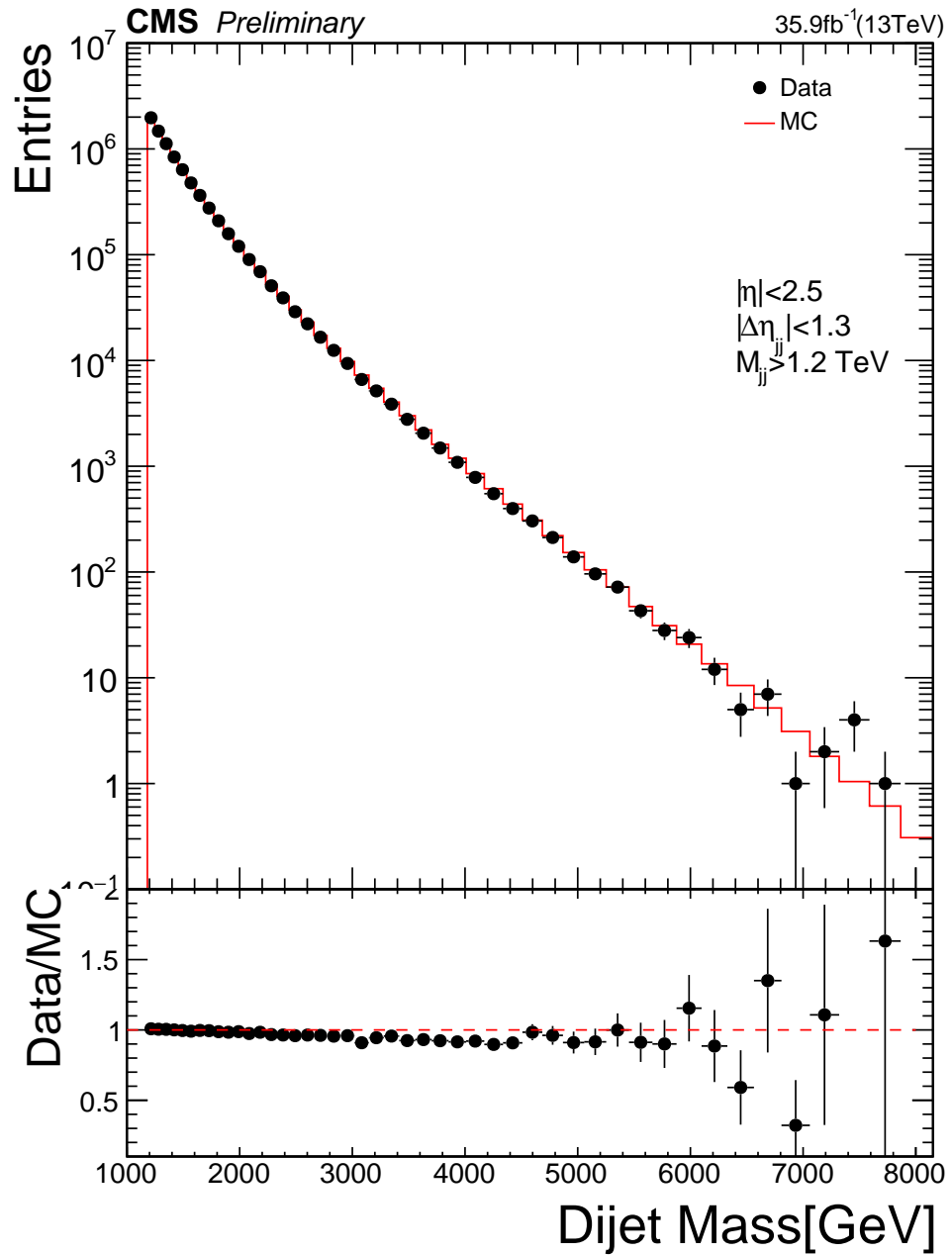


Figure 5.3: Dijet mass spectrum after full analysis main cut selection. The back markers shows the data the red line shows QCD simulation.

- $\Delta\eta = |\eta_1 - \eta_2|$: the absolute difference in pseudorapidity between two leading wide jets. Figure 5.5 on left shows the comparison between the data and MC simulation for $\Delta\eta$.
- $\cos(\theta^*) = \tanh \frac{\Delta\eta_{ij}}{2}$: the angle between the scattering partons and colliding partons at the center-of-mass frame. The $\Delta\eta$ and $\cos(\theta^*)$ show how forward the dijet

production is. These variables also sensitive to noise and any diversion from the expectation would be the indication of data pathologies. Figure 5.4 on the right side shows the comparison between the data and MC simulation for $\cos(\theta^*)$

The Jet identification criteria or “Jet ID” is also performed in the data quality study that based on the jet energy component listed below:

- The charged hadron fraction (CHF), representing mostly the charged pions (π^\pm) jet content are shown in Figure 5.6 on the right.
- The neutral hadron fraction (NHF), mainly describing the long living neutral hadrons like Λ^0 , neutrons and kaons jet content. Also, if HCAL has a noise problem, we expect an excess of the jets neutral hadron fraction in data with respect to simulated (MC) events. Figure 5.6 shows the comparison between data and MC simulation for the NHF.
- The neutral electromagnetic jet energy fraction (NEMF), which represents mostly pions that quickly decays in photons ($\pi^0 \rightarrow \gamma\gamma$). Figure 5.6 shows the comparison between data and MC simulation for this variable.
- We also perform the neutral particle multiplicity, photon multiplicity, the charged electromagnetic fraction, and the muon fraction to check for the data pathologies. Figure 5.7 and Figure 5.8 shows comparison between data and MC for these variable.

The data quality for kinematic quantities which are P_T , η , and ϕ also performed for investigation of detector pathologies against our jet selection. Figure 5.9 shows these kinematic quantities for two leading wide jets .

The data quality studies are shown that the data samples are clean, with no pathologies and no indication of noise present, after an event and jet selection criteria are applied.

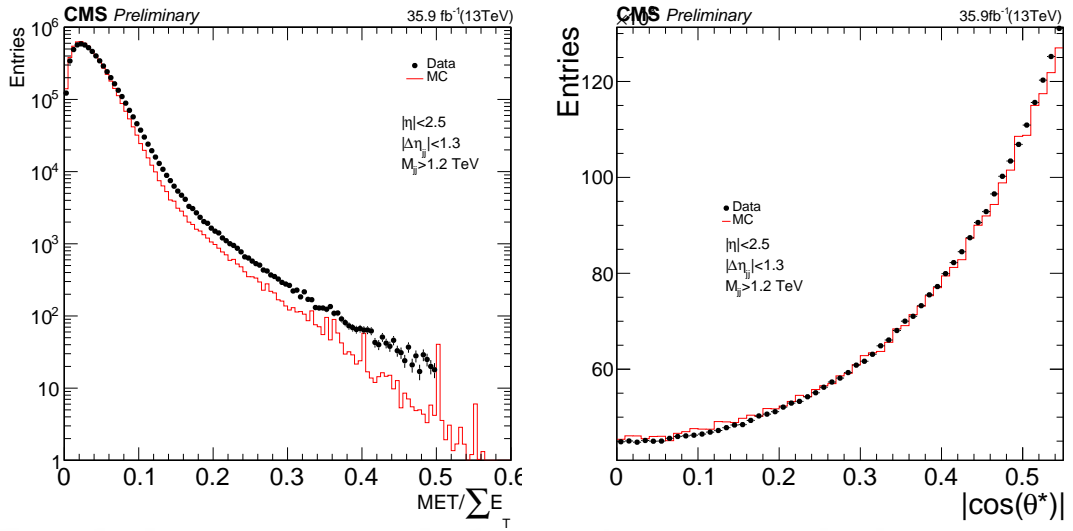


Figure 5.4: The ratio of the transverse missing energy to the total transverse energy of the event (left) and the angle between beam axis and the dijet system at the center of mass frame ($\cos(\theta^*)$) (right) for data (points) and simulated (continuous histogram) events

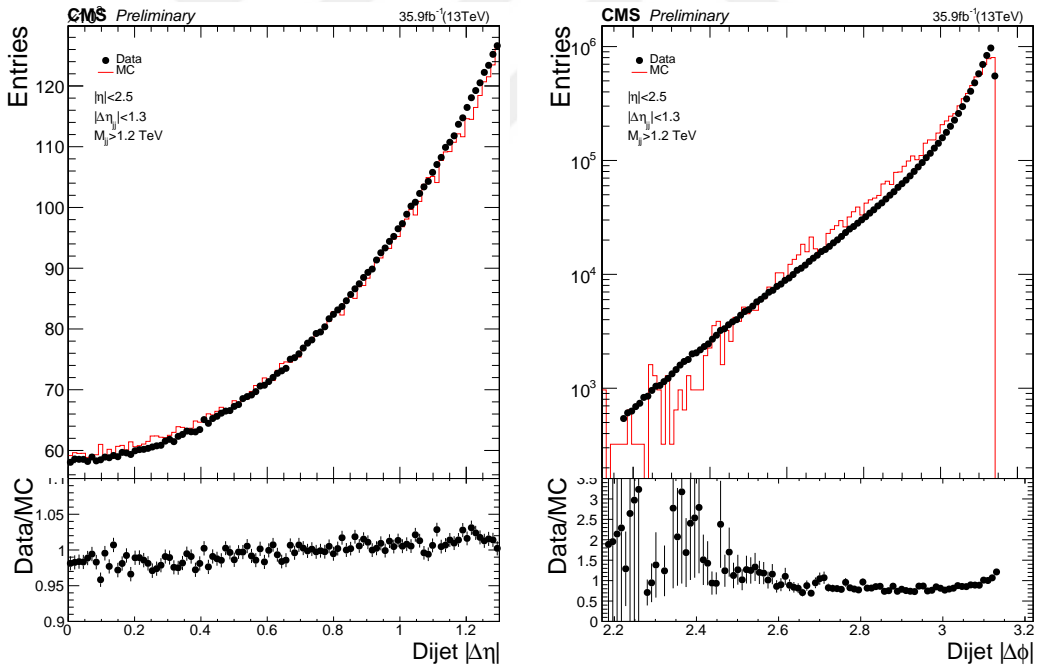


Figure 5.5: The absolute difference in pseudorapidity between two leading wide jets ($\Delta\eta$) (left) and the angle of the two leading jets in the transverse plane ($\Delta\phi$) (right) for data (points) and simulated (continuous histogram) events.

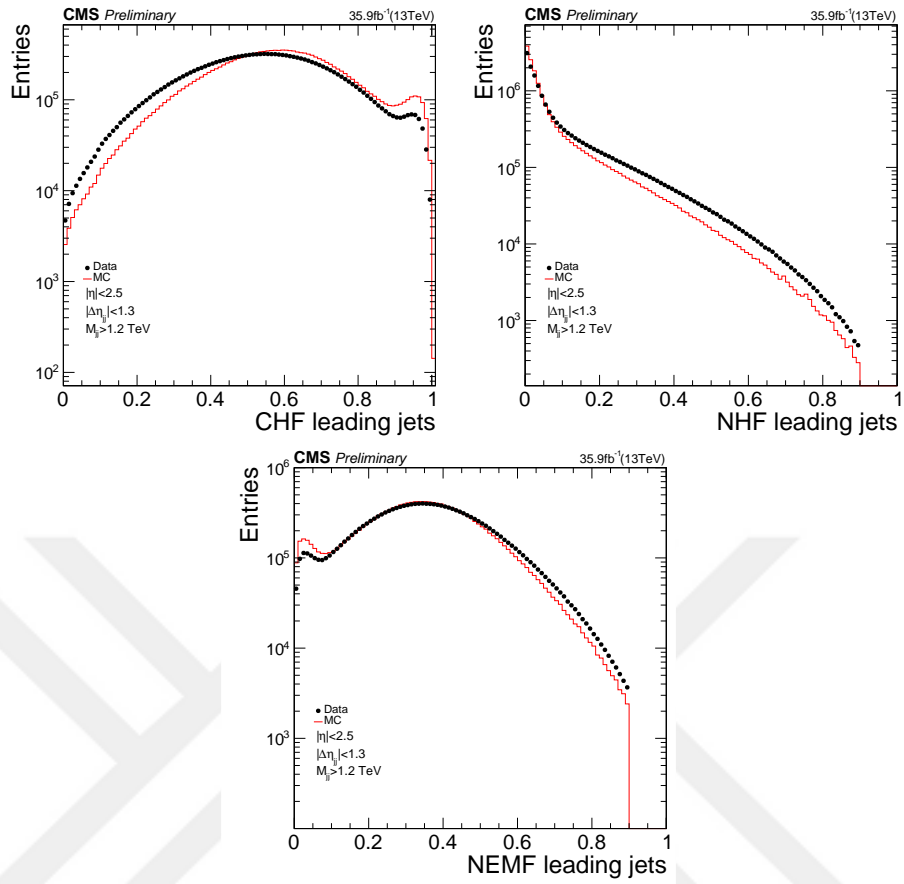


Figure 5.6: The charged hadron fraction (CHF) (top left), the neutral hadron fraction (NHF) (top right), and the neutral electromagnetic jet energy fraction (NEMF) (Bottom) for data (points) and simulated (continuous histogram) events.

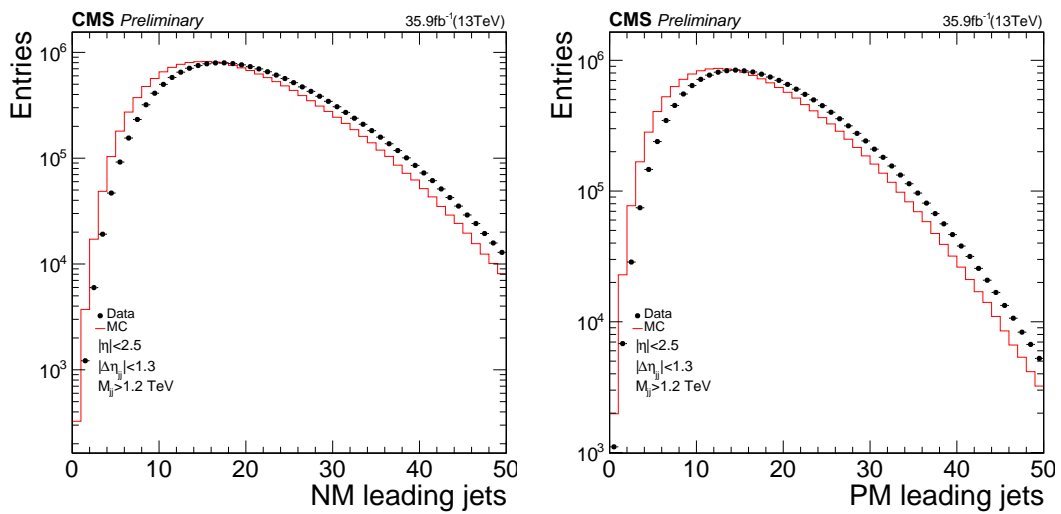


Figure 5.7: The neutral particle multiplicity (NM) (left) and the photon multiplicity (PM) (right) for data (points) and simulated (continuous histogram) events.

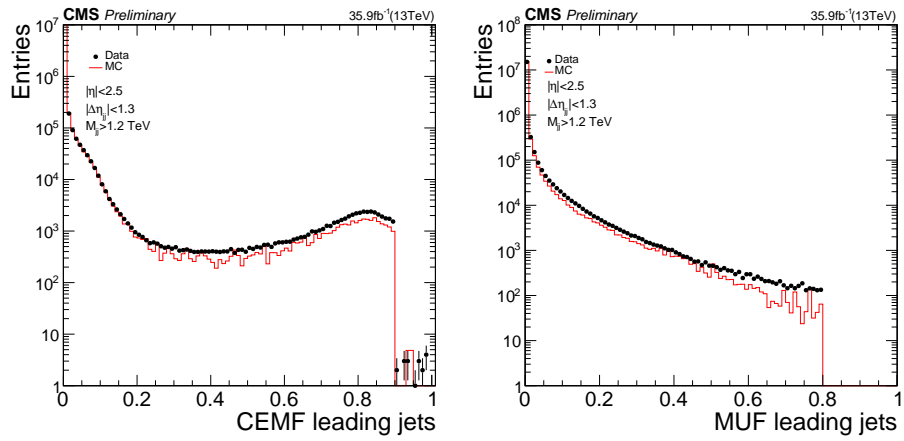


Figure 5.8: The charged electromagnetic fraction (CEMF) (left) and the muon fraction (MUF) (right) for data (points) and simulated (continuous histogram) events.

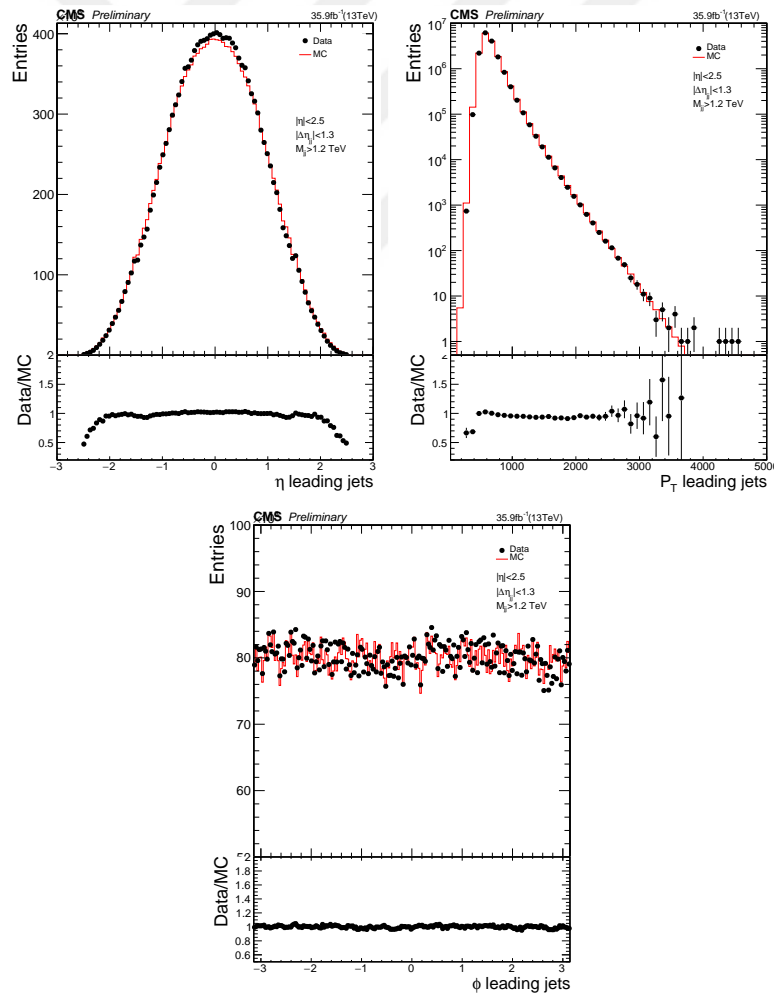


Figure 5.9: η (top left), the transverse momentum (p_T) (top right), and ϕ (bottom) for data (points) and simulated (continuous histogram) events.

5.5 Dijet Mass Spectrum and Fit

The measured dijet mass spectrum is formed as a differential cross section.

$$\frac{d\sigma}{dm} = \frac{1}{\int L dt} \frac{N_i}{\Delta m_i}, \quad (5.2)$$

where m is the dijet mass, N_i is the number of events in the i^{th} dijet mass bin, and Δm_i is the width of the i^{th} dijet mass bin, and the integrated luminosity is $\int L dt$. The estimation of background for this analysis is obtained directly from data and does not rely on MC simulation. Variable dijet mass bins in the distribution are used to have bins with roughly equal dijet mass resolution.

The background estimation obtained from a likelihood fit with a background-only hypothesis is used in order to test the smoothness of the observed data. The following parametrization of a smooth fit function defined as

$$\frac{d\sigma}{dm} = \frac{P_0 (1 - m_{jj}/\sqrt{s})^{P_1}}{(m_{jj}/\sqrt{s})^{P_2 + P_3 \log(m_{jj}/\sqrt{s})}}, \quad (5.3)$$

where $\sqrt{s} = 13$ TeV and $P_{0,1,2,3}$ are free parameters. The binned, background only, maximum likelihood is fit to the data with the following likelihood,

$$\mathcal{L}(data | \theta) = \prod_{i=1}^{n_i} Poisson(x_i | b_i(\theta)) = \prod_{i=1}^{n_i} \frac{b_i(\theta)^{x_i} e^{-b_i(\theta)}}{x_i!}, \quad (5.4)$$

where θ is the vector of nuisance parameters (p_0, p_1, p_2, p_3) , n_i is the number of bins, x_i is the data yield in bin i , b_i is the integral of the fit function in bin i multiplied by the total number of expected events N_b .

$$b_i(\theta) = N_b \int_{m_{jj}^{min,i}}^{m_{jj}^{max,i}} dm_{jj} p(m_{jj}). \quad (5.5)$$

Figure 5.10 shows the measured dijet mass spectrum formed as a differential cross section with smooth background-only fit function. The maximum likelihood fit to the data in the range $1246 < m_{jj} < 7866$ GeV. The differences between the data and the fit are also shown at the bottom of the figure. The data are well described by the smooth fit and the values of χ^2/ndf obtained from the fits that show how the fit function well describes the data. The chi-squared (χ^2) is 36.1 for 40 degrees of freedom. There is no evidence for the dijet resonances in the measured dijet mass spectra.

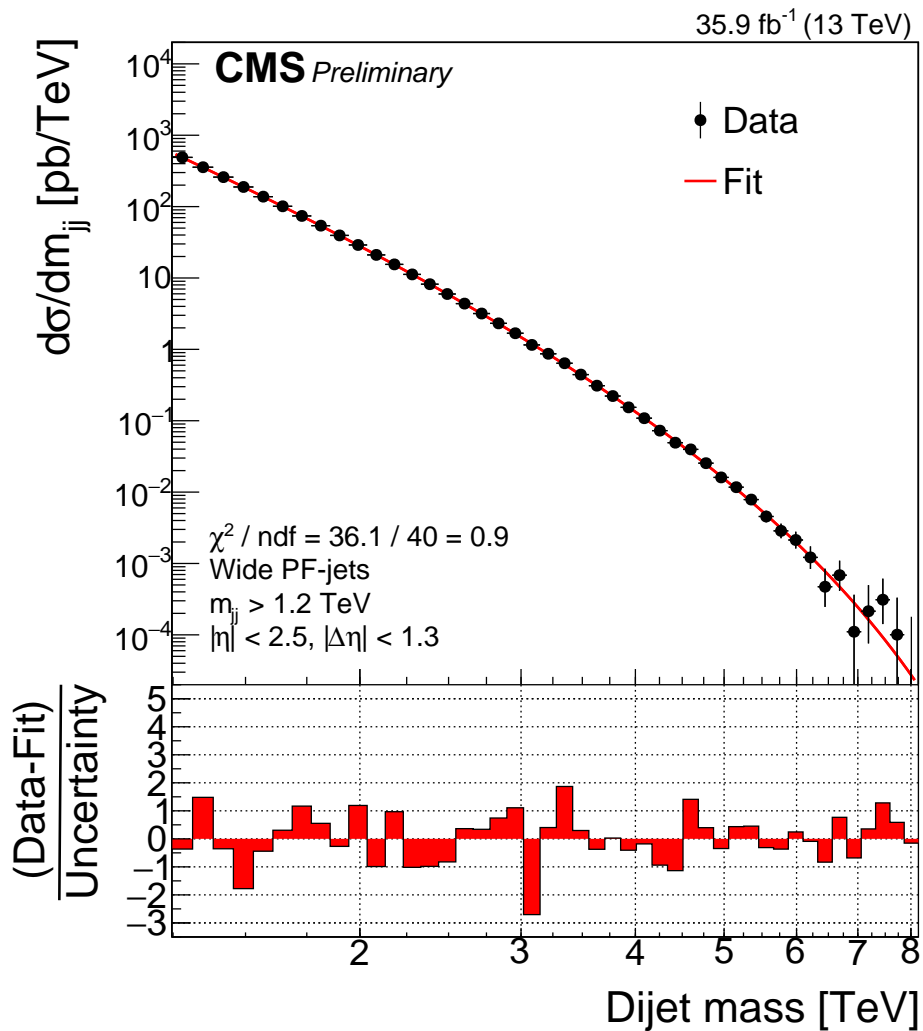


Figure 5.10: The binned fit for PF RECO performed in the range $1246 < m_{jj} < 7866$ GeV. The black point represents the observed data, the continuous red line represents the smooth fit function.

6. SEARCH FOR DIJET RESONANCES

6.1 Signal Modeling

In this analysis, we search only for narrow resonances decaying to qq, qg, gg final states. The natural width of these final states are negligible to when compared to the CMS dijet mass resolutions. Therefore, resonance shape is not as affected by natural width as they are affected by the types of the parton pairs in the resonance decay (qq, qg, gg). The process to procure general shapes for these parton pair types are $qg \rightarrow q^* \rightarrow qg$, $qq \rightarrow G \rightarrow qq$, and $gg \rightarrow G \rightarrow gg$. These signal shapes are obtained using PYTHIA8 simulation at ten different mass points, at 500 GeV and from 1 up to 9 TeV with a step of 1 TeV. RunIISpring16 MC samples are used in this search with about 100k events, which are produced with CMSSW_8_0_X. Table 6.1 shows the detail of signal samples that used for this search.

Table 6.1: The data sets for signal samples which used in this analysis, *XX stand for mass point which used 0.5 TeV and 1 to 9 TeV . *YY is stand for RunIISpring16MiniAODv2-PUSpring16_80X_mcRun2_asymptotic_2016_miniAOD_v0-v1/MINIAODSIM

<i>/RSGravitonToGluonGluon_kMpl01_M_XX_TuneCUETP8M1_13TeV_pythia8/ *YY</i>
<i>/RSGravitonToQuarkQuark_kMpl01_M_XX_TuneCUETP8M1_13TeV_pythia8/ *YY</i>
<i>/QstarToJJ_M_XX_TuneCUETP8M1_13TeV_pythia8/ *YY</i>

Figure 6.1 shows the resonance shape for the three type of parton pairs (qq, qg, gg). Each parton pair is generated from 10 mass points. The width of the dijet resonances increases with the number of gluons in the final state because the gluons emit more radiation than quarks. But, the CMS detector has limited response to the gluons that affects the peak value of dijet resonance mass, decreasing with the number of gluons in the final state. Therefore the shape of the gluon-gluon resonance is the widest of the three and shifted to the lower dijet mass region. There is a low-mass tail on the resonances mostly coming from FSR, and the high-mass tail is enriched by ISR. An

interpolation technique used to produce the intermediate masses for every 100 GeV. This technique is discussed in Appendix B.

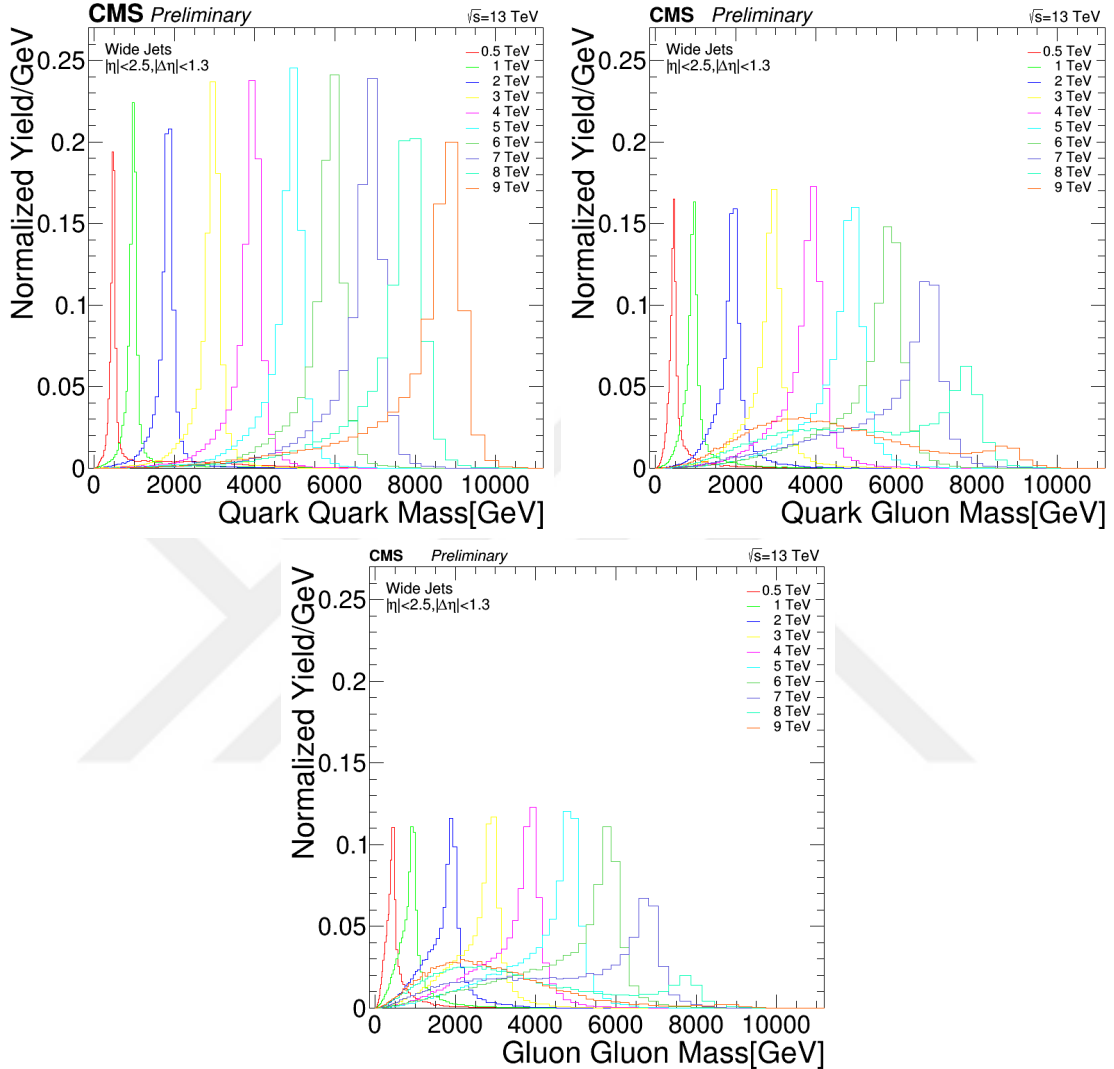


Figure 6.1: Dijet resonance shapes for all considered parton pairs decay at ten different mass point. $qq \rightarrow G \rightarrow qq$ (top left) , $qg \rightarrow q^* \rightarrow qg$ (top right), and $gg \rightarrow G \rightarrow gg$ (bottom).

Figure 6.2 shows dijet mass spectrum with the data compared to a smooth fit function including the narrow resonance signal models. The signal samples of three final states are gg , qg , and qq at the resonance mass values 2.0, 4.0, and 6.0 TeV corresponding resonance models are color-octet scalar, excited quark, and scalar diquark, respectively.

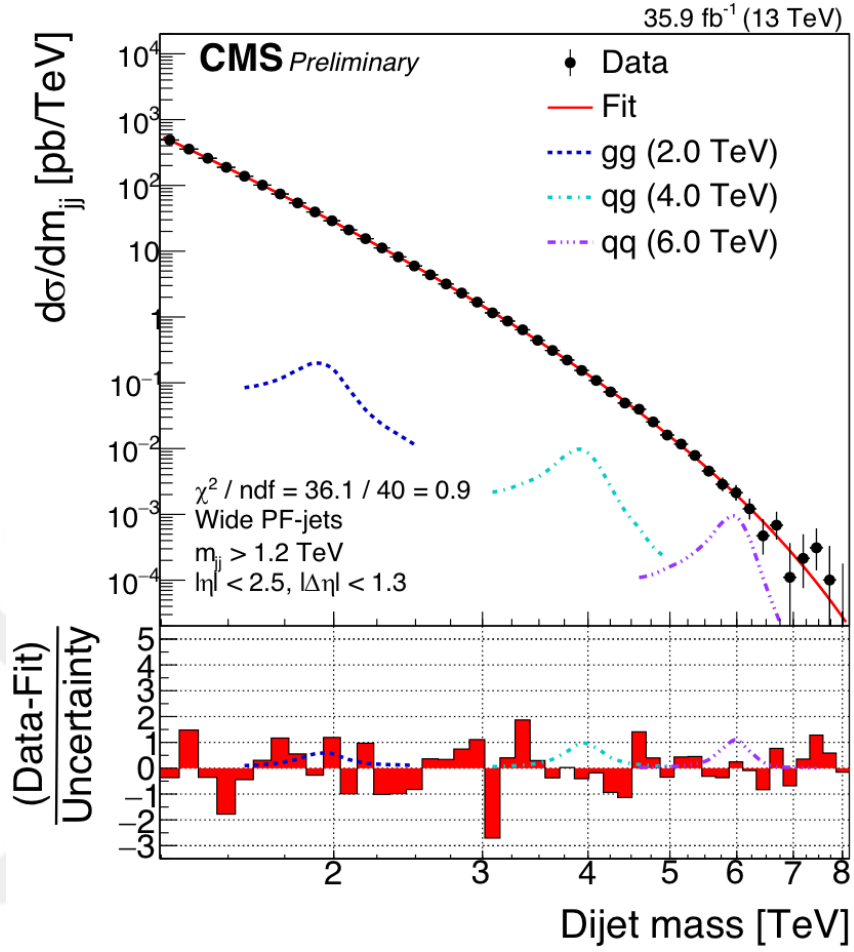


Figure 6.2: Dijet mass spectrum with the data (points) compared to a smooth fit function (solid line) including the narrow resonance signal models (dot-dashed). The signal of three final states is gg, qq, and qq at the resonance mass values 2.0 TeV, 4.0 TeV, and 6.0 TeV corresponding resonance models are color-octet scalar, excited quark, and scalar diquark, respectively

6.2 Significance of the Observed Excess

The significance calculation shows us the probability of between two variables. In here we used the background+signal sample over the background to search the relation between them. The likelihood-based on estimator using to calculate the significance of local excess in the data that defined by:

$$S_L = \sqrt{2 \ln \frac{L_{S+B}}{L_B}} \quad (6.1)$$

where L_B is maximum likelihood from the background-only fit to the data and L_{S+B} is maximum likelihood from the background+signal fit to the data.

The significance calculation has been performed in the limit setting framework, which the same framework we have been used for the limit calculation. In this framework, the same background parametrization, likelihood function, signal shapes are used, but we did not include the systematic effect to calculate the significance in this section. We

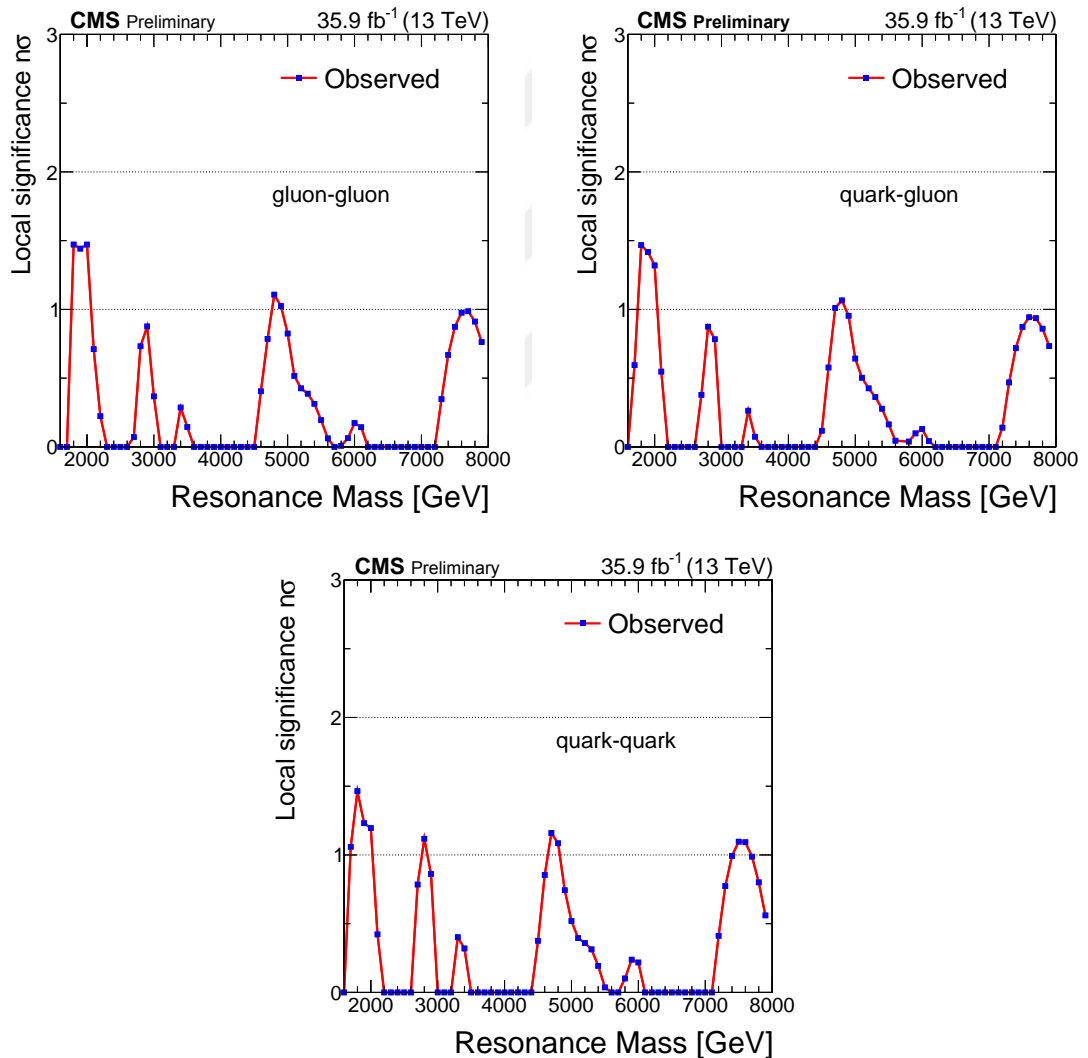


Figure 6.3: Local significance of a gg resonance (top left), a qg resonance (top right), and a qq resonance (bottom) are calculated with the observed data (points) for every 100 GeV.

calculated the significance as a function of resonance mass for three type of signal samples for every 100 GeV. The results of a significance for three resonance types are(qq, qg, gg) shown in Figure 6.3. The local significance is reached around $\sim 1.5\sigma$ for these samples.

6.3 Calculation of Cross section Upper Limits

The measured dijet mass distribution is well defined with the background fit model, and the significance of any observed excesses do not see any evidence of production of massive particles in the dijet mass distributions. Thus, we proceed to set an upper limit on the cross section times branching ratio of a dijet mass.

We calculated the 95% confidence level exclusion limits on the cross section times branching ratio of the dijet resonance using the modified Frequentist method. The modified Frequentist method is statistical approaches commonly used in high energy physics for setting the upper limits with an absence of signals. The limit calculation for a given signal is based on an evaluation of the likelihood that the observed spectrum is better represented by a combination of signal and background than a background only distribution. In other words, we quantify the level of incompatibility of the data with the hypothesis that the data contains a signal.

The Frequentist approach begins by defining a test statistic q_μ with the signal strength μ . The test statistic in the modified Frequentist approach is a logarithmic ratio of signal + background and background only likelihoods. The test statistic is given by:

$$q_\mu = -2\ln \frac{\mathcal{L}(\text{data} | \mu_s + b)}{\mathcal{L}(\text{data} | \hat{\mu}_s + b)}, \quad \hat{\mu} \geq 0 \quad (6.2)$$

where $\hat{\mu}$ is the signal strength that maximizes the likelihood $\mathcal{L}(\text{data} | \mu_s + b)$. In the modified Frequentist (CL_s) method the confidence of the signal+background hypothesis

is defined with the observed data q_μ^{data} as

$$CL_{s+b} = P(q_\mu \geq q_\mu^{data} | \mu_s + b), \quad (6.3)$$

which is calculated from the observed distribution. In addition, for evaluating the confidence of the background only hypothesis, defined as

$$CL_b = P(q_\mu \geq q_\mu^{data} | b) \quad (6.4)$$

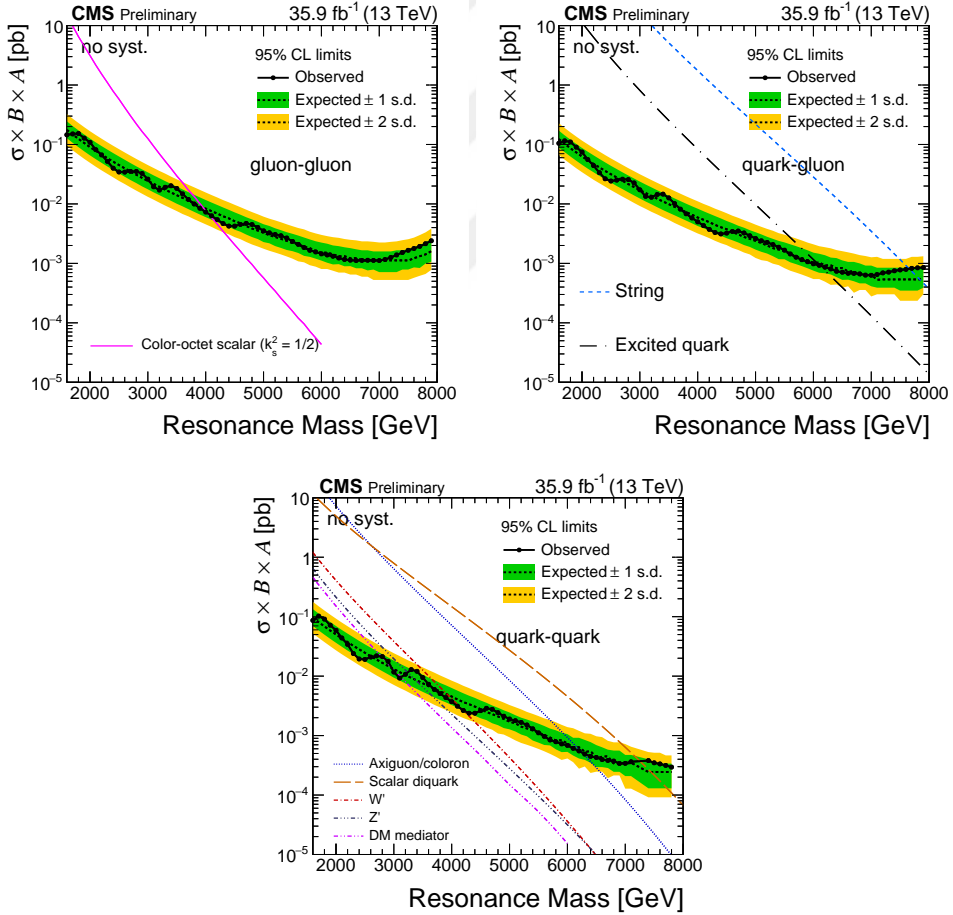


Figure 6.4: %95 CL upper limits on $\sigma \times BR \times A$ for gg resonance (top left), qg resonance (top right), and qq resonance (bottom) with only statistic uncertainties.

The modified Frequentist confidence level variable CL_s are calculated as the ratio of the signal+background and background only probabilities:

$$CL_s = \frac{CL_{s+b}}{CL_b} \quad (6.5)$$

In the modified Frequentist approach CL_s that is required to be less than or equal to 0.05 in order to declare the 95% C.L. exclusion.

The 95% CL upper limits on cross-section times branching ratio times dijet events acceptance is calculated with the only statistical error. Figure 6.4 shows the %95 CL upper limits on $\sigma \times BR \times A$ for a gg, a qq, and qg resonances. The procedure described so far does not include the systematic uncertainties. In the next section, the systematic uncertainties will be described, which affects the upper limits results.

6.4 Systematic Uncertainties

The standard methodology for incorporating systematic uncertainties into dijet resonance search contain the following source of systematic uncertainties:

- Jet Energy Scale (JES),
- Jet Energy Resolution (JER),
- Background parameterization,
- Integrated luminosity.

6.4.1 Jet energy scale

The JES uncertainty is a relative error the between the jets in the signal simulation and where the signal would emerge in the real data. Summer16_23Sep2016 uncertainties where used in this analysis, which are recommended by JETMET group.

These uncertainties on the jet P_T propagate almost linearly to the dijet mass. A single 2% value is used for all the mass range considered in this analysis and spread to the limit setting procedure.

6.4.2 Jet energy resolution

The uncertainty on the jet energy resolution translates into an uncertainty of 10% on the resolution of the dijet mass. This value was also recommended by JETMET. This uncertainty is propagated to the search by changing the width of the resonance shape by $\pm 10\%$, which results in slight stretching or shrinking of the resonance shape itself.

6.4.3 Background parametrization

The smooth fit function defined in Equation 5.3 has four free parameters. The reasonable starting point of these parameters determines after the fit to the data. These parameters have a non-diagonal covariance matrix, suggesting a degree of correlation among them. This covariance matrix is diagonalized, with its eigenvalues becoming diagonal elements and a conversion from the original correlated parameters to new uncorrelated parameters is obtained. Eigenvalues of the original covariance matrix correspond to variances or error squared, of the new uncorrelated parameters, and new uncorrelated parameters are eigenvectors of the original covariance matrix. These new uncorrelated parameters are present as nuisance parameters to take account the uncertainty result from the choice of the background parameterization. In practice, to integrate the likelihood over these nuisance parameters, the initial four parameters are varied from their best fit values in a correlated fashion, along with the eigenvectors of the covariance matrix.

6.4.4 Integrated luminosity

The brilcalc tool (Lujan, 2015) is used to calculate the luminosity for this analysis. It is important to use the correct normtag with the brilcalc tool. The normtag contains

the latest official calibrations for the appropriate run period. For the 2016 pp run the recommended normtag is normtag_PHYSICS.json (Pua, 2016). This recommendation corresponds 2.5% uncertainty on the integrated luminosity. As a result, the integrated luminosity calculated using the recommended normtag for the 2016 data taking, resulting 35.9 fb^{-1} .

6.5 Exclusion Limits with Systematic Uncertainties

The likelihoods definition when including the systematics uncertainties can be extended to include the nuisance parameter. The Poisson distributions with different bins given by:

$$\mathcal{L}(\text{data} \mid \mu, \theta) = \prod_{i=1}^{n_i} \text{Poisson}(x_i \mid s_i(\mu, \theta) + b_i(\theta)) \cdot \text{Constraint}(\theta \mid \tilde{\theta}, \delta\theta), \quad (6.6)$$

where θ is the vector of nuisance parameters, x_i is the data yield in the i^{th} bin, $b_i(\theta)$ the corresponding background yield, $s_i(\mu, \theta)$ the corresponding signal yield, and n_i the number of bins. The constraint terms used for different nuisance parameters are summarized in Table 6.2

Table 6.2: The constraints associated to systematic uncertainty nuisance parameters.

Systematic Uncertainty	Constraint
Jet Energy Resolution	Gaussian
Jet Energy Scale	Gaussian
Luminosity	LogNormal
N_b, p_0, p_1, p_2	Uniform

In the Frequentist paradigm, the systematic uncertainties related to the nuisance parameter θ , both the numerator and denominator likelihoods can be maximized with respect to nuisance parameters. The test statistic for LHC CL_s then would take the following form:

$$\tilde{q}_\mu = -2 \log \frac{\mathcal{L}(\text{data} \mid \mu, \tilde{\theta}_\mu)}{\mathcal{L}(\text{data} \mid \tilde{\mu}, \tilde{\theta})}, \quad 0 \leq \tilde{\mu} \leq \mu. \quad (6.7)$$

To obtain the observed 95% CL upper limit on the signal strength in the asymptotic approximation, we define the value of μ that satisfies,

$$CL_s \equiv \frac{CL_{s+b}}{CL_b} = \frac{1 - \Phi(\sqrt{\tilde{q}_\mu})}{\Phi(\sqrt{\tilde{q}_{\mu,A}} - \sqrt{\tilde{q}_\mu})} = \alpha \quad (6.8)$$

where $\alpha = 0.05$ and q is the test statistic determined on the Asimov dataset corresponding to the nominal nuisance parameters (setting all fluctuations to be zero) and the expected background. A similar expression is used to obtain from the median expected 95% CL upper limit,

$$\sqrt{\tilde{q}_{\mu,A}} = \Phi^{-1}(1 - 0.5\alpha), \quad (6.9)$$

and to find the N_σ uncertainty band around the expected limit,

$$\sqrt{\tilde{q}_{\mu,A}} = \Phi^{-1}(1 - \alpha \Phi(N) + N). \quad (6.10)$$

In the Figure 6.5, the black points indicate the observed upper limits on $\sigma \times BR \times A$ for qq, qg, and qq resonances at 95% CL. The black dashed line represents the expected upper limits in the hypothesis of no signal, and the green and yellow bands stand for 1σ , and 2σ uncertainty bands, respectively. The observed (expected) curves are below the signal models up to particular masses, meaning that in those regions the corresponding models are excluded. When the observed (expected) curves cross the signal models, those marks determine the mass upper limit for corresponding signal models and the above that point the analysis become sensitive, and no conclusions can be said about signal modeling until we get more data to reach that point to speak up.

Figure 6.6 shows the ratio of 95% CL upper limits on $\sigma \times BR \times A$ without systematic uncertainties to the with systematic uncertainties for gg, qg, and qq resonances. Figure 6.7 shows the summary of the observed upper limits for three parton pair types and all signal resonance models on the same plot.

Finally, Table 6.3 shows observed and expected mass limits at 95% CL on models of dijet resonances with corresponding luminosity is 35.9 fb^{-1} at $\sqrt{s} = 13 \text{ TeV}$.

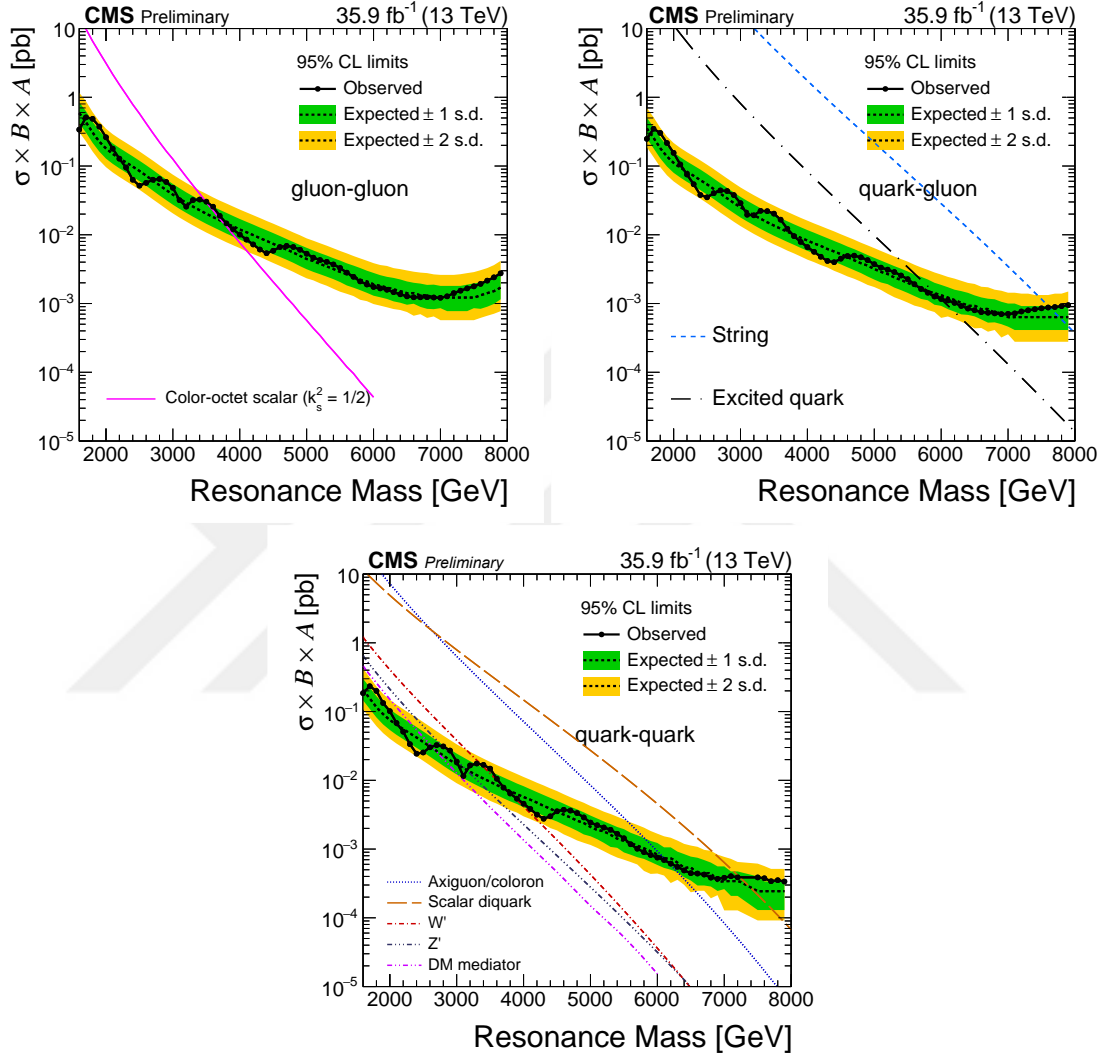


Figure 6.5: %95 CL upper limits on $\sigma \times BR \times A$ for gg resonance (top left), qg resonance (top right), and qq resonance (bottom) with systematic uncertainties. The black points indicates the observed upper limits, the black dashed line represents the expected upper limits, and the green and yellow bands stand for 1σ , and 2σ uncertainty bands, respectively.

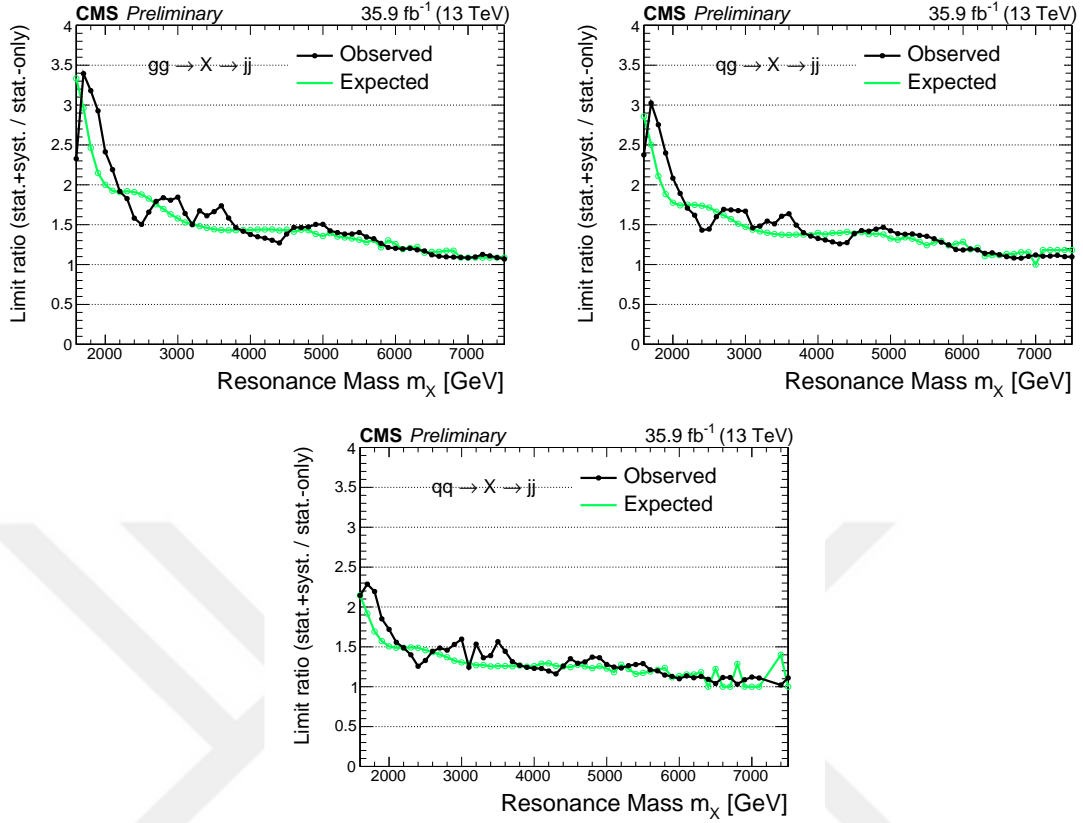


Figure 6.6: The ratio of 95% CL upper limits on $\sigma \times BR \times A$ for a gluon-gluon resonance (top left), a quark-gluon resonance (top right), and a quark-quark resonance (bottom) with and without systematic uncertainties.

Table 6.3: The observed and expected upper mass limits at 95% CL on models of dijet resonances with corresponding luminosity is 35.9 fb^{-1} at $\sqrt{s} = 13 \text{ TeV}$.

Model	Final State	Observed [TeV]	Expected [TeV]
String	qg	7.6	7.7
Scalar diquark	qq	7.2	7.4
Axigluon/Coloron	$q\bar{q}$	6.1	6.0
Exited quark	qg	6.0	5.8
Color-octet-scalar ($k_s^2 = 1/2$)	gg	3.4	3.6
W'	$q\bar{q}$	3.3	3.6
Z'	$q\bar{q}$	2.7	2.9
RS Graviton	$q\bar{q}, gg$	1.7	2.1

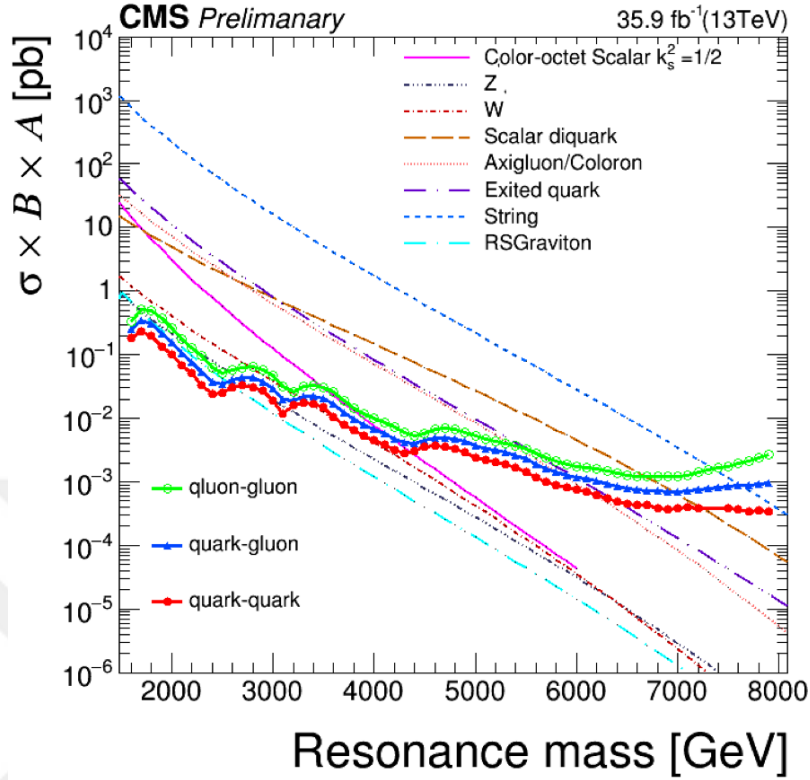


Figure 6.7: The observed upper limits 95% CL on $\sigma \times BR \times A$ for dijet resonance of the gluon-gluon, quark-gluon, and quark-quark compared to the theoretical predictions for color octet scalar, new gauge boson Z' and W' , scalar diquarks, axigluons/colorons, string resonances, and RSGraviton.

Table 6.4: Observed and Expected Upper Limits at 95% CL on $\sigma \times BR \times A$ for a gg resonance, a qg resonance, and qq resonance as a function of resonance mass with systematic uncertainties

Mass [GeV]	95 % Upper Limit [pb]					
	gg		qg		qq	
	Observed	Expected	Observed	Expected	Observed	Expected
1600	3.38e-01	5.86e-01	2.48e-01	3.52e-01	1.85e-01	2.07e-01
1700	5.10e-01	4.36e-01	3.48e-01	2.57e-01	2.34e-01	1.55e-01
1800	4.86e-01	3.07e-01	3.03e-01	1.82e-01	2.00e-01	1.16e-01
1900	3.74e-01	2.27e-01	2.16e-01	1.39e-01	1.33e-01	9.18e-02
2000	2.62e-01	1.80e-01	1.55e-01	1.11e-01	1.02e-01	7.56e-02
2100	1.79e-01	1.50e-01	1.05e-01	9.49e-02	6.82e-02	6.43e-02
2200	1.28e-01	1.29e-01	7.53e-02	8.24e-02	5.10e-02	5.57e-02
2300	9.51e-02	1.13e-01	5.43e-02	7.21e-02	3.36e-02	4.82e-02
2400	6.31e-02	9.80e-02	3.79e-02	6.23e-02	2.44e-02	4.20e-02
2500	5.18e-02	8.48e-02	3.51e-02	5.41e-02	2.54e-02	3.60e-02
2600	5.69e-02	7.25e-02	4.02e-02	4.63e-02	3.02e-02	3.10e-02
2700	6.32e-02	6.15e-02	4.41e-02	3.96e-02	3.25e-02	2.67e-02
2800	6.47e-02	5.25e-02	4.33e-02	3.39e-02	3.11e-02	2.29e-02
2900	5.87e-02	4.47e-02	3.78e-02	2.90e-02	2.71e-02	1.96e-02
3000	4.82e-02	3.84e-02	2.88e-02	2.51e-02	1.87e-02	1.71e-02

Table 6.4: Observed and Expected Upper Limits at 95% CL on $\sigma \times BR \times A$ for a gg resonance, a qg resonance, and qq resonance as a function of resonance mass with systematic uncertainties

Mass [GeV]	95 % Upper Limit [pb]					
	gg		qg		qq	
	Observed	Expected	Observed	Expected	Observed	Expected
3100	3.18e-02	3.33e-02	1.96e-02	2.20e-02	1.16e-02	1.51e-02
3200	2.57e-02	2.92e-02	1.92e-02	1.93e-02	1.65e-02	1.33e-02
3300	3.19e-02	2.57e-02	2.23e-02	1.71e-02	1.76e-02	1.19e-02
3400	3.25e-02	2.28e-02	2.21e-02	1.52e-02	1.68e-02	1.06e-02
3500	3.03e-02	2.02e-02	2.03e-02	1.36e-02	1.48e-02	9.52e-03
3600	2.56e-02	1.81e-02	1.66e-02	1.23e-02	1.05e-02	8.54e-03
3700	1.88e-02	1.63e-02	1.22e-02	1.11e-02	7.83e-03	7.67e-03
3800	1.46e-02	1.46e-02	9.56e-03	1.00e-02	6.43e-03	6.98e-03
3900	1.20e-02	1.32e-02	7.88e-03	9.03e-03	5.41e-03	6.30e-03
4000	1.01e-02	1.20e-02	6.63e-03	8.25e-03	4.57e-03	5.71e-03
4100	8.52e-03	1.09e-02	5.65e-03	7.47e-03	3.83e-03	5.22e-03
4200	7.23e-03	9.91e-03	4.79e-03	6.88e-03	3.17e-03	4.74e-03
4300	6.10e-03	8.94e-03	4.16e-03	6.20e-03	2.76e-03	4.25e-03
4400	5.39e-03	8.15e-03	3.99e-03	5.71e-03	2.99e-03	3.86e-03
4500	5.86e-03	7.37e-03	4.49e-03	5.22e-03	3.54e-03	3.47e-03
4600	6.63e-03	6.69e-03	4.91e-03	4.74e-03	3.73e-03	3.17e-03
4700	6.89e-03	6.10e-03	4.97e-03	4.25e-03	3.63e-03	2.88e-03
4800	6.64e-03	5.52e-03	4.69e-03	3.86e-03	3.34e-03	2.59e-03
4900	6.05e-03	4.93e-03	4.28e-03	3.56e-03	2.89e-03	2.39e-03
5000	5.30e-03	4.44e-03	3.73e-03	3.17e-03	2.43e-03	2.10e-03
5100	4.64e-03	4.15e-03	3.33e-03	2.88e-03	2.22e-03	1.90e-03
5200	4.29e-03	3.76e-03	3.11e-03	2.69e-03	2.06e-03	1.81e-03
5300	4.04e-03	3.47e-03	2.87e-03	2.39e-03	1.91e-03	1.61e-03
5400	3.70e-03	3.17e-03	2.55e-03	2.20e-03	1.66e-03	1.42e-03
5500	3.29e-03	2.88e-03	2.26e-03	2.00e-03	1.44e-03	1.32e-03
5600	2.81e-03	2.69e-03	1.91e-03	1.81e-03	1.18e-03	1.22e-03
5700	2.45e-03	2.49e-03	1.63e-03	1.71e-03	1.01e-03	1.12e-03
5800	2.10e-03	2.20e-03	1.44e-03	1.51e-03	9.02e-04	1.03e-03
5900	1.89e-03	2.10e-03	1.27e-03	1.42e-03	8.19e-04	9.28e-04
6000	1.74e-03	1.90e-03	1.16e-03	1.32e-03	7.52e-04	8.30e-04
6100	1.66e-03	1.81e-03	1.11e-03	1.22e-03	6.93e-04	7.32e-04
6200	1.59e-03	1.71e-03	1.02e-03	1.12e-03	6.14e-04	7.32e-04
6300	1.46e-03	1.61e-03	9.21e-04	1.03e-03	5.52e-04	6.35e-04
6400	1.36e-03	1.51e-03	8.45e-04	9.28e-04	4.89e-04	5.37e-04
6500	1.27e-03	1.42e-03	7.98e-04	9.28e-04	4.46e-04	5.37e-04
6600	1.23e-03	1.42e-03	7.49e-04	8.30e-04	4.41e-04	4.39e-04
6700	1.23e-03	1.32e-03	7.35e-04	8.30e-04	4.26e-04	4.39e-04
6800	1.23e-03	1.32e-03	7.19e-04	7.32e-04	3.84e-04	4.39e-04
6900	1.22e-03	1.22e-03	7.01e-04	7.32e-04	3.69e-04	3.42e-04
7000	1.21e-03	1.22e-03	7.07e-04	6.35e-04	3.82e-04	3.42e-04
7100	1.27e-03	1.22e-03	7.18e-04	6.35e-04	4.03e-04	3.42e-04
7200	1.42e-03	1.22e-03	7.66e-04	6.35e-04	3.88e-04	3.42e-04
7500	1.54e-03	1.22e-03	7.96e-04	6.35e-04	3.87e-04	2.44e-04
7600	1.66e-03	1.22e-03	8.24e-04	6.35e-04	3.76e-04	2.44e-04
7700	1.78e-03	1.22e-03	8.51e-04	6.35e-04	3.41e-04	2.44e-04
7800	1.93e-03	1.32e-03	8.75e-04	6.35e-04	3.52e-04	2.44e-04
7900	2.15e-03	1.42e-03	8.89e-04	6.35e-04	3.37e-04	2.44e-04

7. DIJET RESONANCE SEARCH WITH QUARK/GLUON JET TAGGING

7.1 Motivation

Distinguishing quark-initiated jets from the gluon-initiated jets is very useful for many physics analyses, and there has been growing interest in the means of separating quark jets from gluon jets because of significant jet production at LHC (Gallicchio and Schwartz, 2011). Many supersymmetric models produce quark jets with missing transverse energy such as gluino pair production which each gluino's cascade decay can produce four quarks and missing transverse momentum (Gallicchio and Schwartz, 2013). This process creates many jets from QCD as a background. These jets are predominately gluonic and being able to filter out background QCD events containing gluon jets would be helpful. Quark-gluon discrimination in the search for gluino pair production has been published (Bhattacharjee, 2016).

The quark/gluon jet discrimination would also be useful for some Standard Model studies. For instance, in vector boson fusion (VBF), the forward jets are always quark jets whereas, from non-electroweak backgrounds to VBF, the jets near the beams are often gluonic. In the Standard Model, as the P_T of jets goes up, or if they are produced along with an electroweak boson, the fraction becomes more quark-heavy. Thus, knowing the quark-to-gluon jet fraction of an event can help determine what the underlying hard partons are with applications in the standard model.

The quark/gluon jet discrimination will be very useful for dijet resonances search that decaying to two partons as final jets, such as quark-quark, gluon-gluon, quark-gluon. Besides, categorizing of dijet mass distribution using quark/gluon jet tagging allow searching for particular parton pairs final states (qq, qg, gg). If the signal appears in the dijet mass distribution as a bump, quark/gluon jet tagging of the signal may help us to understand the theoretical origin of the signal. This classification may also significantly improve the signal sensitivity for dijet resonances.

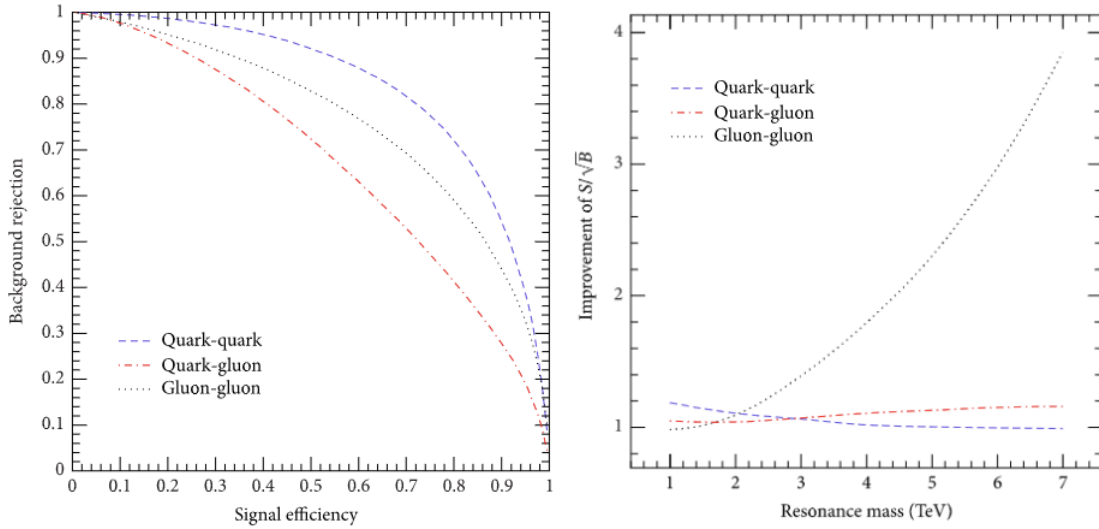


Figure 7.1: Left: ROC curves of each type of parton pairs. The greatest background rejection is achieved for quark-quark parton pair tagging. Right: Improvement of signal significance ratio as a function of resonance mass after applying parton tagging. The tagging discriminator is chosen at 80% signal efficiency

Figure 7.1 shows the separation of parton pairs to search for the effect on dijet resonance search. In order to get the best background rejection in a given signal efficiency point for each type of signal resonances (qq, qg, and gg), the receiver operation characteristics (ROC) curves are plotted from a Monte Carlo simulation. On the right of Figure 7.1 are shown quark-quark parton pairs to give the best background rejection as a function of signal efficiency. On the left of Figure 7.1 are shown improvement of signal significance ratio as a function of resonance mass after applying parton tagging with an 80% signal efficiency (Ozturk,2014).

In this section, we will discuss the separation of quark-initiated jet from the gluon-initiated jet, and the effect on the dijet resonance search. The result of the tagging method on dijet resonance search and comparison of the standard resonance search will subsequently be discussed.

7.2 Quark/Gluon Jet Discrimination in CMS

To separate initiated-quark jets from the initiated-gluon jets is possible because of differences between quarks and gluons (Alexander, 1996). Most work has been based on jet properties that result from the difference in color charge between the partons. The color factors in quantum chromodynamics for quarks $C_F = 4/3$ and gluons $C_A = 3$ and so this lead to, approximately $C_A/C_F = 9/4$ times more particles in a gluon-initiated jets than in a quark-initiated jets (Larkoski, 2014).

These differences show discrepancy on an observable jet variable which allows us to separate quark jets from gluon jets on statistical basis. Using several jet variables at the same time can improve tagging results. A likelihood distribution can be obtain with these jet variables, which shows them as quark jets or gluon jets. In this analysis, likelihood discriminant is used to separate quark jets from gluon jets.

7.2.1 A likelihood discriminant

The likelihood discriminant is developed as a product of the three variables multiplicity, $axis_2$, and P_{TD} . This approach guarantee simplicity, transparency, and robustness (Marini, 2013). These variables are chosen after their discriminant power have been studied according to their receiver operation characteristics (ROC) regarding quark efficiency vs. the gluon rejection. The most significant background rejection is obtained by quark-quark parton pair and quark-gluon parton pair is the most challenging parton pair type to distinguish compare to other parton pair types according to ROC curves of each parton pairs (Ozturk,2014).

Once the probability distributions of these three variables are obtained, the likelihood discriminant can be defined. The probability density function for gluon ($G(\vec{x})$) and the probability density function for quark ($Q(\vec{x})$), defining as the product of each variables probability density function (f^i), computed at given variable's value $x([i])$:

$$G(\vec{x}) = \prod_i f_G^i(x[i]) \quad Q(\vec{x}) = \prod_i f_Q^i(x[i]) \quad (7.1)$$

so that a likelihood estimator can be defined as:

$$L(\vec{x}) = \frac{Q(\vec{x})}{Q(\vec{x}) + G(\vec{x})} \quad (7.2)$$

Multiplicity

Multiplicity is the total number of particle flow candidates reconstructed within the jet. The ratio of multiplicity for quark and gluon jets comes from the color factor in quantum chromodynamics which has different values for quarks ($C_F = 4/3$) and gluons ($C_A = 3$) so that more particles are obtained in gluon-initiated jets than in quark-initiated jets (Acton, 1993).

Gluon jets are expected to have a higher value of multiplicities as compared with quark jets because of color ratio. A difference of multiplicity of light quark and gluons are shown in Figure 7.2 on top left.

Axis₂

Minor axis (σ_2) measures the angular spread of the jet in the $\eta - \phi$ plane. For equal energy, the axis should be narrower in quark jets than gluon jets due to the mean transverse energy value of the particles which is expected around the same (Marini, 2013). Therefore, gluon jets are spread over a large angular gap than quark jets. The angular distribution of quark and gluon shows in the Figure 7.2 on bottom.

$P_T D$

Transverse momentum distribution among the PF candidates is defined as (Cornelis, 2014) :

$$P_T D = \frac{\sqrt{\sum P_T^2}}{\sum P_T^2} \quad (7.3)$$

where the sums are extended over all candidates within the PF jets.

$P_T D$ variable is a measure how asymmetrically the transverse momentum of a given jets is distributed among its constituents. From its definition, $P_T D \rightarrow 1$ means that jets consisting of only one particle carries all of its momentum, and $P_T D \rightarrow 0$ means jets consist of an infinite number of particles. That way, quark jets are expected to hadronize more asymmetrically within its constitutes respect to the gluon jets because of this $P_T D$ value closer the unity. $P_T D$ distribution is showed in Figure 7.2 on top right.

7.3 Q/G Jet Tagging Discriminator Optimization

Our analysis strategy is the same as standard dijet search, so the same event selection process is used in this analysis. The Table 7.1 is a summary of the event selection for the quark/gluon jet tagging search. The q/g jet tagging is applied to two leading jets once all the main analysis selections are applied.

Table 7.1: The events selection summary for quark/gluon jet tagging search

Jet Type	Particle Flow (PF) Jet
Jet Algorithm	anti- k_T , $R = 0.4$
$\Delta R = \sqrt{\Delta\phi^2 + \Delta\eta^2}$	< 1.1
Jet Identification	Tight Jet ID
$ \eta $	< 2.5 (central region)
Transverse Momentum (P_T)	$P_{T_1} > 60 \text{ GeV}$, $P_{T_2} > 30 \text{ GeV}$
$ \Delta\eta_{jj}^{\text{Wide}} = \eta_1 - \eta_2 $	< 1.3

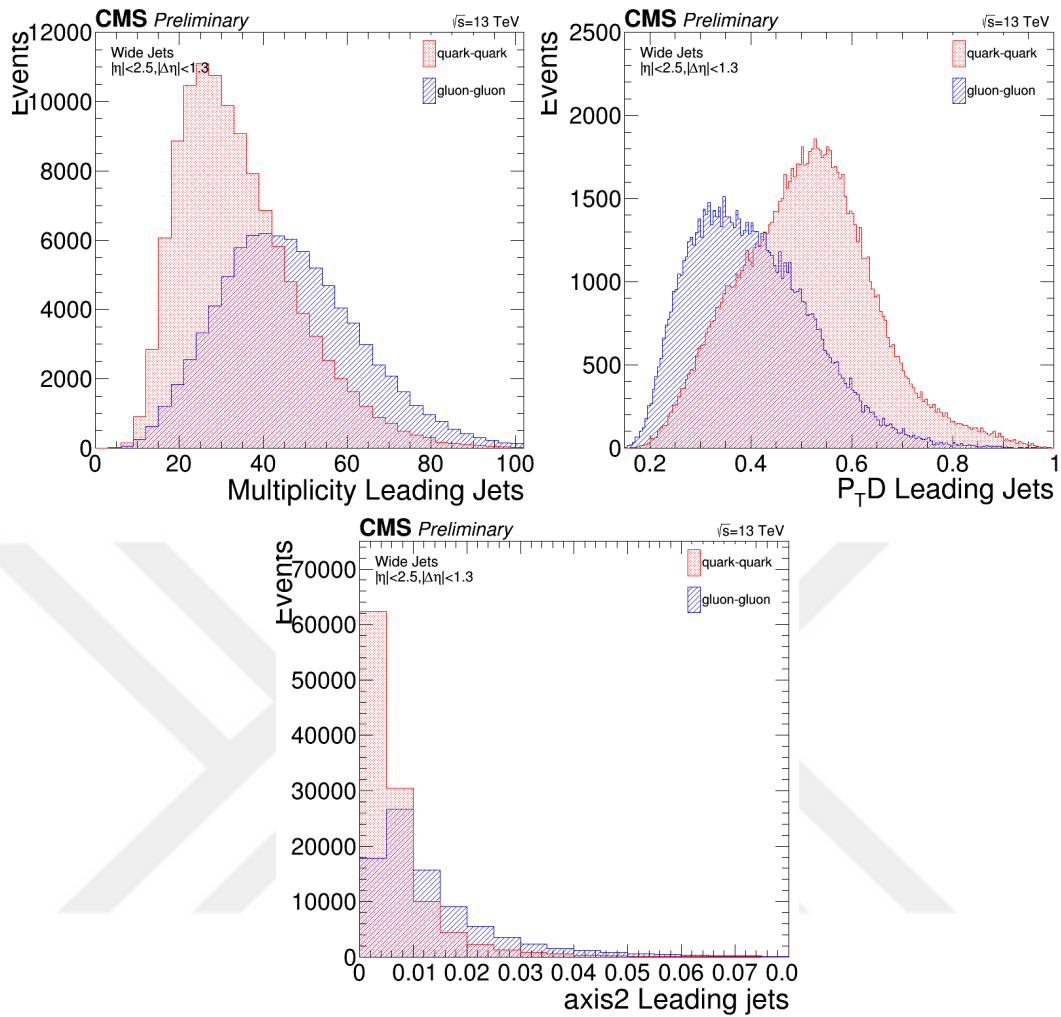


Figure 7.2: Normalized distributions of the discriminant variables, for quark (red) and gluon (blue) jets at 4 GeV reconstructed jet with $|\eta| < 2.5$. Total multiplicity (top left), $P_T D$ (top right), $axis_2$ (bottom).

Figure 7.3 shows the likelihood distribution for quark and gluon jets, on that plot quarks peak at 1, and gluons peak at 0. With a selection of q/g likelihood discriminant (LD) operation point on this plot, quark-heavy events, or gluon-heavy events can be determined. The selected q/g LD operation point may give an improvement of significance depending on the selection. The leading jets can be chosen smaller or bigger than this LD operation point, which provides quark-heavy events or gluon-heavy events on the statistic sense. If two leading jets are chosen bigger than the LD operation point, we denote as 0g-tag because it is a quark heavy event. Similarly, if two leading jets are chosen smaller than LD operation point, we denote as 2g-tag event, and one leading jet is chosen bigger than

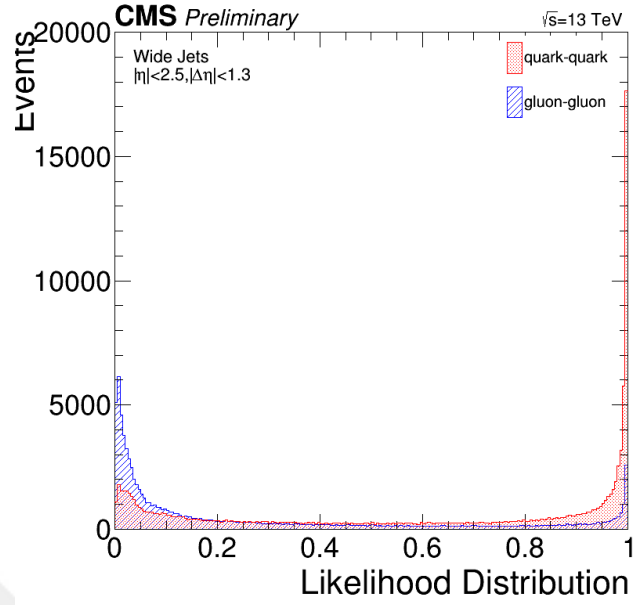


Figure 7.3: Normalized distributions of the likelihood quark/gluon discriminant for quark (red) and gluon (blue) at 4 GeV reconstructed jet with $|\eta| < 2.5$

LD operation point, then the other one is chosen smaller than LD operation point, we denote as 1g-tag. The Table 7.2 shows the selection of q/g jet tagging for this search.

Table 7.2: The q/g jet tagging application strategy. Figure 7.3 shows LD operation points which we choose the apply and Figure 7.4 shows the optimal LD operation point as 0.5.

2g-tag	$(Jet_1 > 0.5 \ \& \ Jet_2 > 0.5)$
1g-tag	$(Jet_1 > 0.5 \ \& \ Jet_2 < 0.5) \ \ (Jet_1 < 0.5 \ \& \ Jet_2 > 0.5)$
0g-tag	$(Jet_1 < 0.5 \ \& \ Jet_2 < 0.5)$

Significance must improve with q/g jet tagging for contributing to dijet resonance search. For this purpose, optimal q/g LD operation point should be determined for this analysis. Calculating the improvement of significance, S/\sqrt{B} which is obtained with q/g jet tagging divided to S/\sqrt{B} which is obtained from standard dijet resonance search.

$$Improvement \ of \ Significance = \frac{S_{q/g \ tag} / \sqrt{B_{q/g \ tag}}}{S / \sqrt{B}} \quad (7.4)$$

Improvement of significance for q/g jet tagging is performed for three type of parton pairs (qq, qg, gg). On the top left of Figure 7.4 shows the gluon-gluon parton pair with a 2g-tag method, on the top right of Figure 7.4 shows the quark-quark parton pair with a 0g-tag method and on the bottom of Figure 7.4 shows the quark-gluon parton pair with a 1g-tag method. Improvement of signal significance for quark-quark resonance and quark-gluon resonance is not improved significantly, but there is a remarkable result for gluon-gluon resonance signal sample. The optimal operation point from those plots point out the around 0.5 (both leading jets) for three type of parton pairs.

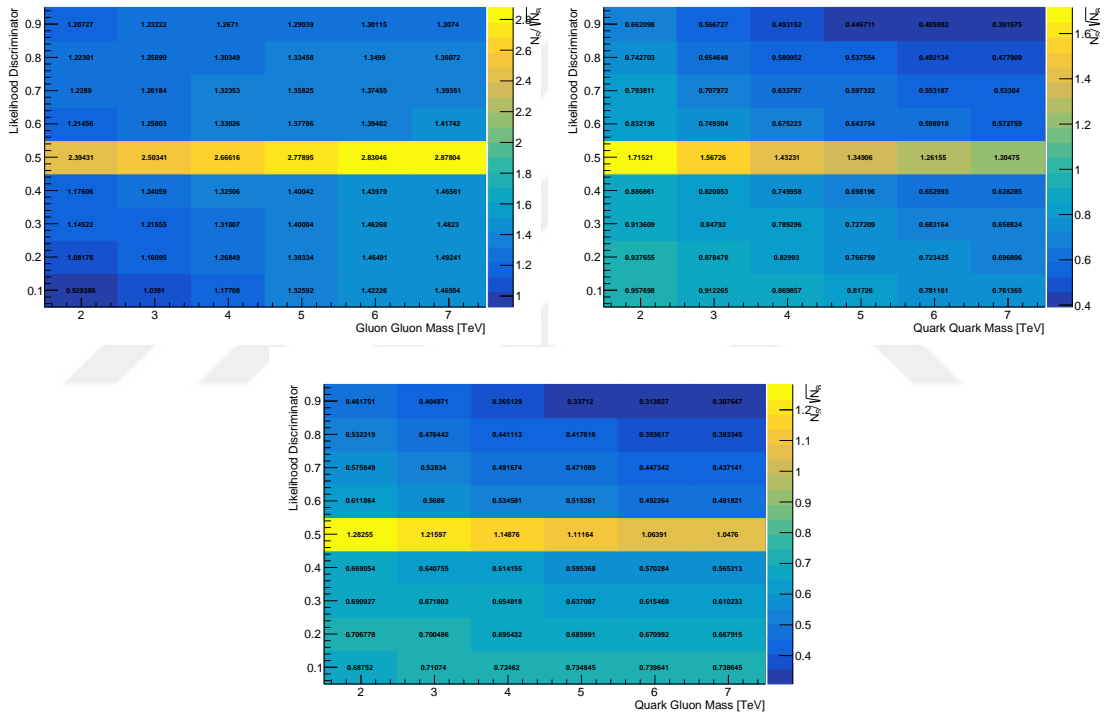


Figure 7.4: Improvement on signal significance for the gluon-gluon parton pair with a 2g-tag method (top left), the quark-quark parton pair with a 0g-tag method (top right), and the quark-gluon parton pair with a 1g-tag method (bottom).

7.4 Dijet Mass Measurement with Quark/Gluon Jet Tagging

In this section, analysis strategy summarised for q/g jet tagging search. As we mentioned in Section 7.3, the same analysis strategy used for q/g jet tagging method. The data, QCD MC simulation, and the signal models are the same as standard dijet search,

and you may find more information in Section 5.1. Besides, the detailed events selection strategy may find in Section 5.2. Even if we have the same approach, we still need the check trigger efficiency and data quality after applying the q/g jet tagging to see there is not any effect on the search. In the same perspective, we should also check the signal modeling. After, these checks we can proceed the generate dijet mass spectrum and then calculate the upper limits with this new approach to see the effect on dijet search.

7.4.1 Trigger efficiency

The following triggers PFHT800, PFHT900, PFJet500, CaloJet500_NoJetID, and DiPFJetAve500 are used for the trigger efficiency with respect to the singleMuon45 trigger to find the efficient dijet mass for quark/gluon jet tagging. We used the mentioned triggers for utilizing a 2g-tag, 1g-tag, and 0g-tag method. All considered methods showed the same mass point as the standard dijet resonance search that found 98 % efficiency on 1246 GeV. Figure 7.5 shows trigger efficiency for q/g jet tagged dijet events.

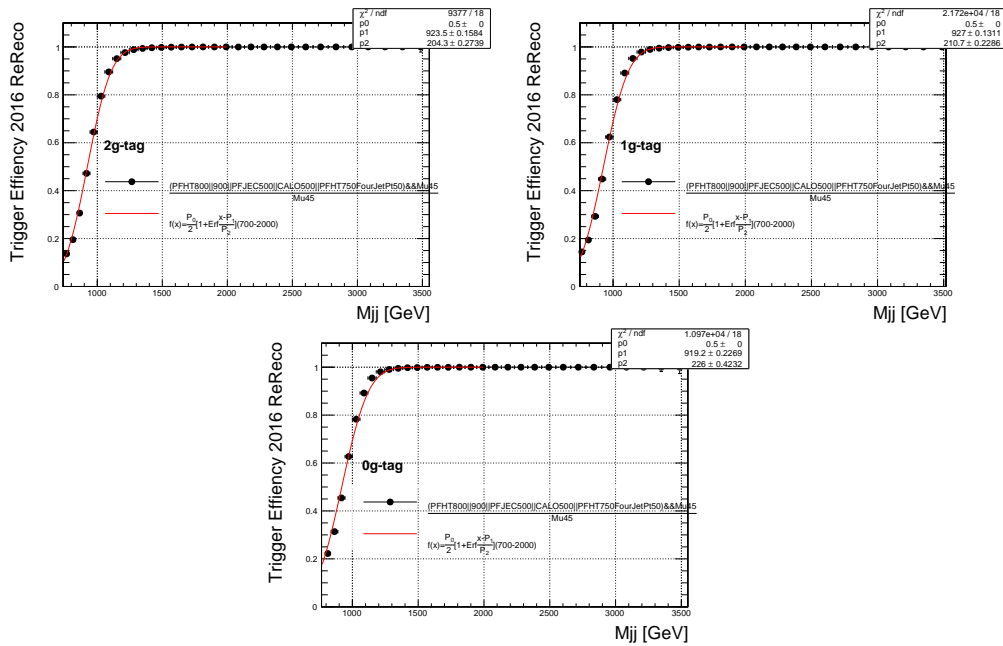


Figure 7.5: The measurement of trigger efficiency for quark/gluon tagged dijet events versus m_{jj} , 2g-tag (top left), 1g-tag (top right) and 0g-tag (bottom).

7.4.2 Data quality

In this section, quality of inclusive dijet data for a 2g-tag, 1g-tag, and 0g-tag has been performed. For this, the data sample is compared to the MC simulation events, which are normalized to the number of data entries. The normalization factor shifted according to the q/g jet tagging method which are the 2g-tag, 1g-tag, and 0g-tag corresponding scale factors are 0.65, 1.03, and 0.81, respectively.

Firstly, the dijet mass spectrum is evaluated with a comparison of MC simulation and the data. The dijet mass spectrum is in good agreement with a comparison of MC simulation and the data for three type of tagging method. The highest mass event is equal to $m_{jj}^{wide} = 7.8$ TeV for a 1g-tag, $m_{jj}^{wide} = 7.6$ TeV for a 2g-tag, and $m_{jj}^{wide} = 7.3$ TeV for a 0g-tag. Figure 7.6 shows the comparison between data and MC simulation for a 2g-tag, 1g-tag, and 0g-tag.

We study the data quality of kinematic quantities which are P_T , η , and ϕ . The angle of the two leading jets in the transverse plane, $|\Delta\phi|$ and the absolute difference in pseudorapidity between two leading wide jets, $|\Delta\eta|$ are also investigated. These data quality check is produced for three type of q/g jet tagging method separately.

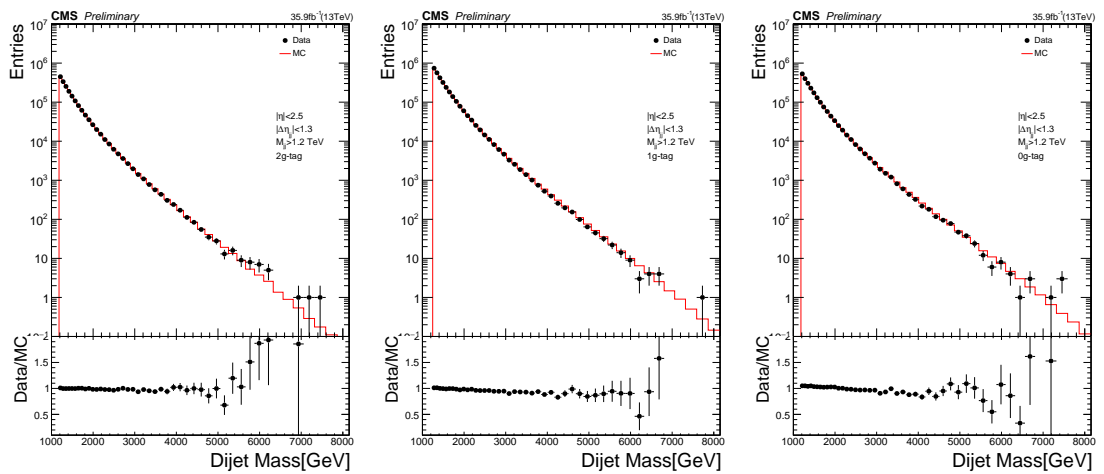


Figure 7.6: The dijet mass distribution with the data (point) and MC simulation (continuous histogram) events for 2g-tag method (left), 1g-tag method (middle), and 0g-tag method (right) along with data/MC ratio on bottom plots.

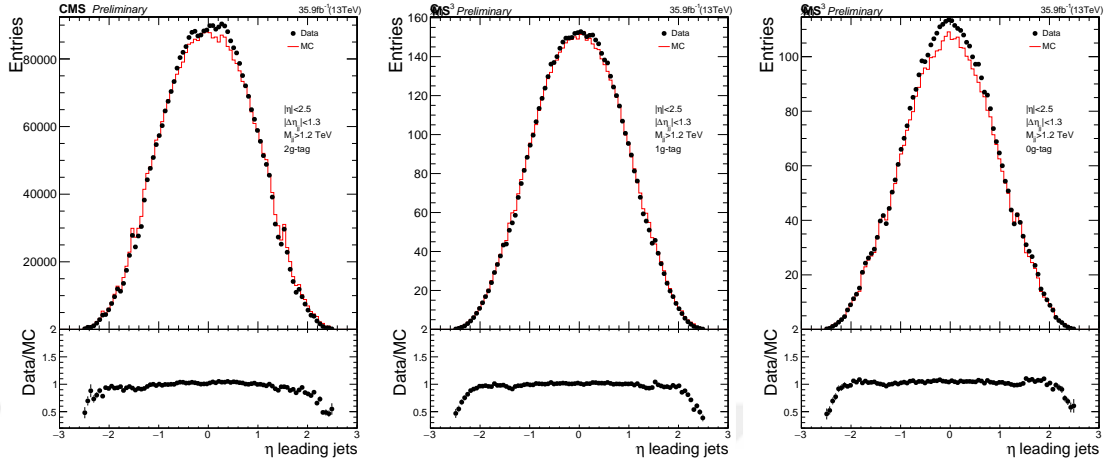


Figure 7.7: The η distribution of two leading wide-jets with the data (point) and MC simulation (continuous histogram) events for 2g-tag method (left), 1g-tag method (middle), and 0g-tag method (right) along with data/MC ratio on bottom plots.

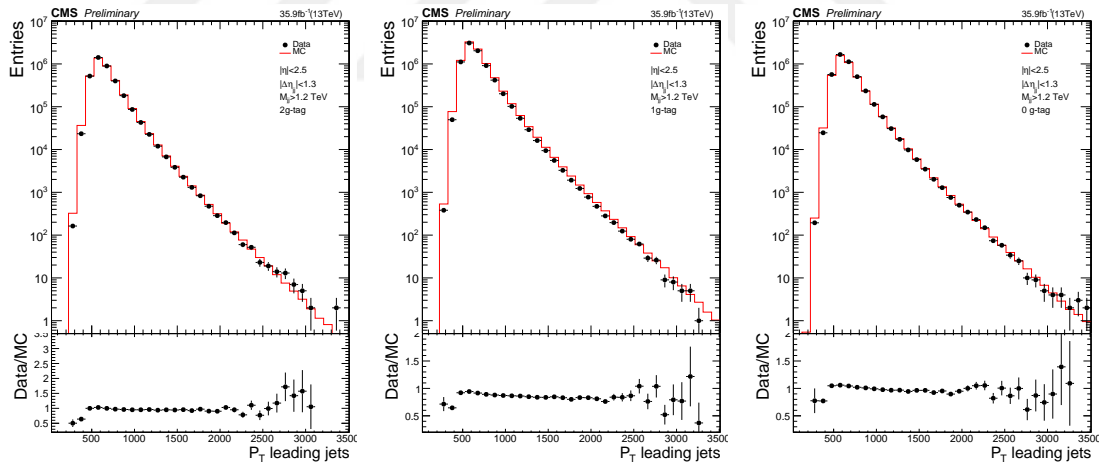


Figure 7.8: The p_T distribution of two leading wide-jets with the data (point) and MC simulation (continuous histogram) events for 2g-tag method (left), 1g-tag method (middle), and 0g-tag method (right) along with data/MC ratio on bottom plots.

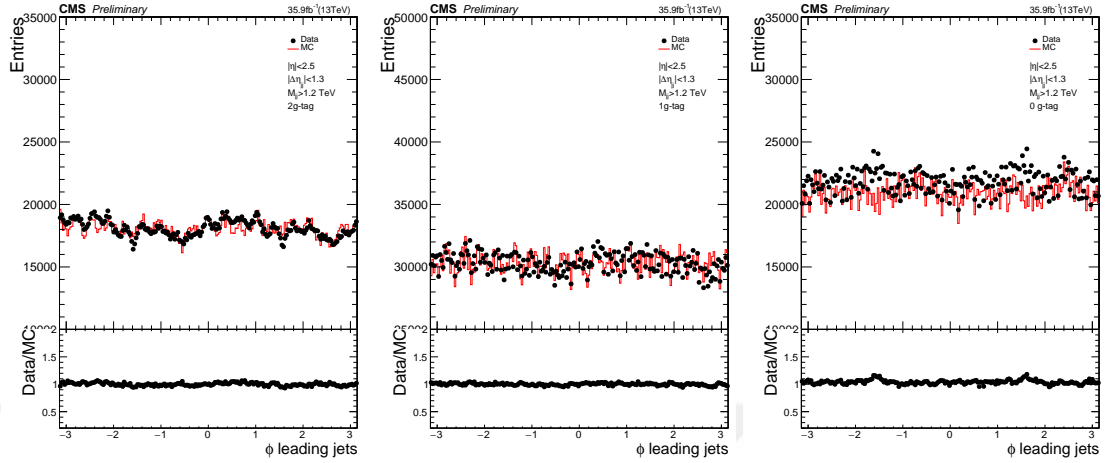


Figure 7.9: The ϕ distribution of two leading wide-jets for 2g-tag (left), 1g-tag (middle), and 0g-tag (right)

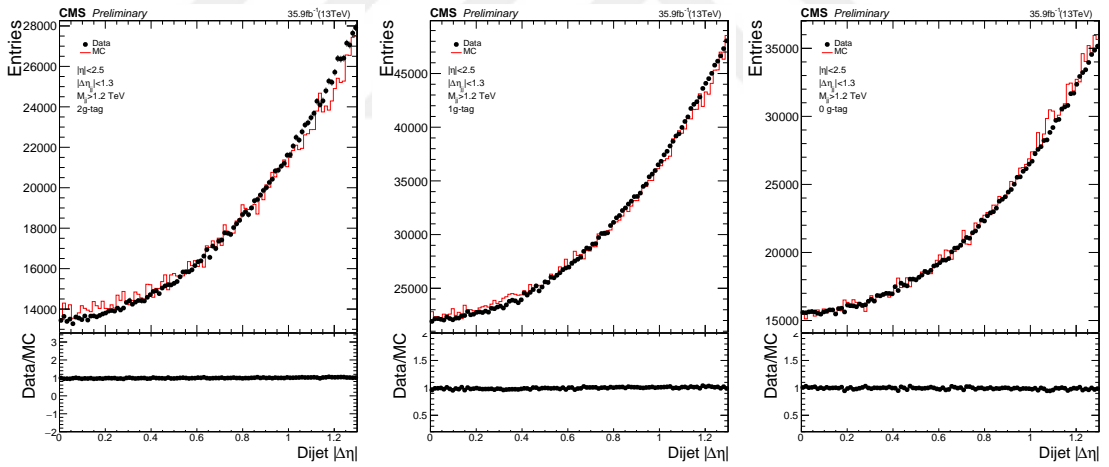


Figure 7.10: The $\Delta\eta$ distribution of two leading wide-jets with the data (point) and MC simulation (continuous histogram) events for 2g-tag method (left), 1g-tag method (middle), and 0g-tag method (right) along with data/MC ratio on bottom plots.

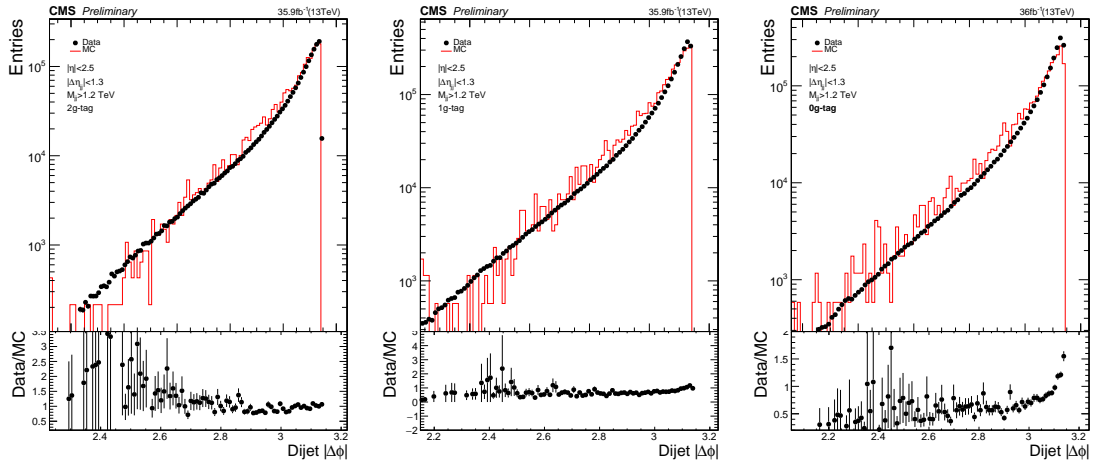


Figure 7.11: The $\Delta\phi$ distribution of two leading wide-jets with the data (point) and MC simulation (continuous histogram) events for 2g-tag method (left), 1g-tag method (middle), and 0g-tag method (right) along with data/MC ratio on bottom plots.

7.4.3 Impact of q/g jet tagging on signal modeling

The signal model can be affected in two ways using the q/g jet tagging. First, it may increase the signal efficiency, and secondly, it may change the shape of the dijet resonance. Figure 7.12 shows the gluon-gluon, quark-gluon, and quark-quark resonance samples for a resonance masses at 1 TeV, 3 TeV, 5 TeV, and 7 TeV with a comparison of the standard signal shape to the q/g jet tagged signal shape with a LD operation points of 0.2, 0.5 and 0.8. On top left of Figure 7.12 shows a comparison of the standard gg signal shape to the 2g-tagged gg signal shapes. On top right of Figure 7.12 shows a comparison of the standard qq signal shape to the 1g-tagged qq signal shapes. On bottom of Figure 7.12 shows the comparison of the standard qq signal shape to the 0g-tagged qq signal shapes. Comparing these signal shapes without and with q/g tagging method is in good agreement. The method of q/g jet tagging does not noticeably affect the signal resonance shapes.

Another impact of q/g jet tagging on signal modeling is the effect of the signal efficiency. The efficiency of considered parton pair types as a function of resonance mass for three parton pair types is shown in Figure 7.13. The signal efficiency is greater

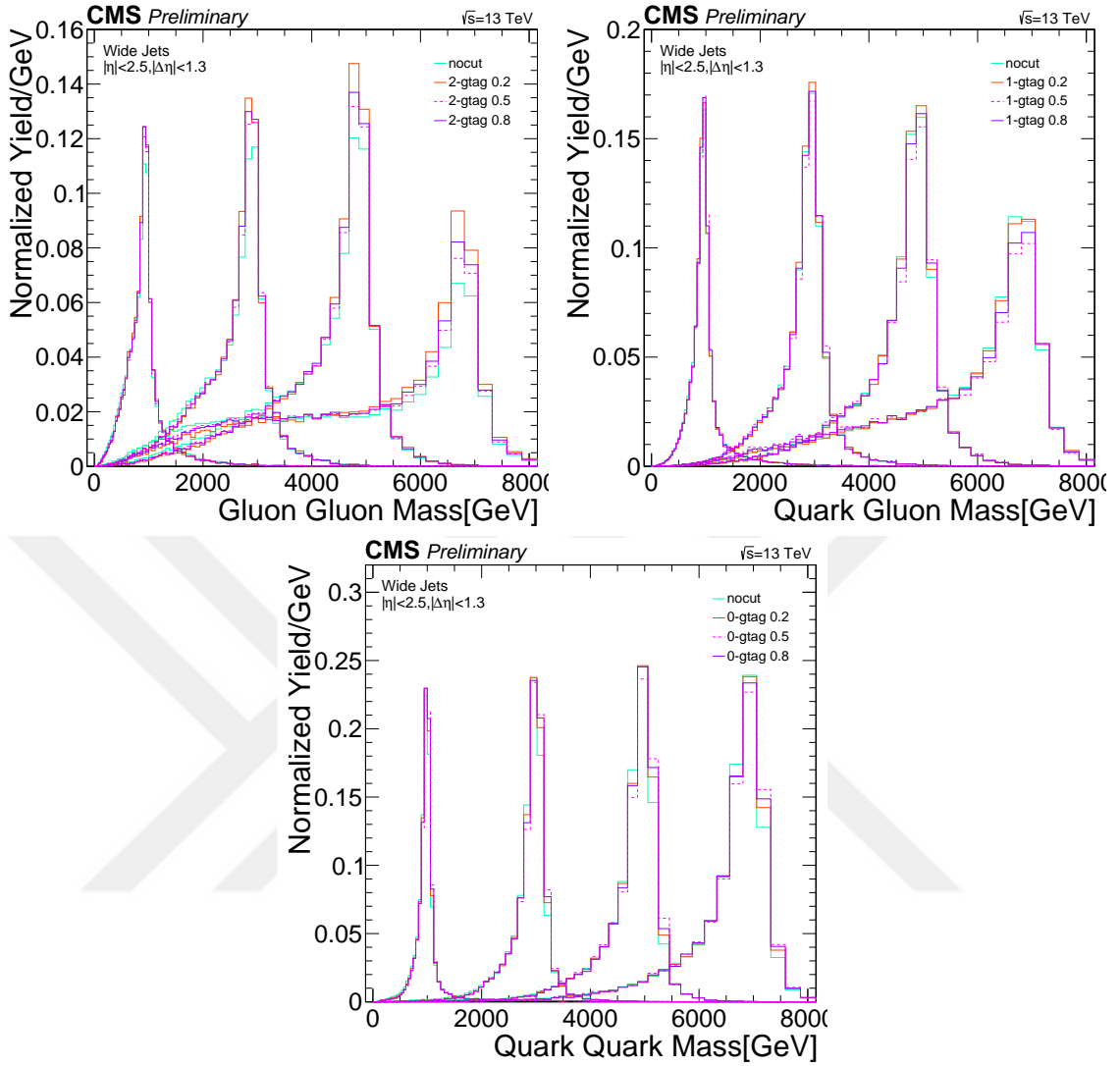


Figure 7.12: Resonance shapes with q/g tag on considered parton pair types for resonance mass 1, 3, 5, 7 TeV with different q/g tag operation point, $G \rightarrow gg$ resonance sample with 2g tag (top left), $q^* \rightarrow qg$ resonance sample with 1g tag (top right), and $G \rightarrow qq$ resonance sample with 0g tag, (bottom).

than 50% for gluon-gluon resonance mass on the top left plot, and there is no significant improvement for quark-quark and quark-gluon resonances.

7.4.4 Dijet mass spectrum and fit

The dijet mass spectrum is measured separately for a 2g-tag, 1g-tag, and 0g-tag methods. The black points represent the data and is calculated from a differential cross

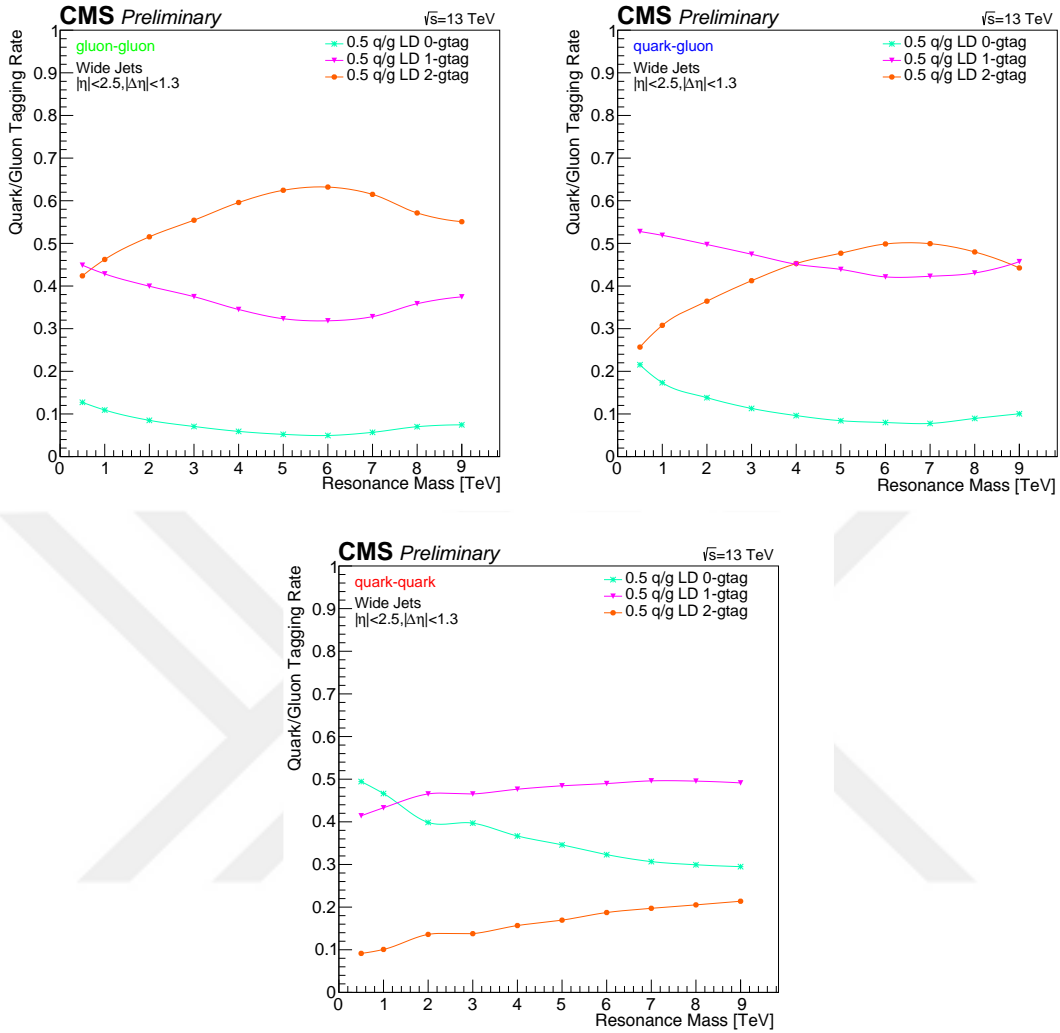


Figure 7.13: Tagging Rate as a function of resonance mass using 0.5 LD operation point for gluon-gluon resonance sample (top left), quark-gluon resonance sample (top right), and quark-quark resonance sample (bottom).

section given by: $\frac{d\sigma}{dm} = \frac{1}{\int L dt} \frac{N_i}{\Delta m_i}$, where m is the dijet mass, N_i is the number of events in the i^{th} dijet mass bin, and Δm_i is the width of the i^{th} dijet mass bin, and the integrated luminosity is $\int L dt$. The estimation of background for this analysis is obtained directly from the data, which is fitted with a 4-parameter function given by: $\frac{d\sigma}{dm} = \frac{P_0(1-X)^{P_1}}{X^{P_2+P_3 \ln(x)}}$, where $X = M_{jj}^{Wide}/\sqrt{s}$, $\sqrt{s} = 13$ TeV and $P_{0,1,2,3}$ are free parameters. You may find more information in Section 5.5.

Figure 7.14 shows the binned fit for a 2g-tag, 1g-tag, and 0g-tag method. We did not observe any resonance structures in the measured dijet mass spectra for these three type of q/g jet tagging method.

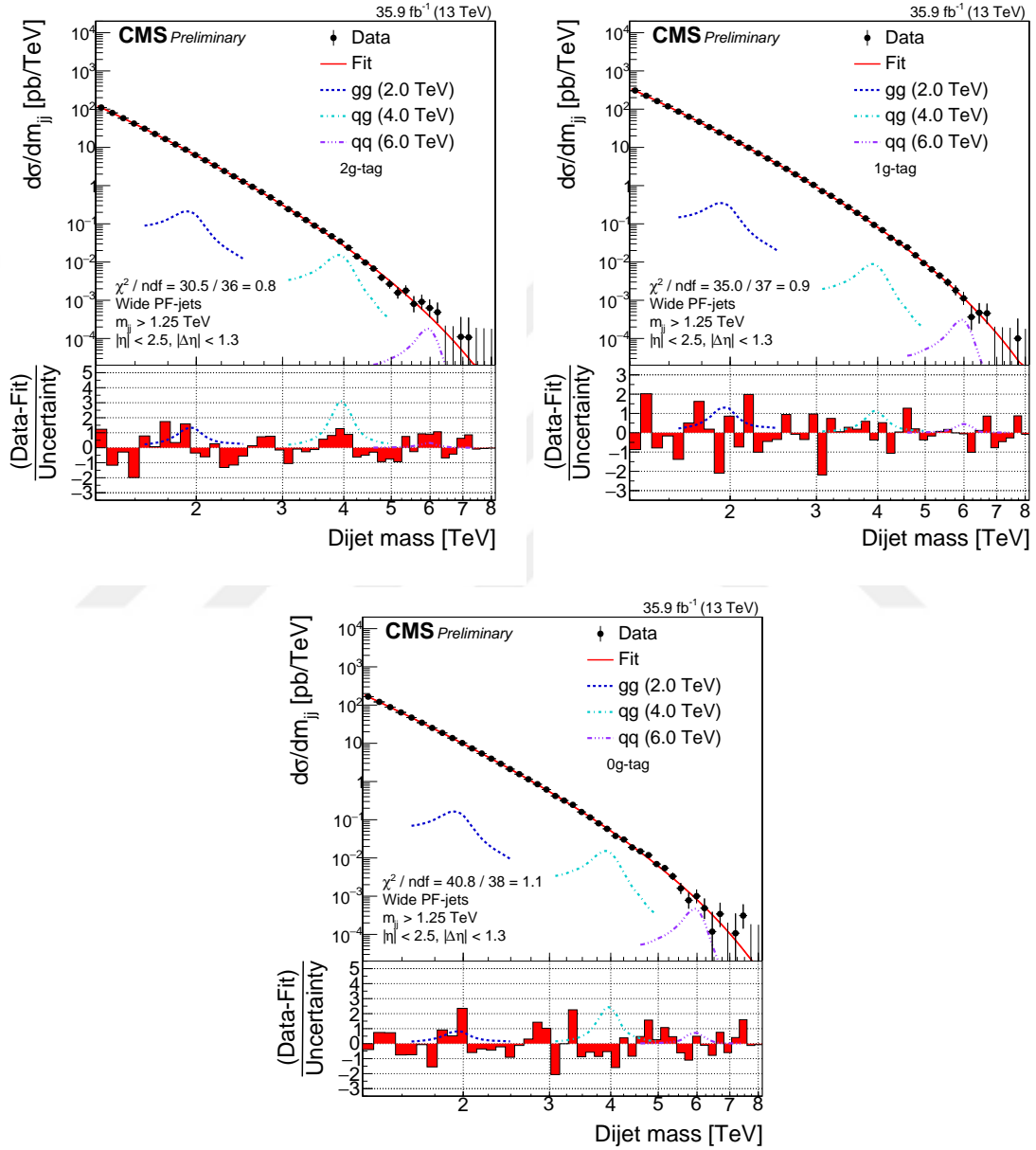


Figure 7.14: The binned fit shown for 2g-tag (top left), 1g-tag (top right), and 0g-tag (down). The signal shapes normalized the cross section for each resonance type at that mass and scaled the quark gluon tagging rate for each tagging method.

7.4.5 Setting of cross section upper limits

We perform the q/g jet tagging search with total integrated luminosity 35.9 fb^{-1} . But, we did not observe any significant excess. We proceed to set upper mass limits for qq, qg and gg resonance sample with 100 GeV step. We used the same methodology as the calculation of standard cross-section upper limits. As mentioned in Section 6.3 we used

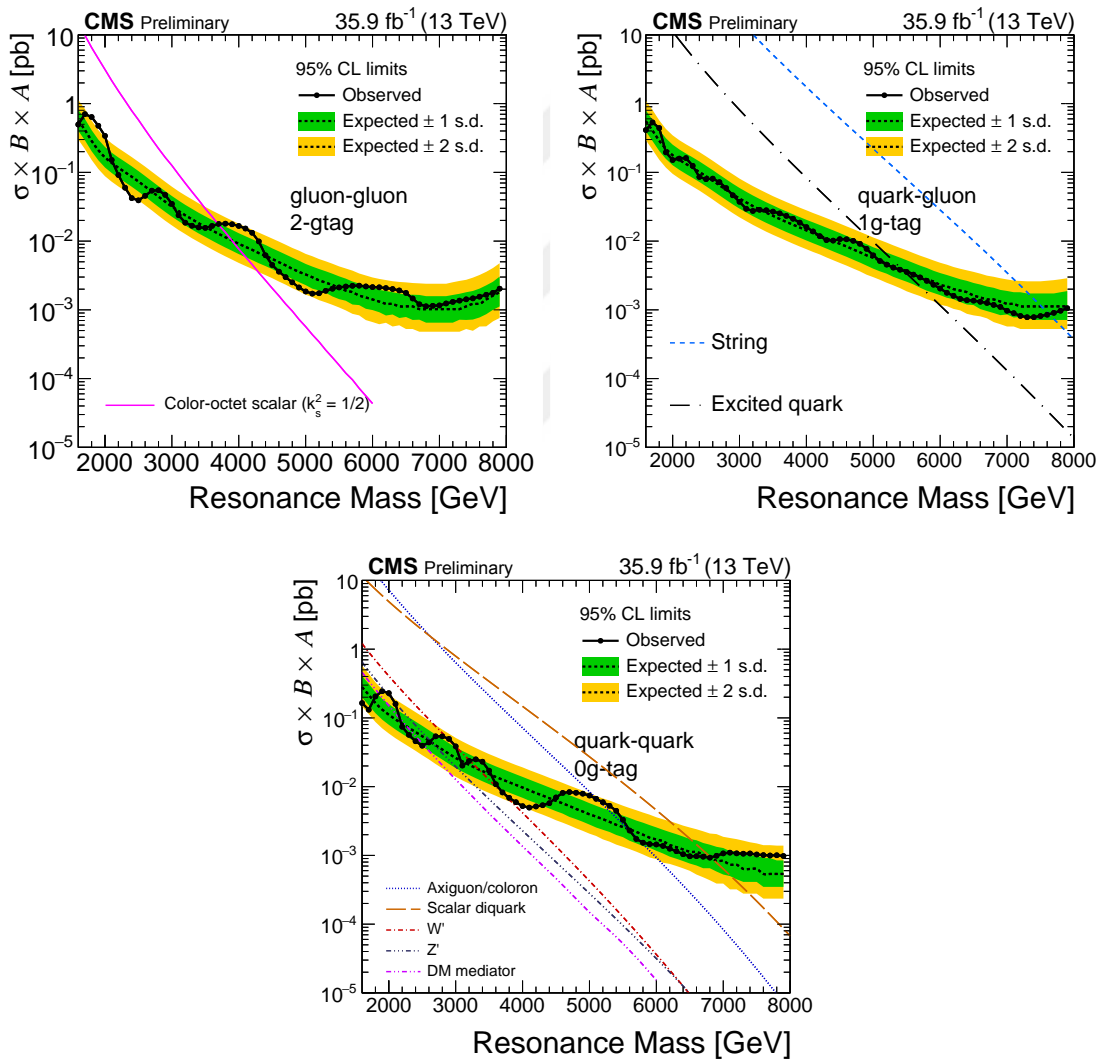


Figure 7.15: 95% CL upper limits on cross section times ratio times acceptance ($\sigma \times BR \times A$) for gluon-gluon resonance with 2g-tag method (top left), quark-gluon resonance with 1g-tag method (top right), and quark-quark resonance with 0g-tag method (bottom) with systematic uncertainties.

the interpolated signal sample to calculate the limits for every 100 GeV. But in this search, we applied the q/g tagging rate to the interpolated signal sample. Figure 7.15 shows the cross-section upper limits with systematic uncertainties for q/g jet tagging.

Figure 7.16 shows the comparison of upper mass limit for standard dijet search and q/g jet tagging for gg, qg and, qq resonance signal utilizing 0.5 LD operation point. The 2g-tag method is used for the gluon-gluon signal sample, which is shown on the top left

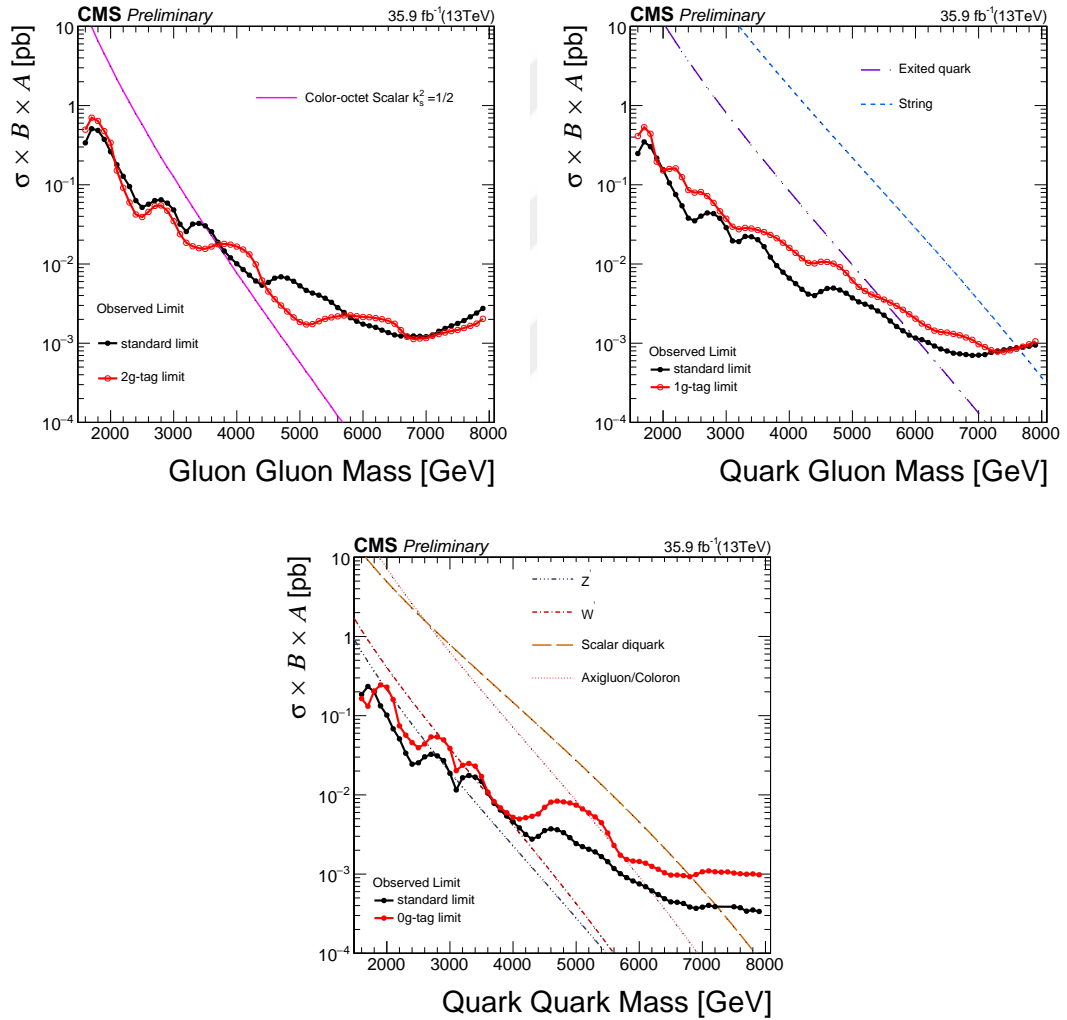


Figure 7.16: The comparison of standard dijet searches (black point) to the q/g jet tagging (red point) for gluon-gluon resonance using 2g-tag method (top-left), quark-gluon resonance using 1g-tag method (top-right) and, quark-quark resonance using 0g-tag method (bottom).

of Figure 7.16. As we expect, the better limits are obtained for some masses compared to the standard dijet resonance search. In this search, the only resonance model decaying to gluon-gluon is the color-octet-scalar. Standard dijet resonance search set the upper mass limit on the color-octet-scalar above 3.4 TeV. But, the upper mass limit with q/g jet tagging on color-octet-scalar models at above 3.7 TeV. As a result, we obtained a better upper mass limit for the color-octet-scalar when applying the quark/gluon jet tagging method. For the quark-gluon and the quark-quark sample, we didn't obtain any remarkable results.



8. CONCLUSION

In conclusion, we have performed a search of narrow resonances decaying into a pair of jets at $\sqrt{s} = 13$ TeV using proton-proton collisions data, corresponding to an integrated luminosity of 35.9 fb^{-1} . Results are reported for two searches: A standard dijet resonance mass measurement and quark/gluon jet tagging method applied to the dijet resonance mass measurement. Both searches use the same analysis strategy.

The dijet mass spectrum measurement with mass above 1.2 TeV is performed using particle flow jets. These PF jets are reconstructed with an anti- k_T clustering algorithm. The pseudorapidity separation of the two jets is required to satisfy $|\Delta\eta| < 1.3$ with each jet expected inside the region $|\eta| < 2.5$. The dijet mass distribution is fitted with a smooth fit function, and no significant excess is observed. Then, upper limits at 95% CL are obtained on $\sigma \times BR \times A$ for gluon-gluon, quark-gluon, and quark-quark final states. The limits are interpreted within the of specific models using the standard dijet search. String resonances are excluded for masses below 7.6 TeV, scalar diquarks below 7.2 TeV, axigluons and colorons below 6.1 TeV, excited quarks below 6.0 TeV, color-octet scalars below 3.4 TeV, W' bosons below 3.3 TeV, Z' bosons below 2.7 TeV, and RS gravitons below 1.7 TeV, extending previously published limits in the dijet channel.

Table 8.1: Observed and expected mass limits at 95% CL from this analysis with 35.9 fb^{-1} at $\sqrt{s} = 13$ TeV compared to previously published limits on narrow resonances from CMS with 12.9 fb^{-1} and 2.4 fb^{-1} at $\sqrt{s} = 13$ TeV and with 20 fb^{-1} at $\sqrt{s} = 8$ TeV.

Model	Final State	Observed (Expected) mass limit [TeV]			
		35.9 fb^{-1} 13 TeV	12.9 fb^{-1} 13 TeV	2.4 fb^{-1} 13 TeV	20 fb^{-1} 8 TeV
String	qg	7.6 (7.7)	7.4 (7.4)	7.0 (6.9)	5.0 (4.9)
Scalar diquark	qq	7.2 (7.4)	6.9 (6.8)	6.0 (6.1)	4.7 (4.4)
Axigluon/Coloron	$q\bar{q}$	6.1 (6.0)	5.5 (5.6)	5.1 (5.1)	3.7 (3.9)
Exited quark	qg	6.0 (5.8)	5.4 (5.4)	5.0 (4.8)	3.5 (3.7)
Color-octet-scalar($k_s^2=1/2$)	gg	3.4 (3.6)	3.0 (3.3)	—	—
W'	$q\bar{q}$	3.3 (3.6)	2.7 (3.1)	2.6 (2.3)	2.2 (2.2)
Z'	$q\bar{q}$	2.7 (2.9)	2.1 (2.3)	—	1.7(1.8)
RS Graviton	$q\bar{q}, \text{gg}$	1.7 (2.1)	1.9 (1.8)	—	1.6 (1.3)

Table 8.1 shows observed and expected mass limits at 95% CL from this analysis compared to previously published limits on narrow resonances from CMS. As we expect, limits have improved thanks to increased statistics.

Quark/gluon jet tagging has been applied to the two highest P_T jets to reconstruct the dijet mass separately for each parton pair type. We use the likelihood method to separate the quark jets from gluon jets in statistical basis. The q/g likelihood plot has an output between 0 and 1. In this plot, an optimal operation point of 0.5 has been set to get better significance for specific parton pair type. A 2g-tag method is used for gluon-gluon signal samples, 1g-tag method is used for quark-gluon signal samples, and 0g-tag method is used for quark-quark signal sample. As a result, the better upper mass limits have been obtained for the color-octet-scalar resonance model as compared to the standard dijet resonance search results. We did not get a better limit on qq and qg signal samples, as the expected improvement is close to unity and the final results end up being somehow worse than the no-tagging analysis.

REFERENCE

- Aaboud, M., et al. (ATLAS Collaboration), 2017. Search for new phenomena in dijet events using 37 fb^{-1} of pp collision data collected at $\sqrt{s} = 13 \text{ TeV}$ with the ATLAS detector. *Phys. Rev.*, D96 (5), 2004.
- Aad, G. et al. (ATLAS Collaboration), 2010. Search for New Particles in Two-Jet Final States in 7 TeV Proton-Proton Collisions with the ATLAS Detector at the LHC. *Phys. Rev. Lett.*, 105 (16), 161801.
- Abbiendi, G. (CMS Collaboration), 2015. The CMS muon system in Run2: preparation, status and first results. European Physical Society Conference on High Energy Physics, Vienna, Austria.
- Abbott, B. et al. (ATLAS Collaboration), 2011. A search for new physics in dijet mass and angular distributions in pp collisions at $\sqrt{s} = 7 \text{ TeV}$ measured with the ATLAS detector. *New Journal of Physics*, 13 (5), 053044.
- Acosta, D. et al. (CMS Collaboration), 2006. CMS Physics : Technical Design Report Volume 1: Detector Performance and Software. CERN.
- Acton, P.D., et al. (OPAL Collaboration), 1993. A study of differences between quark and gluon jets using vertex tagging of quark jets. *Zeitschrift für Physik C Particles and Fields*, 58 (3), 387–403.3
- Adriani, O. et al. (LHCf Collaboration), 2006. LHCf experiment: Technical Design Report. CERN.
- Airapetian, A. et al. (ATLAS Collaboration), 1999. ATLAS : Detector and physics performance technical design report. Volume 1 CERN-LHCC-99-14, ATLAS-TDR-14
- Alexander, G. et al. (OPAL Collaboration), 1996. A comparison of b and uds quark jets to gluon jets. *Zeitschrift für Physik C Particles and Fields*, 69 (1), 543–560.
- Anelli, G. et al. (LHCb Collaboration), 2003. LHCb Technical Design Report: Reoptimized Detector Design and Performance. CERN.
- Angelopoulos, V., Ellis, J., Kowalski, H., Nanopoulos, D., Tracas, N., and Zwirner, F., 1987. Search for new quarks suggested by the superstring. *Nuclear Physics B*, 292, 59 – 92.
- Anonym, 2015. The Large Hadron Collider. CERN. <https://home.cern/> (02.10.2017)
- Anonym, 2017. FQA LHC the guide. Education Communications and Outreach Group at CERN.
- Atkin, R., 2015. Review of jet reconstruction algorithms, *Journal of Physics: Conference Series*, 645, 012008.
- Bagger, J., Schmidt, C., and King, S., 1988. Axigluon production in hadronic collisions. *Phys. Rev. D*, 37 (5), 1188-1196.
- Bakırcı, M. N. et al. (CMS Collaboration), 2013. Search for narrow resonances and quantum black holes in inclusive and b-tagged dijet mass spectra from pp collisions at $\sqrt{s} = 7 \text{ TeV}$. *Journal of High Energy Physics*, arXiv:1210.2387.
- Bat, A. et al. (CMS Collaboration), 2015. Search for narrow resonances decaying to dijets in proton-proton collisions at $\sqrt{s} = 13 \text{ TeV}$. *Phys. Rev. Lett.*, 116 (7), 1801.

- Bayatian, G. L. (CMS Collaboration), 2006. CMS Physics : Technical Design Report Volume 1: Detector Performance and Software. CERN.
- Baur, U., Hinchliffe, I., and Zeppenfeld, D., 1987. Excited Quark Production at Hadron Colliders. Workshop: From Colliders to Super Colliders Madison, Wisconsin.
- Bell, P. J. et al. (ATLAS Collaborion), 2015. Search for new phenomena in the dijet mass distribution using pp collision data at $\sqrt{s} = 8$ TeV with the ATLAS detector. Journal reference: Phys. Rev. D, 91 (5), 2007.
- Bentvelsen, S. and Meyser, I., 1998. The Cambridge Jet algorithm: features and applications. The European Physical Journal C, 4 (4), 623-629.
- Beringer, J. et al. (Particle Data Group), 2013. Review of Particle Physics. Chinese Physics , 40 (10), 100001.
- Bernet, C., et al. (CMS Collaboration), 2007. Particle-Flow Event Reconstruction in CMS and Performance for Jets, Taus, and E_T^{miss} . CERN Document Server, CMS PAS PFT-09-001.
- Bhattacharjee, B., Mukhopadhyay, S., Nojiri, M., M.Sakakie, Y., and Webberf,B. R., 2016. Quark-gluon discrimination in the search for gluino pair production at the LHC. Journal of High Energy Physics, arXiv:1609.08781v2.
- Botje, M. 2013. SU(2) and SU(3) Symmetry. National Institute for Subatomic Physics (Nikhef), Utrecht.
- Cacciari, M., Salam, G. P., and Soyez, G., 2008. The anti- k_t jet clustering algorithm. Journal of High Energy Physics, 08 (4), 063.
- Catani, S., Dokshitzer, Y. L., Seymour, M. H., and Webber, B. R., 1993. Longitudinally invariant K_t clustering algorithms for hadron hadron collisions. Nucl. Phys.B, 406 (1-2), 187-224.
- Chatrchyan, S. (CMS Collaboration), 2010. Performance of the CMS Drift Tube Chambers with Cosmic Rays. JINST, 5, T03015.
- Chatrchyan, S. et al. (CMS Collaboration), 2015. Search for resonances and quantum black holes using dijet mass spectra in proton-proton collisions at $\sqrt{s} = 8$ TeV. Phys. Rev. D, 91 (05), 2009.
- Cittalin, S. et al. (CMS Collaboration), 2002. The TriDAS Project Technical Design Report, Volume 2: Data Acquisition and High-Level Trigger. CERN.
- Cornelis, T., et al. (CMS Collaboration), 2014. Quark-gluon Jet Discrimination At CMS. The Large Hadron Collider Physics Conference, Columbia University, New York.
- Cortese, P., et al. (ALICE Collaboration), 2004. ALICE: Physics performance report, volume I. J. Phys, G30, 1517-1763.
- David, B., 2016. CMS Detector Slice. CERN Document Server. <https://cds.cern.ch/record/2120661> - (06.03.2018)
- Del Re, D., et al. (CMS Collaboration), 2009. Plans for Jet Energy Corrections at CMS. CERN Document Server, CMS-PAS-JME-07-002.
- Eichten, E., Hinchliffe, I, Lane ,K. D., and Quigg, C., 1984. Super Collider Physics. Rev. Mod. Phys., 56, 579-707.
- Ellis, R. K. et al., 1996. OCD and Collider Physics. Cambridge University Press,435, Cambridge.

- Ellis, S. D., Huston, J., Hatakeyama, K., Loch, P., and Toennesmann, M., 2007. Jets in Hadron-Hadron Collisions. *Progress in Particle and Nuclear Physics*, 60 (2), 484-551.
- Elizabeth, H. S., 1997. Coloron phenomenology. *Phys. Rev.D*, 55 (3), 1678-1683.
- Gallicchio, J. and Schwartz, M. D., 2011. Pure Samples of Quark and Gluon Jets at the LHC. *Journal of High Energy Physics*, arXiv:1104.1175.
- Gallicchio, J. and Schwartz, M. D., 2013. Quark and Gluon Jet Substructure. *Journal of High Energy Physics*, arXiv:1211.7038.
- Gasparini, F. et al. (CMS collaboration), 1997. The CMS muon project : Technical Design Report. CERN.
- Green, D. et al. (CMS Collaboration), 1997. HCAL Technical Design Report. CERN, LHCC 97-31, CMS TDR 2.CERN.
- Griffiths, D., 2008. *Introduction to Elementary Particles*. WILEY-VCH, V454, Weinheim.
- Harel, A., et al. (CMS Collaboration), 2007. Calorimeter Jet Quality Criteria for the First CMS Collision Data. CERN Document Server, CMS-PAS-JME-09-008.
- Harris, R. M. et al., 2006. CMS Sensitivity to Dijet Resonances. CERN Document Server, CMS-NOTE-2006-070.
- Harris, R.M and Kousouris, K., 2011. Searches for Dijet Resonances at Hadron Colliders. *International Journal of Modern Physics A*. p5005-5055.
- Hauth, E. J. et al., 1990. Toward a Standardization of Jet Definitions. DPF Summer Study on High-energy Physics: Research Directions for the Decade Snowmass, Colorado.
- Han, T., Lewis, I., and Liu, Z., 2010. Colored Resonant Signals at the LHC: Largest Rate and Simplest Topology. *Journal of High Energy Physics*, arXiv:1010.4309.
- Herve, A. et al. (CMS Collaboration), 1997. The CMS magnet project : Technical Design Report. CERN.
- Hoffer, H. et al. (CMS Collaboration), 1997. The Electromagnetic Calorimeter Technical Design Report. CERN.
- Isildak, B. 2011, Measurement of the differential dijet production cross section in proton-proton collisions at $\sqrt{s} = 7$ (Ph.D Thesis), Institute for Graduate Studies in Science and Engineering, Bogaziçi University.
- Karimäki, V. et al. (CMS Collaboration), 1997. The CMS tracker system project : Technical Design Report. CERN
- Khachatryan, V. et al. (CMS Collaboration), 2010. Search for Dijet Resonances in 7 TeV pp Collisions at CMS. *Phys. Rev. Lett.*, 106 (02), 9902.
- Kienzle, W. et al. (TOTEM Collaboration), 1997. Total cross section: elastic scattering and diffraction dissociation at the LHC. CERN.
- Larkoski, A. J., Thaler, J., and Waalewijn, W. J., 2014. Gaining (Mutual) Information about Quark/Gluon Discrimination. *Journal of High Energy Physics*, arXiv:1408.3122v3 .
- Lobanov, A. (CMS Collaboration), 2015. The CMS Outer HCAL SiPM Upgrade. *Journal of Physics: Conference Series*, 587 (1), 012005.
- Marini, A. C., Pandolfi, F., Bansal, S., Cornelis, T., van Remortel, N., Azzurri, P., and Del Re, D., 2013. New gluon/quark jet discriminator. CERN Document Server, CMS AN AN-12-281.

- Mrenna, S. et al. (CMS Collaboration), 2016. Event generator tunes obtained from underlying event and multiparton scattering measurements. *European Physical Journal C*, arXiv:1512.00815v2.
- Ozturk, S. et al. (CMS Collaboration), 2011. Search for resonances in the dijet mass spectrum from 7 TeV pp collisions at CMS. *Physics Letters B*, 704 (3), 123-142.
- Ozturk, S., 2014. Identification of Parton Pairs in a Dijet Event and Investigation of Its Effects on Dijet Resonance Search. *Hindawi Advances in High Energy*, <http://dx.doi.org/10.1155/2014/719216>.
- Pinfold, J. et al. (MoEDAL Collaboration), 2009. Technical Design Report of the MoEDAL Experiment. CERN.
- Pua, J. (CMS Collaboration), 2015. CMS luminosity measurements for the 2016 data-taking period. CERN Document Server, CMS PAS LUM-17-001.
- Randall, L. and Sundrum, R., 1999. A Large Mass Hierarchy from a Small Extra Dimension. *Phys.Rev.Lett.*, 83(17), 3370-3373.
- Rauco, G. et al. (CMS Collaboration), 2017. Jet algorithms performance in 13 TeV data. CERN Document Sever, CMS PAS JME-16-003.
- Salam, G. P. and Soyes, G., 2007. A practical Seedless Infrared-Safe Cone jet algorithm. *Journal of High Energy Physics*, arXiv:0704.0292.
- Sakuma, T. and McCauley, T., 2014. Detector and Event Visualization with SketchUp at the CMS Experiment. *Journal of Physics: Conference Series*, 513(2), 022032.
- Schael, S. (CMS Collaboration), 2003. The CMS silicon strip detector - mechanical structure and alignment system. 11th International Workshop on Vertex Detectors, Kailua-Kona, USA.
- Soyez, G. Salam, P. G. and Cacciari, M., 2011. FastJet user manual. *The European Physical Journal C*, arXiv:1111.6097.
- Sphicas, P. et al. (CMS Collaboration), 2015. The Computing Project Technical Design Report. CERN.
- Sterman, G. et al (CTEQ Collaboration), 1995. Handbook of perturbative QCD: Version 1.0. *Rev.Mod.Phys.*, 67, 157-248.
- Topaklı, H. et al. (CMS Collaboration), 2013. Search for narrow resonances using the dijet mass spectrum in pp collisions at $\sqrt{s} = 8$ TeV. *Phys. Rev. D*, 87 (11), 4015.
- Vidal, X. C. and Manzano, R. C., 2017. LHC.Taking a closer look at LHC. https://www.lhc-closer.es/taking_a_closer_look_at_lhc/1.home/ (02.10.2017)
- Yang, C. N. and Mills, R. L., 1954. Conservation of Isotopic Spin and Isotopic Gauge Invariance. *Phys. Rev.*, 96 (1), 191.
- Zwalinski, L. et al. (ATLAS Collaboration), 2012. Search for new physics in the dijet mass distribution using 1 fb^{-1} of pp collision data at $\sqrt{s}=7$ TeV collected by the ATLAS detector. *Physics Letters B*, 708 (1-2), 37-54.

APPENDIX A

Two particle to two particle decay $1 + 2 \rightarrow 3 + 4$.

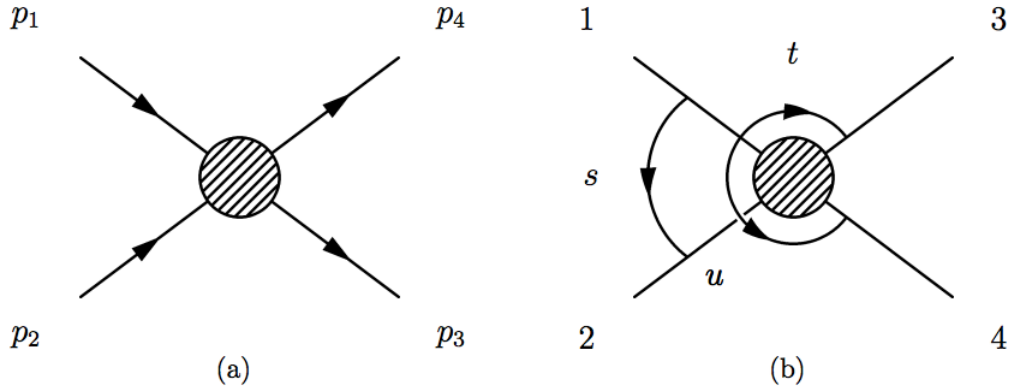


Figure A.1: Two-particle scattering. The kinematical constraints are energy-momentum conservation and the mass shell condition (a). Visualization of Mandelstam variables (b)

The Mandelstam variables are defined according to Figure A.1.

$$\begin{aligned}
 s &= (p_1 + p_2)^2 \\
 t &= (p_1 - p_3)^2 \\
 u &= (p_1 - p_4)^2
 \end{aligned}
 \tag{A.1}$$

The center of mass frame is defined by:

$$\vec{p}_1 + \vec{p}_2 = 0 = \vec{p}_3 + \vec{p}_4
 \tag{A.2}$$

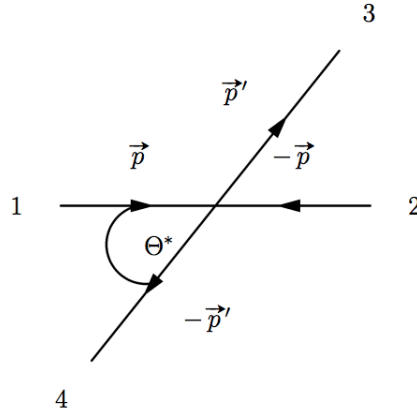


Figure A.2: Two-particle scattering in center of mass frame. For the constraints on the scattering angle $\cos\theta^*$

In the following we take a closer look at the center of mass frame, see Figure A.2
Equation A.2 leads to:

$$\vec{p}_1^* = -\vec{p}_2^* = \vec{p}$$

$$\vec{p}_3^* = -\vec{p}_4^* = \vec{p}'$$

$$p_1 = (E_1^* = \sqrt{\vec{p}^2 + m_1^2}, \vec{p})$$

(A.3)

$$p_2 = (E_2^* = \sqrt{\vec{p}^2 + m_2^2}, -\vec{p})$$

$$p_3 = (E_3^*, \vec{p}')$$

$$p_4 = (E_4^*, -\vec{p}').$$

The Mandelstam variables can be defined as follow:

$$t = -\frac{1}{2} s (1 - \cos\theta^*)$$

(A.4)

$$u = -\frac{1}{2} s (1 + \cos\theta^*)$$

The Mandelstam variable s can be expressed in terms of the outgoing partons transverse momentum p_T and y^* :

$$s = 4p_T^2 \cosh^2 y^* \quad (\text{A.5})$$

The rapidity can be defined from measured energy and momentum by:

$$y = \frac{1}{2} \ln \frac{E + p_z c}{E - p_z c} \quad (\text{A.6})$$

The rapidities of the outgoing partons, in the center-of-mass frame, are opposite ($\pm y^*$), due to transverse momentum conservation, and related to the scattering angle:

$$\cos \theta^* = \tanh y^* \quad (\text{A.7})$$

The definition of the pseudo-rapidity given by:

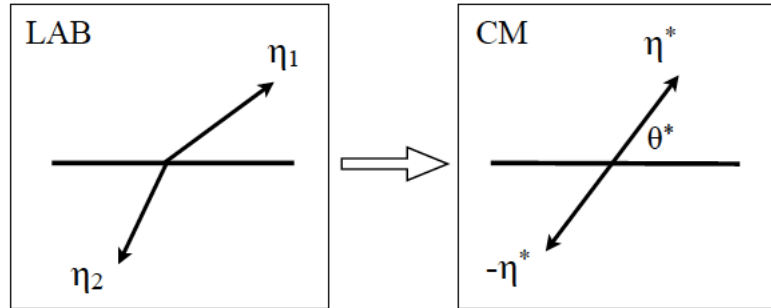


Figure A.3: Lab frame and center of mass (CM) frame of a two parton system.

$$\eta = \frac{1}{2} \ln \frac{1 + \cos \theta}{1 - \cos \theta} = \ln \frac{\cos \theta/2}{\sin \theta/2} = -\ln(\tan \theta/2) \quad (\text{A.8})$$

$$\eta_{boost} = \frac{1}{2}(\eta_1 + \eta_2)$$

$$\eta^* = \frac{1}{2}(\eta_1 - \eta_2) \tag{A.9}$$

$$\eta_{LAB} = \eta^* + \eta_{boost}$$

From the relations above, one can express the scattering angle at the center-of-mass frame as a function of the rapidities of the scattered partons at the laboratory frame:

$$\cos \theta^* = \tanh\left(\frac{\eta_1 - \eta_2}{2}\right) \tag{A.10}$$

APPENDIX B

Interpolation technique used to produce the intermediate masses for every 100 GeV in this search. The method, based on the vertical interpolation.

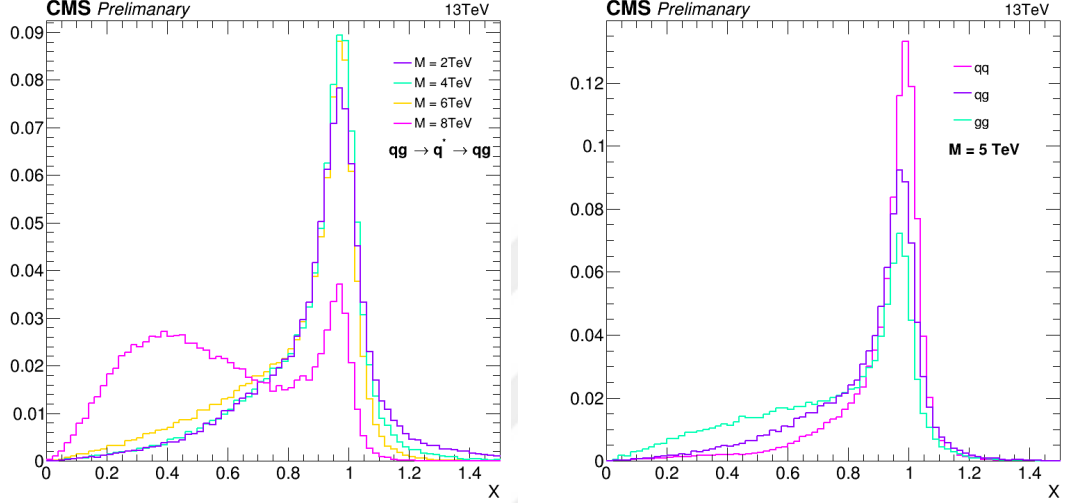


Figure B.1: Left: The distribution of X variable for qq resonance at various resonance mass points. Right: Comparison of X distribution at the resonance mass of 5 TeV for qq, qg, and gg resonance sample.

These interpolated mass generated using their neighbor resonances which produced using MC. First a new parameter X is introduced as $X = \frac{M_{jj}}{M_{Res}}$, where M_{jj} is dijet mass and M_{Res} is resonance mass. Then the new X distribution of any resonance mass is generated using their neighbor existing MC simulation samples. For instance, if we want to produce the X distribution of resonances with a mass at 6.5 TeV, we use the equation A.11

$$Prob_{6.5TeV}(x) = Prob_{6TeV}(x) + \left[Prob_{7TeV}(x) - Prob_{6TeV}(x) \right] \cdot \frac{6.5 - 6}{7 - 6.5} \quad (A.11)$$

We can generalize the formula for M that representing the resonance point which is wanted to generate for M_1 and M_2 are the neighbor resonances mass for the mass M.

Finally, We can be describe the formula in below:

$$Prob_M(x) = Prob_{M_1}(x) + \left[Prob_{M_2}(x) - Prob_{M_1}(x) \right] \cdot \frac{6M - M_1}{M_2 - M} \quad (\text{A.12})$$

After all, X distribution is converted to dijet mass bins to get resonance shape at any resonance mass point. The Figure B.1 shows the distribution of X variable for different mass point and resonance type.



CURRICULUM VITAE

Name : Ayşe
Surname : BAT
Date of birth : 07/12/1987
Place of birth : Tokat/TR
E-Mail : aaysbt@gmail.com
Languages : Turkish, English
Bachelor Degree :2004- 2010
Dumlupinar University Kutahya/Turkey
Physics Department 3.10/4.00
Master Degree :2010-2012
Dumlupinar University Kutahya/Turkey
High Energy Physics
Thesis: Simulation of Electron Gun and Superconducting Accelerating Structures at Self Amplifications of Spontaneous Emission Laser Systems
Ph.D Degree :2012-2018
Gaziosmanpasa University Tokat/Turkey
Particle Physics
Thesis: Search For New Particles Decaying to Dijet with Quark/Gluon Jet Tagging at 13 TeV Proton-Proton Collisions at CMS
Fellowship :2017
I have granted from TAEK to work on CMS HCAL Phase1 Upgrade for 6 months.
Fellowship 2015-2016
TUBITAKFellowship- Researcher Fellow in FERMILAB for a year.